ANUL XLIX **2004**

S T U D I A
UNIVERSITATIS BABEŞ-BOLYAI
PHYSICA
2

Papers presented at the 1st International Conference

Advanced Spectroscopies on Biomedical and Nanostructured Systems

2004 September 19-22, Cluj-Napoca, Romania

EDITORIAL OFFICE: Republicii no. 24, 400015 Cluj-Napoca ♦ Phone 0264-40.53.52

SUMAR - CONTENTS - INHALT

PLENARY LECTURES AND ORAL PRESENTATIONS

STUDIA UNIVERSITATIS BABEŞ-BOLYAI, PHYSICA, XLIX, 2, 2004

PLENARY LECTURES AND ORAL PRESENTATIONS

ELECTRONIC STRUCTURE AND SYMMETRY CHARACTERIZATION OF II-VI SEMICONDUCTOR QUANTUM DOTS EMBEDDED IN GLASS MATRIX

K BABOCSI[1], C. DEM[1], M IVANDA[2], V KULAKOVSKII[3], M SCHMITT[1] and W KIEFER[1*]

[1]Institut für Physikalische Chemie, Universität Würzburg, Am Hubland, D-97074 Würzburg, Federal Republic of Germany
[2]Ruder Boskovic Institute, P.O. Box 180, 10002 Zagreb, Croatia
[3]Institute of Solid State Physics, RAS, Moscow, Russia
**Corresponding author. Tel: +49-931-8886330; Fax: +49-931-8886332; Email: wolfgang.kiefer@mail.uni-wuerzburg.de*

ABSTRACT. By means of polarized low wavenumber Raman (LWR) spectroscopy the acoustic vibration modes in commercially available CdS_xSe_{1-x} nanocrystals embedded in glass matrix were investigated. The QD's size was determined using the inverse proportionality between the wavenumber of acoustic modes and the QD's diameter. Strong exciton-exciton coupling and spin dephasing effects in confined systems were observed by analyzing the polarization properties of femtosecond four wave mixing (FWM) signals. The appearance of strong FWM signals in forbidden polarization geometries is a proof of the formation of biexcitons in QDs and of the splitting of the lowest lying exciton state Δ, yielding direct information about the QD's asymmetry.

Keywords: semiconductor nanocrystals, QD's size, QD's symmetry

Introduction

Semiconductor nanocrystals with spatial dimensions on the order of the bulk exciton radius ($a_B \approx 10$ nm) or less were extensively investigated in the last decade [1-7]. However, their optical properties are still not entirely understood. Their large application range from spintronics to quantum computation [1,2] requires a more clear understanding of the physics of quantum confinement. Due to their dimensions ranging on a nanometer scale, the degrees of freedom of the electrons and holes are substantially reduced in semiconductor QDs. Such spatial confinement of carriers leads to redistribution of the energy levels into a discrete spectrum, leading not only to huge enhancement of optical nonlinearities of quantum dots (QD's), but also to novel properties, previously not observed in the bulk. Issues like inhomogeneous size distribution in the sample usually complicate the study of QD's, because the exciton energy is very sensitive to the size of the nanocrystal. Promissing results in the information transfer and storage in quantum confined spins focused the efforts of scientists on the ability to control and maintain the spin coherence over a practical length and time scale.

In this work we realize a full characterisation and determine essential parameters of CdSSe QDs embedded in glass matrix by means of linear and nonlinear spectroscopy methods. The samples are commercially available Schott filter glasses. 3D spatial confinement of electrons and holes leads not only to strong carrier-carrier interaction, but also a strong carrier-phonon coupling can be observed, whose vibration frequency is definitely correlated to the nanocrystal's size [8]. Polarized low wavenumber Raman spectroscopy was succesfully applied in order to put in evidence the presence of acoustic phonons in the QDs under discussion, thus constituting a direct measure of the nanocrystals diameter and size distribution inside the sample.

It was shown [9,10] that in confined systems the role of Coulomb interactions cannot be neglected between excitons, leading to the formation of exciton molecules – so called biexcitons. By studying the polarization properties of the femtosecond four wave mixing (FWM) signal we prove the existence of biexcitons. Moreover, an exciton spin dephasing effect is evidenced, which is correlated to the energy splitting of the lowest lying exciton state. The energy structure is correlated to the QD's asymmetry; therefore we can show that femtosecond FWM measurements are an efficient tool to determine the symmetry of the QD's shape.

Low Wavenumber Raman Scattering on CdSSe QD's

In this section we focus on polarized low wavenumber Raman (LWR) spectra for CdS_xSe_{1-x} QDs of different sizes embedded in glass matrix. We used 90° scattering geometry and recorded the spectra in the low wavenumber regime, very close to the Rayleigh line (≈ 4 cm^{-1}). The excitation occurred in off-resonance conditions using the krypton ion laser line at 647 nm at a power of 42 kW. LWR spectra were recorded by means of a Spex 1403 double monochromator equipped with a multichannel detection system (CCD camera Photometrics RDS 900). We included in our setup linear polarizers and recorded the LWR spectra in two polarization geometries: VV (excitation beam vertically polarized and scattered light vertically analyzed) and HV (excitation light horizontally polarized, whereas scattered light vertically analyzed).

In a first approximation, the QDs are free, homogeneous, perfectly symmetric spheres. The vibration spectrum of such a sphere contains two types of acoustical modes as shown in Fig. 1: spheroidal and torsional [11].

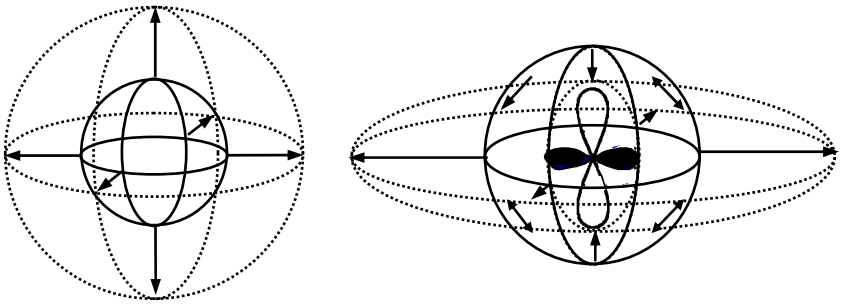

a. b.

Fig. 1. a. Breathing mode: angular momentum *l*=0, active only in VV polarization geometry. **b.** Quadrupolar Mode: angular momentum *l*=2, depolarized and active in both VV and HV polarizations.

These vibration modes are labelled according to the symmetry group of the sphere with *l* and *m*, in analogy to the harmonic functions Y_{lm}. An additional index p=1,2,…,n has to be considered, which indicates the sequence of eigenmodes for a fixed angular shape (*l,m*) in increasing order of radial wave vector. In Fig. 1 we depicted only the spheroidal modes, labelled *l*=0 (Fig. 1a – radial symmetry) and *l*=2 (Fig. 1b – quadrupolar), because only these two modes are Raman active [12]. The depolarization ratio of the Raman signal I_{HV}/I_{VV} allows one to decide which vibration is Raman active. Figure 2 summarises the Raman spectra recorded in HV and VV polarization geometries for CdS_xSe_{1-x} of different sizes and composition, contained in Schott filter glasses, namely GG495, OG550 and OG590. The numbers next to the letters indicate the cut-off wavelength of the glass, which depends both on crystal size and composition. The fraction x for the S fraction was determined earlier by resonant Raman measurements [13]. Our interest is focused on the determination of the nanoparticles' size using the theory of Montagna and Dusi [11]. According to their observations, the wavenumber of the Raman active acoustical vibrations varies inversely proportional with the size of the nanocrystals, dependence described by the mathematical relation:

$$\tilde{\nu} = \frac{S_l v}{cd} \quad . \tag{1.1}$$

Here, $\tilde{\nu}$ stays for the wavenumber of the acoustic vibration mode, v is an average value (taking into account the crystal axes orientation) between the longitudinal (*l*=0) and transversal (*l*=2) sound velocity, c is the light velocity, and d is the diameter of the nanoparticle in cm. S_l is a proportionality coefficient depending on the angular momentum *l*, the harmonic number *n,* and the ratio between the longitudinal and transversal sound velocities v_L/v_T. In our calculations the numerical values S_0=0.84 and S_2=0.91 were used [11] and the thus determined QD's sizes are indicated in Fig. 2. In VV parallel polarization geometry the symmetric surface modes (p=1) are well pronounced and even higher harmonics (p=2,3) can be observed. For smaller particles even the quadrupolar *l*=2 are visible. In the HV geometry only the depolarized *l*=2 can be observed.

Figure 2 presents the mean diameter calculated inside the 15% [13] inhomogeneous distribution of the QD's size inside the sample. All samples are situated in the strong confinement regime, with radii much smaller in comparison to the exciton Bohr radius in the bulk ($a_B \approx 10$ nm). There is no evidence of acoustic phonon modes in bulk semiconductors. Therefore we can conclude that the relative high intensity of the acoustic vibration modes in nanoparticles is a result of quantum confinement.

Femtosecond Four Wave Mixing Spectroscopy on $CdS_{0.7}Se_{0.3}$ QD's

One of the samples, namely OG550, containing nanocrystals of 4.7 nm in radius (strong confinement regime), was chosen for further characterization by time integrated four wave mixing (TI-FWM) spectroscopy. The x fraction of S atoms was determined by resonant Raman measurements [13]. We performed degenerate FWM (DFWM) in the framework of photon echo [14] on the sample kept at 10 K

inside an optical cryostat. For optical excitation we used three 80-fs laser pulses of the same energy (2.4 eV) lying in the inhomogeneously broadened $1S_e$-$1S_h$ transition (inset in Fig. 3). The first two (in time) pulses (k_1 and k_2) are both spatially and in time overlapped and their interference in the sample volume results in a grating. The third k_3 scans this grating and is scattered on it according to the Bragg condition. The resulting FWM signal is spatially separated from the incident beams and is scattered in the direction k_s given by the phase matching condition $k_s=k_1+k_2-k_3$. The 3–pulse photon echo has as advantage the ability to individually control the polarization of each fs-pulse, thus various polarization geometries making accessible to the experiment. Left σ^+ and right σ^- hand circularly polarized laser pulses were used, the recorded TI-FWM signals being labelled corresponding to the polarization geometry I^{ijkl}, where *i,j,k,l* represent the indices of the "+" or "–" of the laser beam σ^+ and σ^- polarizations, respectively.

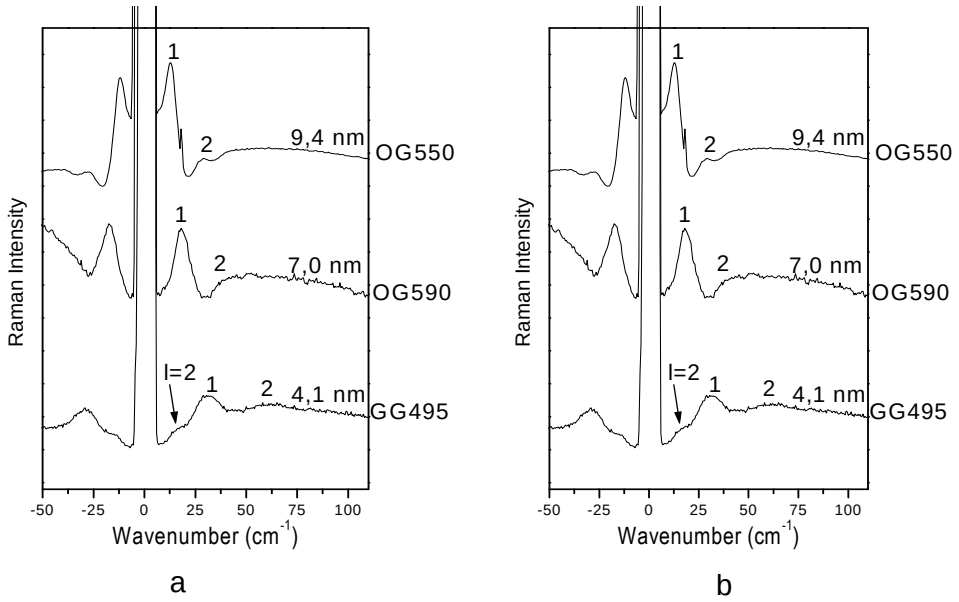

Fig. 2. a. Low wavenumber Raman spectra recorded in parallel VV geometry. **b.** Low wavenumber Raman spectra recorded in orthogonal HV polarization geometry. The calculated QD's sizes are indicated next to the glass filter's names.

Our experimental results are in contradiction with the non interacting oscillators (NIO) theory, which predicts a non-zero FWM signal only in the case when all three laser pulses have the same polarization, i.e. σ^+ and the FWM signal is recorded in I^{++++} geometry. The appearance of a strong FWM signal in forbidden polarization geometries is due to the relaxation of selection rules as result of modifications of the QD's electronic structure with respect to the bulk.

Electrons and holes in QD's are constrained in extremely reduced space and the Coulomb interactions between them cannot be ignored any longer. This results in a strong coupling between excitons belonging to the same nanocrystal. Due to the small amount of QDs in the dielectric matrix (the QDs volume fraction is only 1% in the dielectric matrix), there is no Coulomb interaction between carriers situated in different nanocrystals. Thus the appearance of FWM signals in forbidden geometries (Fig. 3) according to the non interacting systems (NIO) model is due to the strong Coulomb interactions between confined carriers.

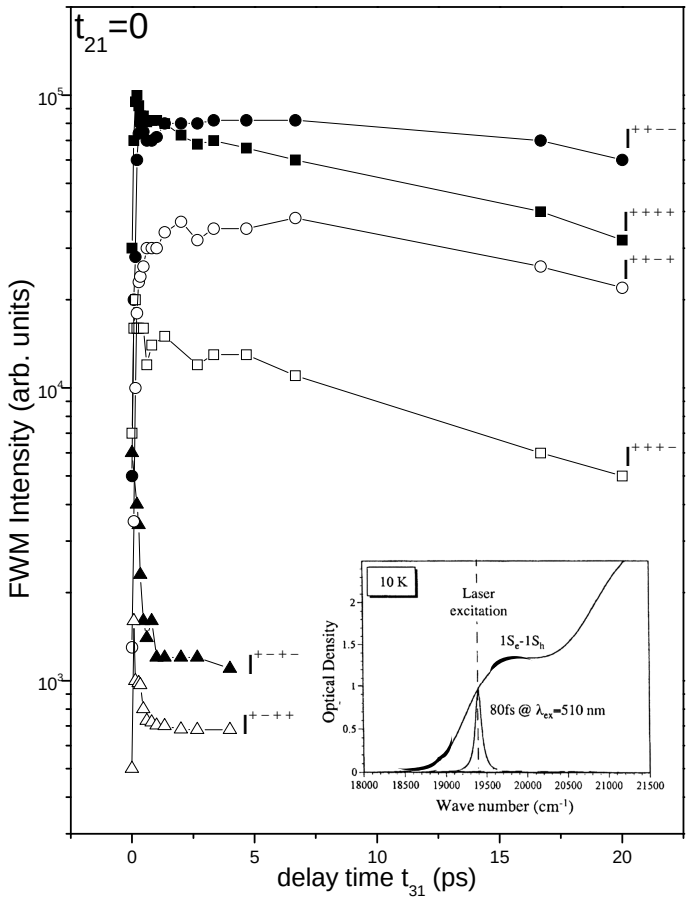

Fig. 3. TI–FWM signal recorded in different polarization geometries recorded for 4.7 nm average radii QD's at 10 K. The inset shows an absorption spectrum recorded at 10 K and the excitation energy of the fs pulses lying in the inhomogeneously broadened $1S_e$–$1S_h$ exciton transition.

In order to understand the qualitatively different time behaviour of FWM signals recorded in forbidden polarization geometries (Fig. 3) we have to analyze closer the modification of selection rules induced in the sample due to quantum

confinement. The electronic structure of confined systems [1-5] is well described in the framework of the four–level model: a ground state, an exciton spin doublet J=1, and a singlet biexciton state. The lowest lying optically active exciton state J=$\pm$1 is split further if the QD's symmetry is C_{2v} or lower, in two other states $|X\rangle=(|+1\rangle+|-1\rangle)/\sqrt{2}$ and $|Y\rangle=(|+1\rangle-|-1\rangle)/\sqrt{2}$, optically active in mutually orthogonal linear polarizations and split by the energy Δ [6,7]. Circularly polarized laser beams excite a linear combination of these and induce a spin precession with a rate given by $\Delta/2\pi\hbar$. It is important to mention that this is not a "real spin" precession, but a process due to the QD's asymmetry.

First, we focus our attention on the time behaviour of I^{++++} and I^{++--}, which both show large intensities over a relatively long period of time. The excitation process occurs as described above: the pulses k_1 and k_2 both σ^+ polarized create a population grating in the sample volume, which is scanned by pulse k_3. In the first five ps, I^{++++} and I^{++--} exhibit different behaviours: I^{++++} decays very abrupt, whereas I^{++--} first increases in intensity, and only after $\approx$ 5 ps decays with the same time constant as I^{++++} of $\approx$180 ps. Taking into account that the scattering of k_3 occurs by changing the polarization of the pulse, it is natural to suppose that the population after 5 ps is already spin dephased and the relaxation process is determined only by the decay of the population grating (exciton lifetime T$\approx$ 180 ps). Moreover, the appearance of I^{++--}, forbidden according to the NIO model can only be explained if the existence of biexcitons is accepted. In the framework of the four–level model, the selection rules allow excitation of an exciton population only if k_1 and k_2 both have the same polarization, i.e. σ^+. Scattering of σ^+ polarized k_3 leads to relaxation back to the ground state by emitting a FWM signal in the direction defined by k_s, which is also σ^+ polarized. Indeed we record the highest intensity of the FWM signal in I^{++++} geometry. In contrast, the scattering of a σ^- polarized k_3 pulse on the population grating created by two σ^+ polarized beams can only occur if the biexciton states are involved. Quantum confinement predicts the mixing of biexciton energy levels with the exciton states [5], and therefore the energy conservation rules are respected. Thus, taking strong exciton-exciton interactions and formation of biexciton states into account, the four–level model explains well the appearance of I^{++--}.

Another strong TI-FWM signal at early delay times was recorded in the I^{+-+-} configuration. Its intensity at zero delay time between the incident laser pulses is equal to that of I^{++--}, after which it drops down very quickly and disappears completely together with the temporal overlap of the pulses k_1 (k_2) and k_3. The large intensity of the signal at zero time is natural, because if all three pulses are overlapped in time, the FWM signal is symmetric under the interchange of k_1 (k_2) and k_3. Therefore, the reason for the fast decay of I^{+-+-} ($\approx$200 fs) in comparison to I^{++--}, also forbidden according to the NIO model, has to be in the qualitative difference between the gratings created by same and oppositely polarized k_1 and k_2, respectively. Two oppositely circularly polarized laser pulses create not a population, but induce a precession of the polarization vector

associated to the two linearly polarized exciton states |X> and |Y>. The polarization vector rotation period is given by $1/|k_1 – k_2|$, which is much shorter than the lifetime of excitons. The appearance of relatively strong TI-FWM signals in other forbidden polarization geometries (Fig. 3) are due to depolarization effects and lowering o the QD's symmetry. This is also proved by the ratio 1:2 valid for all intensities $I^{++++} : I^{+++-}$, $I^{++--} : I^{++-+}$ and $I^{+-+-} : I^{+-++}$.

The numerical summation of the TI-FWM signals I^{++++} and I^{++--} displays a monoexponential decay in the hole range of delay times longer than 3 ps and is a direct measure of the exciton lifetime (≈160 ps), which we determined separately by femtosecond differential transmission measurements. Moreover, the difference between I^{++++} and I^{++--} is a measure of the spin dephasing time, responsible for the increase in intensity of I^{++--} at small delay times, also separately determined by temporally overlapping k_2 and k_3, scanning with k_1 and recording the signal in the direction $k_s=k_1-k_2+k_3$. We determined a spin dephasing time of $\tau \approx 1$ ps, indicating that in our sample the energy split $\Delta \approx h/2\pi\tau$ fluctuates in the range of ± 1 meV. Therefore we can conclude that the symmetry of our system is equivalent to the group symmetry C_{2v} or lower.

Conclusions

In conclusion, we proved the efficiency of both LWR and TI-FWM spectroscopy by achieving a full characterization of commercially available CdSSe QD's embedded in a dielectric matrix. Essential modifications in the QD's electronic structure due to quantum confinement are responsible for a series of new properties with respect to the bulk. Spatial confinement of carriers leads to enhancement of acoustic phonon vibrations well evidenced in LWR spectra. The most important parameter – the QD's size was determined as a function of the acoustic phonons vibration wavenumber.

Polarization properties of the TI-FWM signal in the framework of three pulse photon echo yield information about the symmetry of the QD's embedded in the glass. We showed that the relaxation of polarization selection rules is mainly due to enhancement of Coulomb interactions between excitons belonging to the same nanoparticle. The scattering of σ^- polarized pulse on the population grating created by two σ^+ polarized beams is only possible if the existence of biexciton states is admitted. The appearance of FWM signals in polarization geometries forbidden according to the NIO model is due to the lowering of the QD's symmetry. We determined the QD's symmetry group taking the spin dephasing effect and the energy split Δ into account as being C_{2v} or lower. Thus, these two complementary methods LWR and TI-FWM allow a full characterization of the electronic structure of quantum confined systems.

Acknowledgements

This work was supported by the German Science Foundation (DFG, Sonderforschungsbereich 410, Teilprojekt C3). M. I. acknowledges also support by the Ministry of Science and Technology, Republic of Croatia (Projects TP01/0098-23 and 00980303), and V.D.K. by the Russian Foundation for Basic Research.

REFERENCES

[1] Al. L. Efros, Phys. Rev. B **46**, 7448 (1992).
[2] Al. L. Efros and A. V. Rodina, Phys. Rev. B **47**, 10 005 (1993).
[3] M. Chamarro, C. Gourdon, P. Lavallard, O. Lublinskaya, and A. I. Ekimov, Phys. Rev. B **53**, 1336 (1996).
[4] M. Nirmal, D. J. Norris, M. Kuno, M. G. Bawendi, Al. L. Efros, and M. Rosen, Phys. Rev. Lett. **75**, 3728 (1995).
[5] U. Woggon, F. Gindele, O. Wind, and C. Klingshirn, Phys. Rev. B **54**, 1506 (1996).
[6] D. Gammon *et al.*, Phys. Rev. Lett. **76**, 3005 (1996).
[7] V. D. Kulakovskii, G. Bacher, R. Weigand, T. Kummell, A. Forchel, E. Borovitskaya, K. Leonardi, and D. Hommel, Phys. Rev. Lett. **82**, 1780 (1999).
[8] S. Schmitt-Rink, D. A. Miller, and D. S. Chemla, Phys. Rev. B **35**, 8113 (1987).
[9] V. Klimov, S. Hunsche, and H. Kurz, Phys. Rev. B **50**, 8110, (1994).
[10] J. M. Caruge, Y. Chan, V. Sundar, H. J. Eisler, and M. G. Bawendi, Phys. Rev. B **70**, 085316, (2004).
[11] Montagna M and Dusi R, Phys Rev B **52**, 10080, (1995).
[12] E. Duval, Phys Rev B **46**, 5795 (1992).
[13] M. Ivanda, K. Babocsi, C. Dem, M. Schmitt, M. Montagna, and W. Kiefer, Phys. Rev. B **67**, 235329 (2003).
[14] S. Mukamel, Principles of Nonlinear Optical Spectroscopy, Oxford University Press, (1995).

STUDIA UNIVERSITATIS BABEŞ-BOLYAI, PHYSICA, XLIX, 2, 2004

FREEZING ON HEATING OF LIQUID SOLUTIONS: THE OBSERVATION OF A "LAW-BREAKING" LIQUID

M. PLAZANET,[1] C. FLOARE,[2,#] M.R. JOHNSON,[1] R. SCHWEINS[1] and H.P. TROMMSDORFF[2*]

[1]Institut Laue-Langevin, B.P. 156X, 38042 Grenoble Cx, France
[2]Laboratoire de Spectrométrie Physique, Université J. Fourier Grenoble – CNRS (UMR 5588), BP 87, 38402 St. Martin d'Hères Cx, France
permanent address: National Institute for Research and Development of Isotopic and Molecular Technologies, P.O. Box 700, 400293, Cluj-Napoca 5, Romania
hans-peter.trommsdorff@ujf-grenoble.fr, fax: 33(0)476635495

This is the story of a serendipitous discovery, which was made when preparing inclusion compounds of 4-methylpyridine (4MP: C_6NH_7) in α-cyclodextrine (αCD, the association of 6 glucose units: $(C_6O_5H_{10})_6$). At room temperature, solutions containing up to 300 g/l of 4MP in αCD are homogeneous and transparent. When heated to between 50° and 80°C, these solutions, which also c ontain the crystallization water of αCD, solidify. After cooling the solution to room temperature, the solid melts and the original solution is recovered. The figure below illustrates the phenomenon for a solution of 200g/l of 4MP in αCD.

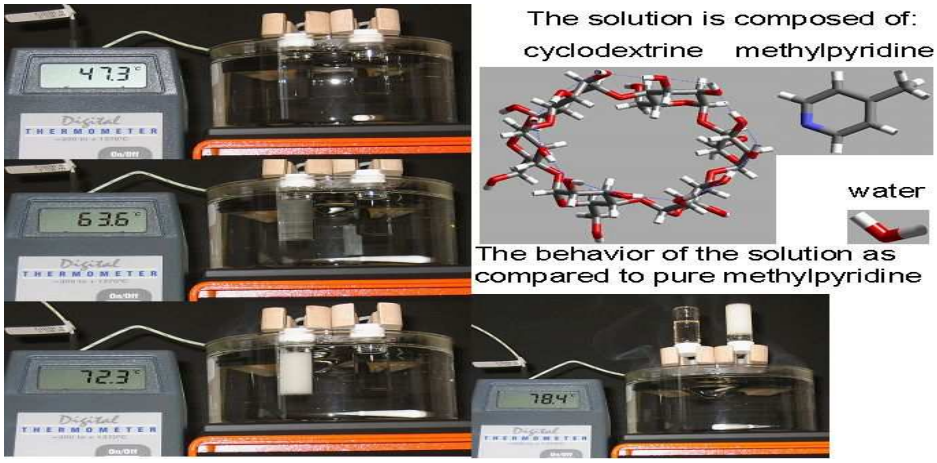

A first note on this observation has been published,[1] and this report has stirred considerable interest.[2] Here we report measurements made in order to characterize changes of the structure and of the molecular dynamics during this transition, measurements performed by elastic and quasi elastic neutron scattering (QENS) at the Institute Laue-Langevin (ILL) in Grenoble.[3] QENS measures the scattered intensity as a function of momentum transfer, $\boldsymbol{Q} = \mathbf{k}_i - \mathbf{k}_f$, and of energy

transfer, $\Delta E = E_i - E_f$. Here, $\mathbf{k}_i$ and $\mathbf{k}_f$ are the wavevectors and E_i and E_f the energies of the incident and scattered neutron, respectively, and the momentum transfer lies typically in the range of Å^{-1}. The spectrum of scattered neutrons, $S(\boldsymbol{Q},\omega = \Delta E/\hbar)$, is the Fourier transform of the intermediate scattering function, $(\boldsymbol{Q},t)$:

$$S(\boldsymbol{Q},\omega) = \frac{1}{2\pi}\int_{-\infty}^{\infty} I(\boldsymbol{Q},t)\exp(i\omega t)dt$$

where $I(\boldsymbol{Q},\tau)$ is given by:

$$I(\mathbf{Q},\tau) = \left\langle \exp(i\mathbf{Q}\mathbf{r}(t+\tau))\cdot\exp(-i\mathbf{Q}.\mathbf{r}(t))\right\rangle$$

$I(\boldsymbol{Q},t)$ is a correlation function, which involves the particle position, **r**(t), and characterizes the decay in time of the single particle fluctuations. The broadening of the energy distribution of the scattered neutrons is thus proportional to the decay of the particle-particle correlation function. This way molecular dynamics is monitored. Different instruments explore different time scales ranging from ps (IN5) to ns (IN10) and longer. The angular distribution of the scattered intensity is determined by the amplitude of the motion of the particles. Measurements with the instruments IN10 and IN16 (energy resolution ~ 1μeV), show that at room temperature, when the sample is liquid, all components diffuse on time scales faster than the upper limit of about 10^{-9} s set by the energy resolution window of these instruments. As the sample is heated, one of the components in the system slows down, making the sample solid. This slowing down upon heating results in a net increase of intensity of scattered neutrons in an energy window of 1μeV around $\Delta E = 0$, as shown in the figure below, which presents curves recorded when heating and cooling the sample at a rate of 6°/hour.

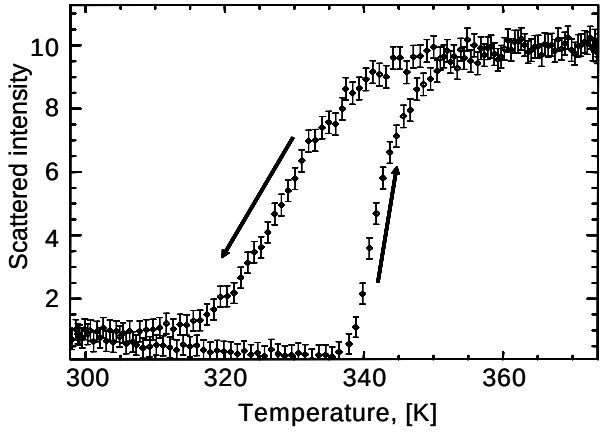

From the intensities, it is however clear that only part of the molecules are immobilized. Even at high temperature, in the solid phase, a mobility is still observed on the time scale of 10^{-11} s set by the resolution window of 100 μeV of the spectrometer IN5. Only αCD is immobilized on these time scales, but the 4MP solvent remains liquid.

These observations raise the question about structure of the solid phase: Is the solid ordered or disordered? Which length scales are involved? Exist sizable clusters of αCD already at room temperature?

In order to address these issues, measurements by neutron diffraction were performed. Small angle scattering on the instrument D11 was used to determine the presence and the size of αCD clusters.

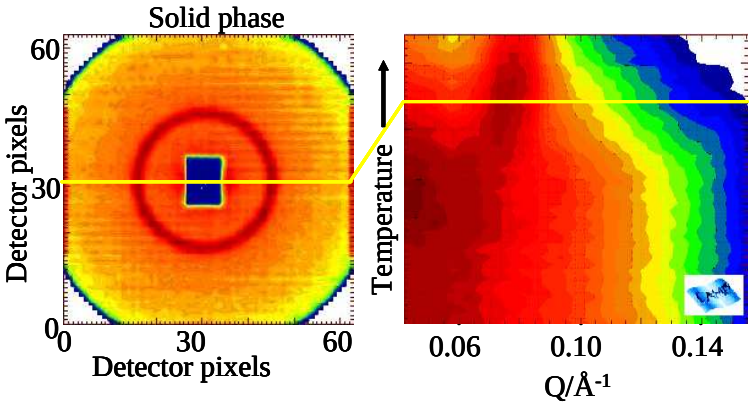

The figure above shows the results of these measurements, the left hand side is an image recorded by the 2D detector for the solid phase, while the right hand side shows a 2D plot of the evolution of the scattered intensity as a function of temperature and of angle, converted here to momentum transfer, ***Q***. At lower temperatures, this intensity distribution is typical for a liquid, while the emergence of a sharp diffraction ring signals the appearance of an ordered structure with a spacing of 44.8 Å in the solid phase. This spacing does not depend on the concentration of αCD in the original solution, indicating that the structure is not restricted to ordered layers, but could be in fact 3D crystalline. This suggestion was indeed confirmed by diffraction measurements on the instrument D16, where a powder diffraction pattern was observed for the solid phase, the first 5 prominent diffraction peaks corresponding to lattice spacings of 44.8, 20.4, 15.0, and 11.9 Å. While the space group could not be assigned unambiguously, based on these data, all possible structures have unit cells of about 15000 $Å^3$, and correspond to a probable composition: 4×[αCD + 6×H2O + ca. 60×4MP]. At still higher temperatures, above ca. 100° C, all sharp diffraction peaks disappear and the normal melting of the solid phase is observed.

How can these surprising observations be rationalized?

As temperature increases, the total entropy must increase. How can this requirement be reconciled with the observations made here that crystalline order is established and that molecular motions are slowed down?

We postulate that a rearrangement of hydrogen bonds provides the mechanism by which the solution solidifies. MD calculations indicate indeed that a structure of αCD with all ***intra***-molecular hydrogen-bonds “closed” is most stable. The opening of H-bonds with increasing temperature provides the possibility to establish ***inter-***molecular H-bonds via the water molecules and the establishment of long-range

order. How the ordering of the αCD molecules affects the entropy of the liquid phase remains a matter of exploration. What our measurements do seem to indicate is that the diffusion of the 4MP solvent is increased in the ordered structure.

The observations reported here open many avenues for future work. An obvious first objective is the determination of the crystal structure of the solid. Based on this structure, accurate MD calculations over long times should be made in order to understand this solidification phenomenon and the critical role of the small amounts of water and the H-bonds that they form with αCD and 4MP. In this way, this relatively simple molecular system will be a very useful benchmark system to test the validity of force fields and of molecular mechanics/ dynamics calculations, calculations that can not be tested in such detail for more complex biological systems. Precise calorimetric measurements must also be made to follow enthalpy changes of the phase transition.

In view of possible exploitations of this solidification phenomenon in various conceivable applications, other systems should be explored. The observation of this phenomenon in a number of cyclodextrine/pyridine systems suggests that more solutions could be found with analogous behavior. In a search for such systems, the solubility, the ability to establish intra and intermolecular hydrogen bonds, and the competition between these will be crucial factors.

REFERENCES

[1] M. Plazanet, C. Floare, M.R. Johnson, R. Schweins, H.P. Trommsdorff, J. Chem. Phys. 121(2004)5031.

[2] http://physicsweb.org/articles/news/8/9/15/1

[3] http://ill.fr/YellowBook.

[1] M. Plazanet, C. Floare, M.R. Johnson, R. Schweins, H.P. Trommsdorff, J. Chem. Phys. 121(2004)5031.
[2] http://physicsweb.org/articles/news/8/9/15/1
[3] http://ill.fr/YellowBook.

STUDIA UNIVERSITATIS BABEŞ-BOLYAI, PHYSICA, XLIX, 2, 2004

ELECTRONIC PROPERTIES OF A PEANUT-SHAPED C_{60} POLYMER

JUN ONOE[1,2]*

1) Materials Science Division, Research Laboratory for Nuclear Reactors, Tokyo Institute of Technology, 2-12-1 Ookayama, Meguro, Tokyo 152-8550, Japan.
2) Japan Science and Technology Agency (JST), 4-1-8 Honmachi, Kawaguchi, Saitama 332-0012, Japan
*Corresponding Author: Prof. Jun Onoe, Materials Science Division, Research Laboratory for Nuclear Reactors, Tokyo Institute of Technology, 2-12-1 O-okayama, Meguro, Tokyo 152-8550, Japan. TEL & FAX +81-3-5734-3073. E-mail: jonoe@nr.titech.ac.jp

ABSTRACT. Electronic properties of an electron-beam (EB)-induced C_{60} polymer, which is a new polyhedral structured (peanut-shaped) carbon nanomaterial, are presented. The current-voltage characteristics indicated that the peanut-shaped polymer exhibit metallic characters in air at room temperature. Valence photoelectron spectra of the polymer showed that the electronic structure of the C_{60} film became closer to that of graphite as the EB-irradiation time increased, and its density of states around the Fermi level was eventually greater than for the graphite. This suggests that the electronic structure of the C_{60} film changed from a semiconductor to a semi-metal and/or metal by EB irradiation. Interestingly, the electronic structure remained metallic even after 5-days of air exposure, which is the reason for the metallic electron-transport property described above. In order to elucidate the origin of the metallic properties, we have performed density-functional calculations of a peanut-shaped C_{120} dimer regarded as a basic unit of the polymer. It was found that the HOMO consisting of π–electrons orbital, which is related to the electron transport property, has no nodes in the cross-linkage region between C_{60} molecules and spreads over the peanut-shaped dimer, indicating that electrons move freely from one to another side.

I. INTRODUCTION

Since the first report on C_{60} photopolymerization [1], there have been several reports of methods to produce C_{60} polymers [2]. In particular, C_{60} polymerization induced by light and electron-beam (EB) radiation is of very interest from a viewpoint of nanofabrication of C_{60}-based carbon materials.

For the C_{60} photopolymer, it was found that the photopolymerization of C_{60} molecules forms a 2D hexagonal C_{60} polymer with an intermolecular bond of the [2+2] cycloadditional four-membered ring, as illustrated in Fig. 1 [3-8], and four-probe measurements indicated that the 2D C_{60} polymer is an intrinsic semiconductor [9]. However, because the C_{60} photopolymer is readily decomposed into C_{60} monomers even at a substrate temperature higher than 373 K [3], this material can be hardly applied to nanofabrication processes. More coalesced intermolecular bonds between C_{60} molecules are necessary practically.

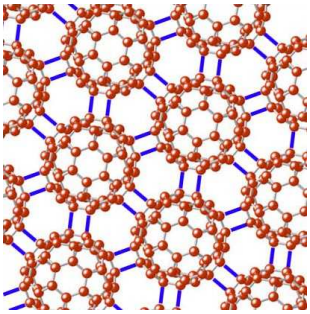

Figure1. Schematic illustration of a two-dimensionally hexagonal C_{60} polymer with an intermolecular bond of the [2+2] four-membered ring.

In our recent work [10-12], comparison of infrared spectra with theoretical IR calculations indicated that an electron-beam (EB) irradiated C_{60} film is neither graphite nor carbon nanotube-like but a peanut-shaped C_{60} polymer (a typical peanut-shaped C_{60} dimer structure is shown in Fig. 2.

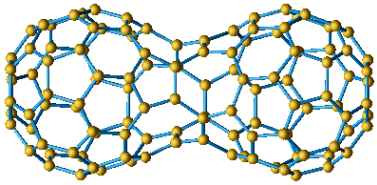

Figure 2. Schematic illustration of a peanut-shaped C_{120} structure formed in a C_{60} film under electron-beam irradiation.

Although many attempts to examine electron-stimulated polymerization of solid C_{60} have been made [13-20], there have been no previous reports on the formation of such a peanut-shaped polymer. This polymer can be regarded as a π-electron-conjugated system and expected to exhibit a metallic property.

In the present paper, electronic properties of the peanut-shaped C_{60} polymer are presented. We first showed the current—voltage (I—V) characteristics and sheet resistance of the EB-induced peanut-shaped polymer by four-probe measurements [21], and compared these with the electrical property of pristine solid C_{60} [22, 23]. To use four-probe enables us to extract the sheet resistance of films despite of unknown resistances at the electrical contacts between the probes and the film. We next showed *in situ* photoelectron spectra of the C_{60} film before and after EB irradiation in order to understand the electron transport properties [24]. Thereafter, the origin of the electron transport properties were discussed on the basis of density-functional calculations of a peanut-shaped C_{120} dimer regarded as a basic unit of the peanut-shaped polymer [25].

II. EXPERIMENTS

C_{60} films (70 nm thick) were formed on a CsI substrate in an ultrahigh vacuum (UHV) chamber (base pressure: 1×10^{-7} Pa) by sublimation of C_{60} powder. Thereafter, the C_{60} film was irradiated *in situ* with an EB with an incident energy of 3 keV was applied to the film using an EB-gun connected to the UHV chamber. After the EB

irradiation, the sample was subsequently taken out of the UHV chamber and its sheet resistance and I—V characteristics were measured at room temperature (RT) under normal atmospheric conditions. The experimental details were described elsewhere [21].

The present *in situ* photoelectron spectroscopy apparatus consisted of three UHV chambers. The UHV chamber (base pressure: 3×10^{-7} Pa), equipped with a Knudsen cell (K-cell), a molecular turbo pump (Balzers), an electron-beam gun (Omegatron), and a partial pressure gage (ANELVA QIG-066), was connected to an UHV load-lock preparation chamber (base pressure: 2×10^{-7} Pa) via a gate valve. After a C_{60} film (100 nm thick) formed on a stainless steel substrate, the pristine C_{60} film was transferred to a UHV analysis chamber (base pressure: 1×10^{-7} Pa) by way of the preparation chamber and measured *in situ* by x-ray photoelectron spectroscopy (XPS) and ultraviolet photoelectron spectroscopy (UPS). The film thickness was sufficient to ignore the influence of the substrate on the valence electronic structure of solid C_{60} [26]. In addition, we already confirmed from *in situ* quadrupole mass spectra that no C_{60} molecules were desorbed from the film under the same EB irradiation conditions [10]. After the measurements, the film was returned to the 1st chamber and irradiated with the EB-gun for 50 h at 10-h increments. After every 10-h irradiation, the film was transferred to the analysis chamber for XPS and UPS measurements with a step of 50 meV. After the measurements of the 50-h irradiated film, the sample was air-exposed under atmospheric conditions for 5 days. Subsequently, the air-exposed film was returned to the analysis chamber and measured by XPS and UPS spectroscopy.

III. COMPUTATIONAL

The present density-functional (DFT) calculations were carried out using the Amsterdam density-functional program (ADF) [27]. In ADF, the basis functions of Kohn-Sham molecular orbitals are expressed by Slater-type orbitals (STOs), and the most integrals in calculating, e.g., Fock matrix elements, the bonding energy, gradients in geometrical optimization, etc. are evaluated numerically. Double-zeta STOs augmented with single-zeta 3d polarization functions were used for valence orbitals of the carbon atom, while C 1s core shell was treated by the frozen-core approximation. The local density approximation (LDA) with the Vosko-Wilk-Nusair (VWN) exchange-correlation was employed. The details of the present DFT calculations were described elsewhere [9, 28].

IV. RESULTS AND DISCUSSION

A. Electron transport properties

Figure 3 shows the I—V characteristics and sheet resistance of the C_{60} polymer formed after 20-h EB irradiation. The open circles represent I—V characteristics measured by probes 1 and 4 (outer probes), while the open rectangles represent the sheet resistance derived from voltages measured by probes 2 and 3 (inner probes).

Inset in this figure show the optical micrograph taken during the corresponding four-probe measurement. Interpole distances were set in the range 8 – 40 μm, ensuring appropriate film thickness for four-probe measurement [29], and in the particular case of Fig. 3, the distance was 35 μm. As shown in Fig. 3, the sheet resistance fluctuated around 0 V. This was due to the diminished measurement accuracy for small currents

and/or small voltages in the present system. The sheet resistance and I—V characteristics of pristine C_{60} film could not be obtained, because sheet resistance was beyond the measurement range of the present system.

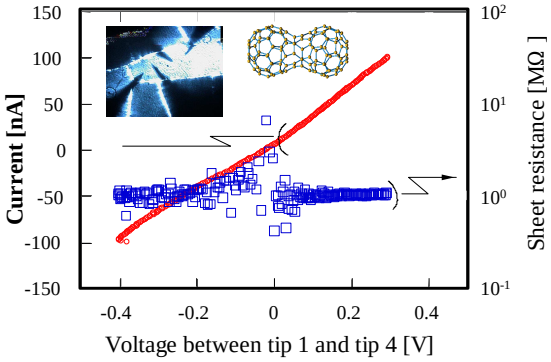

Figure 3. The sheet resistance and current—voltage curve of the 20-h EB irradiated C_{60} film obtained using four-probe measurements. The squares represent the data of the sheet resistance for each film, while the circles display the I—V curve for each film. Insets in each figure show the optical micrographs during the corresponding four-probe measurement. A typical distance between adjacent probes was set in the range 8—40 μm.

As shown in Fig. 3, there is no prolonged plateau around V = 0, and that the I—V curve is linear. In other words, no Schottcky barrier was formed between the film and the metal probes. This indicates the metallic property of the peanut-shaped C_{60} polymer. The resistance directly derived from the I—V curve included large contact resistances due to the small contact area between the sharp tungsten probes and the film, and it is actually difficult to measure the contact resistances. Accordingly, the sheet resistances of the film were measured using voltage difference between inner two probes [30]. Here, it is noted that the contacts of the inner probes to the film were ohmic. Sheet resistance of 1 MΩ in Fig. 3 corresponds to a resistivity of 7 Ωcm (in this case film thickness was 70 nm), We performed four-probe measurements at several locations on the same film and on the different film of 160 nm thick, and the resistivity was distributed in the range 1 – 10 Ωcm. Therefore, it was concluded that the resistivity of the EB-induced C_{60} polymer is considerably smaller than pristine C_{60} by a factor of 10^8 to 10^{14} [22, 23]. It is noted that the EB-induced C_{60} polymer exhibited a metallic property at RT in air and the metallic character remained unchanged after air-exposure for at least two weeks. This indicates that the present metallic C_{60} polymer was very stable in the presence of oxygen and water vapor and could be easily applied to conventional LSI nanofabrication processes.

The temperature-dependence of resistance should be measured for the EB- induced C_{60} polymer in order to distinguish between metal (or semi-metal) and semiconductor. As described in the previous section, the present experimental set-up, however, achieved the temperature variation only from RT to about 373 K, which was not enough to discuss the origin of metallic behavior shown in Fig. 3. To reveal

the origin of the metallic property is a further study of the present work. In the present work, the most fascinating finding is that insulating C_{60} films show a metallic property in air at RT after EB irradiation.

B. Photoelectron Spectra

Figure 4 shows (a) UPS whole spectra of the EB-irradiated C_{60} film along with HOPG and (b) their magnified spectra around the Fermi level (E_F), where the pink, sky-blue and orange lines denote the UPS spectrum of the 20-h EB-irradiated C_{60} film, the 50-h EB-irradiated C_{60} film, and HOPG, respectively. As shown in Fig. 4(a), the narrow bands of the pristine C_{60} film in the energy range of 0 – 15 eV became broader by EB-irradiation. In addition, the whole spectrum of both EB-irradiated films (20-h and 50-h) was quite different from that of HOPG except in binding energy around 15 eV. In accordance with this broadening, the density of states (DOS) for the EB-irradiated film increased near E_F more than that for HOPG.

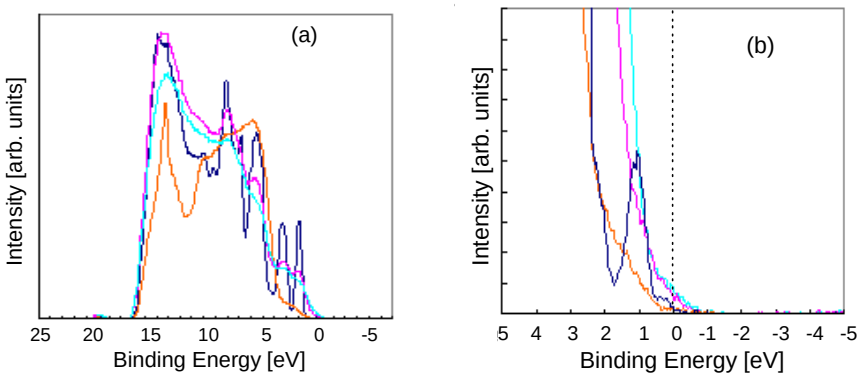

Figure 4. (a) UPS whole spectra of the electron-beam-irradiated C_{60} film and HOPG, and (b) its magnified spectra near the Fermi level: pristine C_{60} film (blue), after 20-h EB-irradiation (pink), after 50-h EB-irradiation (sky blue), and HOPG (orange).

Figure 4(b) shows the magnified spectra around E_F. A weak peak appears at around 1 eV in binding energy for the pristine C_{60} film. This is attributed to a satellite of the intense narrow HOMO excited by the He Iβ (23.1 eV) emission line included in the present non-monochromatized He I light source, because a He I line with emission due to its satellites subtracted provided no such the peak at around 1 eV [31]. This peak is, therefore, neglected in the present discussion. For HOPG graphite as a semi-metal, the DOS should appear at E_F. As can be seen clearly in Fig. 4(b), the orange line well expresses the semi-metallic feature of graphite. On the other hand, the DOS of the C_{60} film became larger than that of HOPG with increasing EB irradiation time and came across the E_F to some extent. This suggests that the EB-irradiated C_{60} film is more conducting than graphite. Accordingly, the EB-irradiated film changed from a semiconductor to a semi-metal or metal as a new π-electron-conjugated system at the present stage. For low-dimensional materials in their metallic phase (for example, quasi-one-dimesional materials), no evidence of the Fermi step can be detected, though

the Fermi discontinuity of the DOS was not clearly observed, as in bulk metals [32]. It is of further interest to clarify the dimension of the peanut-shaped C_{60} polymer structure from the standpoint of the electronic properties.

To understand the metallic properties of the EB-irradiated C_{60} film obtained in air at RT [21], we next examined the valence structure of the 50-h EB-irradiated C_{60} film after air-exposure. Figure 5(a) shows the UPS spectra of the film before (sky blue) and after 5 days of air-exposure (green) together with that of HOPG (orange). As shown in Fig. 5(a), although the DOS of the film decreased after air-exposure, the DOS was still similar to that of HOPG around E_F, indicating that the EB-irradiated C_{60} film exhibits a metallic feature even after air-exposure. This is the origin of the linear I—V curve obtained in the previous result [21].

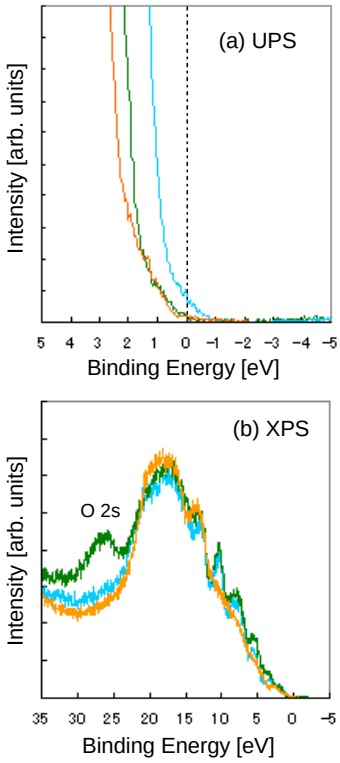

Figure 5. (a) UPS spectra of the 50-h EB-irradiated C_{60} film before and after air-exposure near the Fermi level. (b) Valence XPS spectra of the 50-h EB-irradiated C_{60} film before and after air-exposure: before air-exposure (sky blue), after air-exposure (green), and HOPG (orange).

How did the EB-irradiated C_{60} film maintain its metallic properties even after 5 days of air-exposure? To clarify this issue, we measured the valence XPS spectrum of the 50-h irradiated C_{60} film before and after air-exposure, along with that of HOPG graphite. As shown in Fig. 5(b), a new broad intense peak appeared in the range of 25 – 30 eV in binding energy after air-exposure. Because this peak is attributed to

the O 2s orbital of oxygen atom chemically bound to organic polymers [33], it is considered that molecular oxygen was chemisorbed onto the reactive site, such as in the region of negative curvature of the peanut-shaped structure shown in Fig. 2, and dissolved to form C=O or C-O-C onto the peanut-shaped polymer. However, the atomic ratio of oxygen to carbon changed from 0.8 at% to 5.0 at% even after the air-exposure, which corresponds to 1.5 oxygen molecules per one C_{60} molecule. This allows us to consider that molecular oxygen was adsorbed only on the surface layers of the EB-irradiated C_{60} film but did not diffuse into its bulk, so that the metallic feature of the film was not significantly affected by air-exposure.

C. The origin of the metallic properties

Why does the peanut-shaped connections lead the EB-induced polymer to exhibit a metallic character? In order to elucidate the origin of this metallic property, we next examined the highest occupied molecular orbital (HOMO) and the lowest unoccupied molecular orbital (LUMO) of the peanut-shaped C_{60} dimer (see Fig. 2) that is regarded as the basic unit of the EB-induced polymer. Figure 6 shows the wave function of the HOMO and LUMO for the peanut-shaped dimer. It was clearly found that no nodes are formed on the cross-linkage region between adjacent C_{60} molecules and the HOMO spread over the whole dimer structure.

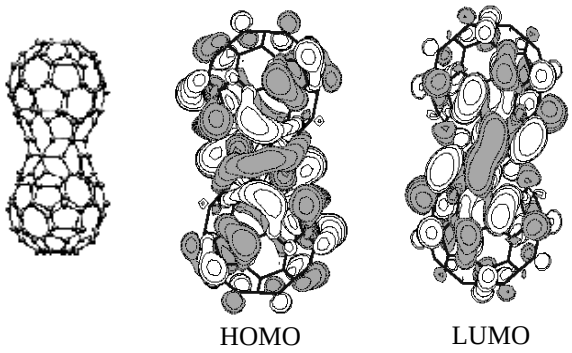

Figure 6. The wavefunctions of the highest occupied molecular orbital (HOMO) and the lowest unoccupied molecular orbital (LUMO) of the peanut-shaped C_{120}, which were obtained using the ADF program.

This indicates that electrons can move freely from one C_{60} to another without excitation, unlike the dumbbell-type polymer [9]. Namely, the peanut-shaped linkage between C_{60} molecules makes a π-conjugated system enlarged over the whole polymer. Accordingly, the EB-induced C_{60} polymer has essentially no energy gap so as to exhibit a metallic property.

The whole structure of the EB-induced C_{60} polymer with a peanut-shaped bonding is not clearly understood at this stage. However, judging from the fact that the EB-induced polymer exhibits a metallic property in the size of 100 μm (see Fig. 3), a low-dimensional peanut-shaped polymer (see Fig. 7) is one of possible structures for this conducting polymer. To verify the low-dimensional structure is now in progress using scanning probe microscopy in combination with DFT calculations [34].

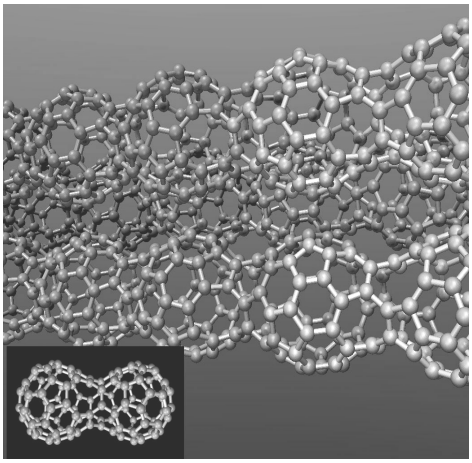

Figure 7. Schematic representation for a possible structure of the EB-induced conducting C_{60} polymer.

V. SUMMARY

To the best of our knowledge, the present work has first demonstrated that EB irradiation of C_{60} films forms a new metallic C_{60} polymer with a drastically decrease in resisitivity of 1-10 Ωcm compared to that of $10^8 – 10^{14}$ Ωcm for pristine solid C_{60}.

In situ valence photoelectron spectroscopy demonstrated that the electronic structure of the EB-irradiated C_{60} film becomes closer to that of graphite as the EB-irradiation time increases, and that the DOS around E_F was eventually greater than for graphite. This indicates that the electronic structure of a C_{60} film was changed from a semiconductor to a semi-metal and/or metal after EB irradiation. It is interesting to note that the DOS at Fermi edge for the peanut-shaped polymer is very similar to that for one-dimensional metal materials.

Even after the film was exposed to air for 5 days, the electronic structure still remained metallic, which is the origin of the linear I—V curve of the EB-irradiated C_{60} film obtained in air at RT [21].

On the basis of the DFT calculations for the HOMO and LUMO of the peanut-shaped dimer as a basic unit of the EB-induced C_{60} polymer, we explained qualitatively the origin of the electronic property of the polymer.

Because EB is currently used for nanolithography and the EB-induced C_{60} polymer is insoluble in organic solvents, the present work indicates the possibility of applying C_{60} molecules in conventional LSI nano-fabrication processes and great potential for developing carbon-based nano-devices.

ACKNOWLEDGMENTS

The present work was supported in part by Sumitomo Science Foundation and Iketani Science & Technology Foundation, in part by the Program of Core Research for Evolutional Science and Technology (CREST) and of the Precursory Research for Embryonic Science and Technology (PRESTO), Japan Science and Technology Agency, and in part by a Grant-in-Aid for Scientific Research of the Ministry of Education, Culture, Sports, Science, and Technology of Japan.

The author (J.O.) also expresses his thanks to Drs. A. Nakao and T. Hara (RIKEN), Dr. T. Nakayama (NIMS), Prof. M. Aono (Osaka Univ.), Dr. A. Hida (Tokyo Inst. Technol.), Prof. T.A. Beu (Univ. "Babes-Bolyai"), and Prof. K. Ohno (Yokohama National Univ.) for collaborating the present and future works.

REFERENCES

1. A.M. Rao, P. Zhou, K.-A. Wang, G.T. Hager, J.M. Holden, Y. Wang, W.-T. Lee, X.-X. Bi, P.C. Eklund, D.S. Cornett, M.A. Duncan, I.J. Amster, Science **259**, 955 (1993).
2. A.M. Rao and P.C. Eklund, Fullerene Polymers and Fullerene Polymer Composites (P.C. Eklund and A.M. Rao eds.), Springer, Berlin, p.145 (2000).
3. J. Onoe and K. Takeuchi, Phys. Rev. B **54**, 6167 (1996).
4. K. Esfarjani, Y. Hashi, J. Onoe, K. Takeuchi, and Y. Kawazoe, Phys. Rev. B **57**, 223 (1998).
5. J. Onoe, A. Nakao, and K. Takeuchi, Phys. Rev. B **55**, 10051 (1997).
6. J. Onoe and K. Takeuchi, Phys. Rev. Lett. **79**, 2987 (1997).
7. T. Nakayama, J. Onoe, K. Takeuchi, and M. Aono, Phys. Rev. B **59**, 12627 (1999).
8. T. Nakayama, J. Onoe, K. Nakatsuji, J. Nakamura, K. Takeuchi, and M. Aono, Surf. Rev. Lett. **6**, 1073 (1999).
9. J. Onoe, T. Nakayama, M. Aono, and T. Hara, J. Appl. Phys. **96**, 443 (2004).
10. T. Hara, J. Onoe, H. Tanaka, Y. Li, K. Takeuchi, Jpn. J. Appl. Phys. **39**,1872 (2000).
11. T. Hara, J. Onoe, and K. Takeuchi, J. Appl. Phys. **92**, 7302 (2002).
12. T. Hara and J. Onoe, Eur. Phys. J. D **24**, 389 (2003).
13. Y.B. Zhao, D.M. Poirier, R.J. Pechman, and J.H. Weaver, Appl. Phys. Lett. **64**, 577 (1994).
14. T. Tada and T. Kanayama, Jpn. J. Appl. Phys. **35**, L63 (1996).
15. M.R.C. Hunt, J. Schmidt, and R.E. Palmer, Appl. Phys. Lett. **72**, 323 (1998); Phys. Rev. B **60**, 5927 (1999).
16. R.F. Egerton and M. Takeuchi, Appl. Phys. Lett. **75**, 1884 (1999).
17. A. Khan, N. Kojima, M. Yamaguchi, K.L. Narayanan, and O. Goetzberger, J. Appl. Phys. **87**, 4620 (2000).
18. L. Bolotov and T. Kanayama, Appl. Phys. Lett. **81**, 1684 (2002).
19. Y. Nakamura, Y. Mera, and K. Maeda, Appl. Phys. Lett. **77**, 2834 (2000)
20. Y. Nakamura, F. Kagawa, K. Kasai, Y. Mera, and K. Maeda, Surf. Sci. **528**, 151 (2003).
21. J. Onoe, T. Nakayama, M. Aono, and T. Hara, Appl. Phys. Lett. **82**, 595 (2003).
22. C. Wen, J. Li, K. Kitazawa, T. Aida, I. Honma, H. Komiyama, and K. Yamada, Appl. Phys. Lett. **61**, 2162 (1992).
23. J. Mort, R. Ziolo, M. Machonkin, D.R. Huffmann, M.I. Ferguson, Chem. Phys. Lett. **186**, 284 (1991). In this paper, the samples were not purified and, although dominantly C_{60}, undoubtedly contained substantial amounts of C_{70}. It is assumed that the controlling molecule is C_{60}.
24. J. Onoe, A. Nakao, and A. Hida, Appl. Phys. Lett., in press.
25. J. Onoe, T. Nakayama, M. Aono, and T. Hara, J. Phys. Chem. Solids **65**, 343 (2004).
26. A.J. Maxwell, P.A. Bruhwiler, A. Nilsson, N. Martensson, and P. Rudolf, Phys. Rev. B **49**, 10717 (1994).
27. The present DFT calculations were carried out using the Amsterdam density-functional program (ADF 2.3.0, Theoretical Chemistry, Vrije Universiteit, Amsterdam).

28. T. Hara, J. Onoe, and K. Takeuchi, Phys. Rev. B **63**, 115412 (2001).
29. When an inter-probe distance (L) is much larger than the film thickness (t), the sheet resistance (R_s) of the film was evaluated in terms of $R_s = 4.532*(V/I)$, and the resistivity (ρ) was calculated from $\rho = R_s*t$. Here, V is the voltage difference between the inner two probes and I is the current flow between the outer two probes.
30. Since the sheet resistance apparently depends on the current flowing between the outer two probes in Fig. 4, the measured resistance does not correspond to the carrier density of the photopolymerized C_{60} film. The carriers of the film are apparently supplied by the biased metal probe during this measurement.
31. M.R. Hunt, P. Rudolf, and S. Modesti, Phys. Rev. B **55**, 7882 (1997).
32. B. Dardel, D. Malterre, M. Grioni, P. Weibel, Y. Baer, and F. Lévy, Phys. Rev. Lett. **67**, 3144 (1991).
33. G. Beamson and D. Briggs, *High Resolution XPS of Organic Polymers*, John Wiley & Sons, New York (1992).

STUDIA UNIVERSITATIS BABEŞ-BOLYAI, PHYSICA, XLIX, 2, 2004

DNA BASE MOLECULES ON SILICON SURFACES STUDIED BY OPTICAL SPECTROSCOPY WITH HIGH SURFACE SENSITIVITY

DIETRICH R. T. ZAHN*, SIMONA D. SILAGHI

**Institut für Physik, TU Chemnitz, D-09107 Chemnitz, Germany*

ABSTRACT. Amongst biomolecules the DNA base molecules adenine, cytosine, guanine, and thymine may also find interesting applications in organic electronics. They have optical gaps in the near ultra-violet and have already been considered as charge transport molecules in organic field effect transistors. Still there is very little knowledge on their electronic and optical properties when deposited as layers on inorganic substrates. Here the growth of the DNA bases deposited on vicinal, hydrogen passivated Si(111) substrates is studied using reflectance anisotropy spectroscopy (RAS). The RAS response of the DNA bases is monitored as a function of thickness. Ordering in the layers is induced by the step and terrace structure of the vicinal Si substrates. Even though the molecular structure is not dramatically different the RAS response is very distinct and allows an unambiguous identification of the base molecules.

1 Introduction

The usage of DNA base molecules as charge transport molecules in biomolecular electronic and optoelectronic devices is still a challenge. Recently, field effect transistor studies based on a modified DNA base revealed that the prototype bio-transistor gives rise to a better voltage gain compared to carbon nanotubes (CNTs) [1]. Silicon can be patterned in many ways and it is possible to use it as a versatile template and combine biomolecules with silicon electronics. Flat Si(111) has a 3-fold symmetry inducing the growth of three equivalent superstructure domains by symmetry, but vicinal Si(111) surfaces can limit overlayer growth to a single domain. Moreover, vicinal surfaces should favour the nucleation along the step edges, thus being potential substrates in controlling the ordering of molecules in so-called molecular nano-wires. In this sense, *in situ* reflectance anisotropy spectroscopy (RAS) is employed in ultra-high vacuum (UHV) conditions for monitoring the ordering of DNA base molecules on vicinal hydrogen passivated Si(111).

2 Experimental

Vicinal p-type (B-doped) Si (111) surfaces with resistivity in the range of 1-30 Ωcm were used as substrates for the DNA base films. Prior to biomolecular deposition, the substrates were wet-chemically hydrogen terminated [2]. The vicinal Si(111) surfaces were off cut oriented by 3° and 6°, respectively, towards the $\left[\bar{1}\bar{1}2\right]$ direction. The surface reconstruction (1x1) was checked by low energy electron diffraction (LEED). In the case of the vicinal surfaces the LEED pattern shows a double splitting of the diffraction points in the $\left[\bar{1}\bar{1}2\right]$ direction typical for the formation of

steps and terraces. The source materials of high-purity DNA base powders purchased from Sigma-Aldrich were evaporated under UHV conditions (base pressure ~ 10^{-8}Pa) from Knudsen cells. Molecules of thymine and cytosine were evaporated at temperatures of 365 and 410 K with corresponding evaporation rates of 0.8 and 0.3 nm/ min, respectively, while adenine and guanine molecules were evaporated at temperatures of 400 and 510 K with evaporation rates of 1.5 and 2 nm/min, respectively. The thicknesses were *in situ* monitored via a quartz crystal microbalance and then *ex situ* calibrated via both ellipsometry and atomic force microscopy film thickness measurements.

The molecular ordering of DNA base molecules on both vicinal and "flat" H:Si(111) surfaces was monitored *in situ* during the growth by reflectance anisotropy spectroscopy (RAS) in the energy range of 1.5-5.5 eV. RAS measures the difference in normal incidence in reflection for light linearly polarized along two orthogonal directions in the sample surface. In the case of a vicinal Si(111) surface the RAS signal can be expressed as follows:

$$\frac{\Delta r}{r} = \mathrm{Re}(\frac{\Delta r}{r}) + i\,\mathrm{Im}(\frac{\Delta r}{r}) = 2\frac{r_{[1\bar{1}0]} - r_{[\bar{1}\bar{1}2]}}{r_{[1\bar{1}0]} + r_{[\bar{1}\bar{1}2]}} \qquad (1)$$

Due to the fact that RAS is performed in normal incidence the technique is very sensitive to surface changes and capable of measuring very small optical anisotropies of 10^{-3} or even smaller.

3 Results

The anisotropy of cubic materials, e.g. silicon, arises at the surface due to a broken symmetry as in the case of vicinal Si(111) substrates where the surface anisotropy is induced by the formation of steps and terraces. Such anisotropy is often referred to as surface induced optical anisotropy (SIOA) [3, 4]. The RAS signal of vicinal Si(111) surfaces is similar with the response of Si(110) surface as shown in fig.1. The fractional contribution of the $[110]$ direction to the vicinality of (111) surface can be determined from the ratio between the magnitude of the E_2 peak for the vicinal surface and that for the (110) surface [2]. The values determined experimentally from the spectra are about 0.08 and 0.17 corresponding to 3° and 6° off cut angles which are quite close t o the expected theoretical values of 0.09 and 0.18.

Figure 2 depicts the *in situ* RAS monitoring of DNA base layers on vicinal H:Si(111)-6° surfaces. During the RAS measurements the substrate geometry was always kept identical with the one sketched in fig.1. All four molecules behave optically different when deposited onto the vicinal surface. Very small anisotropies are observed in the case of guanine and cytosine in comparison with the large RAS signals arising from adenine and thymine layers. When increasing the guanine coverage the RAS signal reaches a saturation level for thicknesses above 30 nm. The amplitude of the silicon features increases with thickness. Larger changes can be observed around the silicon E_2 gap which overlaps with the absorption of guanine since the onset is around 3.5 eV. Moreover, the HOMO-LUMO gap of guanine at 4.31 eV is extremely close to the 4.25 eV energy gap of silicon. The lineshape of the

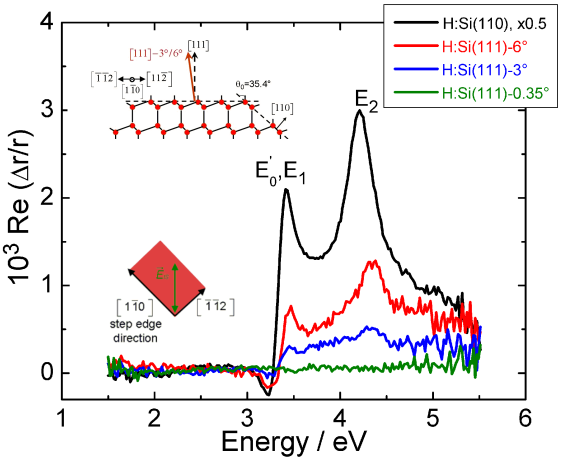

Fig. 1 RAS spectra of various silicon surfaces.

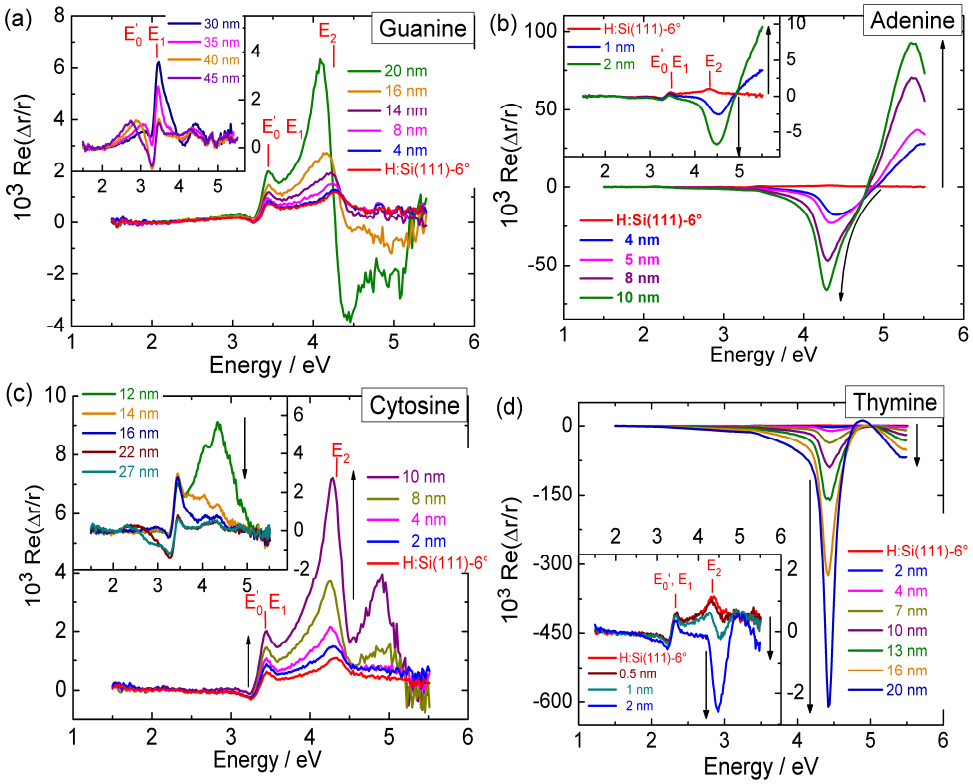

Fig. 2 *In situ* RAS spectra of monitoring: (a) guanine, (b) adenine, (c) cytosine, and thymine layers on H:Si(111)-6°surface.

signal evolves in a derivative-like lineshape with increasing guanine coverage above 14 nm. For coverage above 20 nm the signal starts to decrease and finally saturates for thicknesses around 30 nm as shown in the inset of fig. 2 (a). This can be related to the fact that the molecules form an isotropic layer and consequently the signal vanishes due to equal absorption in orthogonal directions. In order to distinguish between the anisotropy of the substrate and the anisotropy of the guanine films, RAS measurements of guanine deposition on almost flat H:Si(111)-0.35° were carried out (see fig. 3(a)). The observed features are attributed to thickness artifacts. The weak anisotropy of guanine films on vicinal substrates seems to be caused by the vicinality which induces ordering of the guanine molecules up to critical thickness of about 20 nm.

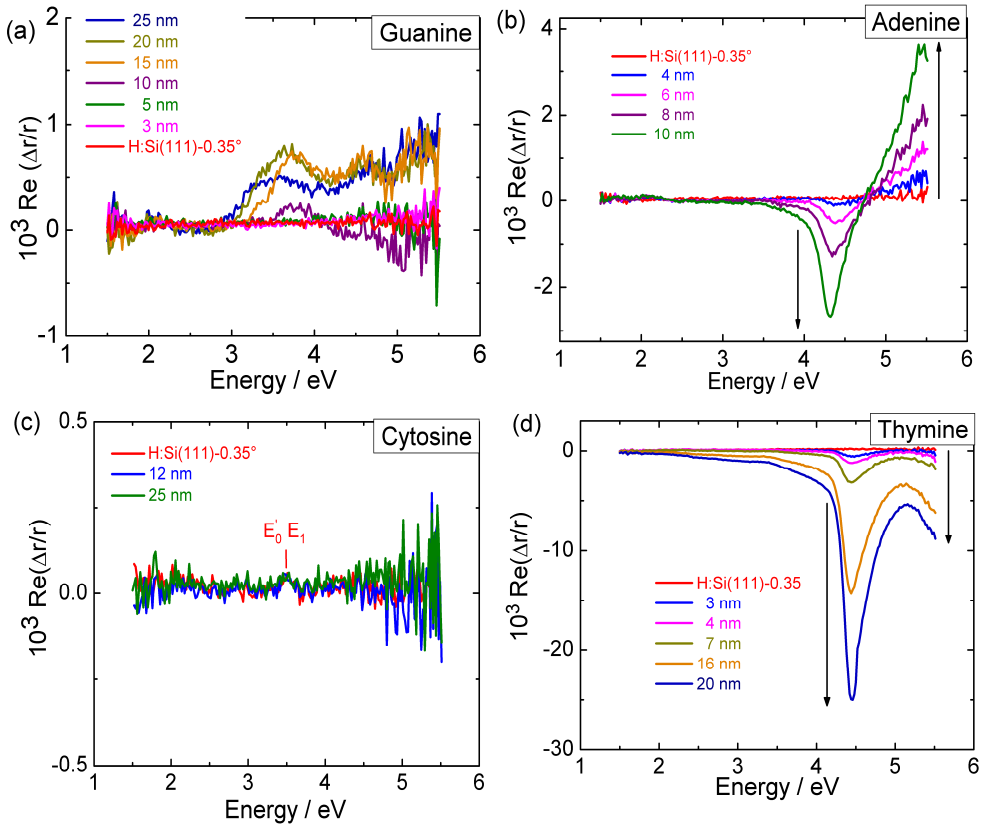

Fig. 3 *In situ* RAS spectra of monitoring: (a) guanine, (b) adenine, (c) cytosine, and thymine layers on "flat" H:Si(111)-0.35°surface.

On the contrary to guanine, adenine exhibits large anisotropy signals. By increasing the adenine coverage the RAS signal evolves in a derivative-like lineshape in the absorption range of adenine while the silicon features gradually vanish. The asymmetric evolution in the lineshape of the derivative-like RAS signals indicates

the contribution of at least two oscillators above 4 eV. Following the surface dielectric anisotropy model [5] it is found that the dominant absorption takes place mainly along $\left[\bar{1}\bar{1}2\right]$ direction suggesting furthermore strong ordering of adenine molecules with respect to this direction. Weak anisotropy can be observed with a similar derivative-like lineshape also on the almost flat silicon surface (fig. 3 (b)). Such small anisotropies were not observed by ellipsometry. The RAS monitoring of cytosine deposition on H:Si(111)-6° shows that the lineshape of the signal is strongly thickness-dependent as in the case of guanine. Larger changes can be observed around the E_2 gap of silicon at 4.25 eV which overlaps with the absorption of cytosine with the onset at 3 eV. At certain cytosine coverage a new feature around 4.90 eV appears which is closed to the second electronic transition at 4.95 eV as obtained from ellipsometry results. For very thin cytosine coverages, the molecules seem to preferentially align on vicinal surfaces with respect to the $\left[1\bar{1}0\right]$ direction. Already for higher coverage larger than 12 nm the signal starts to decrease and finally saturates for thicknesses around 20 nm as shown in inset fig. 2(c). There is no anisotropy of the cytosine layers on H:Si(111)-0.35° meaning that the anisotropy of cytosine on vicinal substrates is caused by the vicinality which induces ordering of the cytosine molecules up to critical thickness of ~ 10 nm.

The strongest RAS signals were observed in the case of thymine layers on H:Si(111)-6° as reproduced in fig. 2 (d). By increasing the thymine coverage the RAS signal of the substrate completely vanishes while large anisotropy signals appear in the absorption range of the molecule. The lineshape of the RAS signal of thymine is very much like ε derived from ellipsometry results not discussed here. The negative sign of the signal suggests high absorption along $\left[\bar{1}\bar{1}2\right]$ direction and hence a preferential alignment of the transition dipole moments of the molecule parallel to the same direction. Smaller anisotropies were also observed on “flat” silicon substrates but still larger signal amplitudes compared to the case of adenine layers on the same type of substrate (see fig. 3 (d)).

4 Summary

The RAS technique was employed for the first time in monitoring the growth of DNA base molecules on both flat and vicinal H:Si(111) surfaces. The RAS measurements revealed information about the molecular ordering of DNA bases induced by the density of steps on silicon surfaces.

ACKNOWLEDGMENTS

The financial support by Sächsisches Staatsministerium für Wissenschaft und Kunst (SMWK), Deutsche Forschungsgesellschaft Graduiertenkolleg GRK 829/1 “Accumulation of Single Molecules to Nanostructures” and the BMBF project 05 622 ESA2 is acknowledged.

REFERENCES

[1]. Mauricio, P. Visconti, V. Arima, S. D'Amico, A. Biasco, E. D'Amone, R. Cingolani, and R. Rinaldi, Nanoletters **3** (2003) 479
[2]. Yasuda, D. E. Aspnes, D. R. Lee, C. H. Bjorkman, G. Lucovsky, J. Vac. Sci. Technol. **A 12** (1994) 1152
[3]. D. E. Aspnes, J. Vac. Sci. Technol. **B 3** (1985) 1498
[4]. D. E. Aspnes, A. A. Studna, J. Vac. Sci. Technol. **A 5** (1987) 546
[5]. R. J. Cole, B. G. Frederick, P. Weightman, J. Vac. Sci. Technol. **A 16** (1998) 3088

STUDIA UNIVERSITATIS BABEŞ-BOLYAI, PHYSICA, XLIX, 2, 2004

METHODS TO CONTROL PIGMENT INCORPORATIONS INTO MEMBRANES

HORST A. DIEHL[1], CARMEN SOCACIU[2], ADELA PINTEA[2] and MEDHAT WAHBA SHAFAA[1]

[1] Institute of Biophysics, University of Bremen, Germany
[2] Department of Chemistry and Biochemistry, University of Agricultural Sciences and Veterinary Medicine, Cluj-Napoca, Romania

Introduction

Permeable membranes are basic structural and functional constituents of living systems. All biological membranes possess a common basic structure. Vertical dimensions range up to about 10 nm. The high variety of membrane components (lipids, proteins, sterols, pigments, etc.) causes a high variety of constitutional conformations. The forces which keep together the structure are of covalent, ionic or entropic nature. According to this wide frame, the physical properties of biological membranes are subjected to local and temporal changes. Most important physical membrane properties are membrane fluidity, active and passive membrane permeability, membrane anisotropy and the ability to incorporate molecules from the extracellular space being biotics or xenobiotics. The incorporation of molecules may have adverse biological effects on membranes like toxins. Or they may constitute the biological function of the membrane as is the case with pigments. Carotenoids are a class of pigments which are widely abundant in nature with more than 600 molecular species. Many of them are of profound significance for life: light harvester in photosynthesis, vitamin A precursors in the vision process, UV protection function in the eye, pigmentation of many plants, animal skins and feathers, antioxidative and antibiotic actions. The knowledge about these and many other health beneficial effects are of empirical origin. Biophysical and biochemical action mechanisms are poorly understood so far. Carotenoids are more or less lipophilic compounds and their action is bound mainly to membranes. How do carotenoids pass or incorporate into membranes, how do they locate in membranes, how stable are they and what is their specific impact on the membrane? And which methods promise access to answers?

Relevant physical methods are Nuclear Magnetic Resonance Spectroscopy, Spin Label Electron Resonance Spectroscopy, Differential Scanning Calorimetry, Fluorescence Spectroscopy and Fluorescence Microscopy. The fluorescence techniques are specifically sensitive and broadly applied. Fluorophores are incorporated into the membranes and the resulting fluorescence properties (quenching, spectral shifts, depolarisation, fluorescence life time) are used for the evaluation of membrane properties. Here we deal with fluorescence spectroscopy The quality of the evaluation depends on the knowledge how the resulting and the intrinsic molecular fluorescence are related to each other. Therefore the molecular physics of the fluorophore must be known.

Experimental

The processes which determine fluorescence emission properties are lateral or rotational diffusions, intermolecular and intramolecular interactions. For biophysical applications there is not just one fluorophore which serves all demands. The main question always is which fluorescence parameter is sensitive against the membrane parameter one wants to examine. In recent years the lipophilic fluorophores Prodan (6-propionyl-2-dimethylaminonaphtalene) and Laurdan (6-dodecanoyl-2-dimethylaminonaphtalene) have been used very successfully. PRODAN possessing a short hydrocarbon is mainly applied to investigate surface interactions of membranes whereas Laurdan reports more about interior membrane properties [1, 2].

Membrane anisotropies we determined from the rotational fluorescence depolarisation of DPH (1-6-diphenyl-1,3,5-hexatriene) or TMA-DPH (1-(4-trimethyl-ammoniumphenyl)- 6-phenyl-1,3,5-hexatriene). An important result was that membrane anisotropy limits the ability of membranes to incorporate pigments and drugs. Pyrene and some of its derivatives, by its ability to form membrane fluidity correlated excimers, and by its micropolarity dependent pyrene monomer fingerprint characteristic, we used to dermine the lateral diffusion in membranes, and to evaluate the polarity of the microenvironment, respectively. Moreover, pyrene can be excited by direct excitation or via membrane intrinsic tryptophane and radiationless energy transfer to pyrene, which gives a report how near pyrene is located to the membrane proteins. [3-12].

Unfortunately, most fluorescent dyes which sense dynamically relevant membrane parameters are UV sensitive. They are susceptible to fluorescence bleaching, and UV light may damage biological membrane components. We tested a variety of non-UV fluorophores in lipid membranes at different temperatures and at different concentrations of cholesterol, two parameters which modulate membrane fluidity: Nile red (9-diethylamino-5H-benzophenoxazine-5-one), DCVJ (4-(dicyanovinyl)julolidine), FM4-64(N-(3-triethylammoniumpropyl)-4-(4-(dibutylamino) styryl)pyridinium dibromide), $DiIC_{18}$ (1,1'-dioctadecyl-3,3,3',3'-tetra-methylindocarbo-cyanine perchlorate) and its derivatives with shorter chain lengths, $DiIC_{16}$ and $DiIC_{12}$, and "Fast $DiIC_{18}$" which contains double bonds at the 9th and 12th carbon atom of each chain, and we incorporated the fluorescent phospholipid analogue C_6-NBD-PC (Hexanoyl (7-nitro-2,1,3-bezoxadiazol-4-yl)1,2-dipamitoyl-*sn*-glycero-3-phosphorylcho-line) [13, 14]. A finding is that at least with respect to cholesterol variation in membranes, the non-UV fluorescent dyes unfortunately do not exert an as high sensitivity parameter as do DPH and its derivatives and Laurdan. And with respect to membrane temperature variations, Laurdan is most superior. Generally Laurdan is favourable as far as no biological damage occurs.

Laurdan presents a spectrally inhomogeneous system. Dissolved in glycerol, Laurdan in the ground and excited state takes up simultaneously a set of various conformations. The spatial conformations differ in their intramolecular twisting angle, representing a locally excited (LE) or a charge transfer (CT) state which are in a thermal balance [15, 16]. Laurdan belongs to a group of conjugated molecules which possess electron yielding and electron-withdrawing functional groups and undergo a large change of their dipole moment on the transition from the ground to the excited state [17]. Dipolar molecules surrounding the fluorophore will increase their state of order if they move on the time scale of the fluorophore life time. The

energy for this rearrangement is taken from the excited fluorophore, resulting in a bathochromic shift of the fluorescence emission. In lipid membranes, intruding water molecules determine the relaxing process of Laurdan. The more rigid a membrane is, the less water molecules enter the hydrophobic core of the lipid matrix. The emission ratio of the two bands, S_1(LE) and S_1(CT), depends on the microenvironment and particularly on the solvent polarity and its ability to form an intermolecular complex with the solvent molecules.

We mostly use a membrane which is either obtained from a cell culture or is prepared from the endoplasmic reticulum of liver cells (liver microsomes). To understand better the basic membrane properties biophysicists like to work on artificial membranes composed of phospholipids (liposomes) which, step by step, can approach a more natural state by incorporation of cholesterol, proteins, pigments and so on.

Results and Discussion

Lipophilic fluorophores are molecules which easily share membrane locations with carotenoids. They come into such a tight vicinity that they interact with each other and it is not always easy to discriminate if a specific fluorescence signal is determined by the membrane which has been modulated by the pigment, or if the signal is directly determined by an interaction of the fluorophore with the pigment. In any case informations about the location of the carotenoid are obtained if the location of the fluorophore is known as it is for Laurdan. Its fluorescence in membranes is strongly quenched by carotenoids. This property is proportional to the carotenoid content and can even be used to check the pigment concentrations. We performed experiments with Laurdan either solved in glycerol (Fig.1) [18]

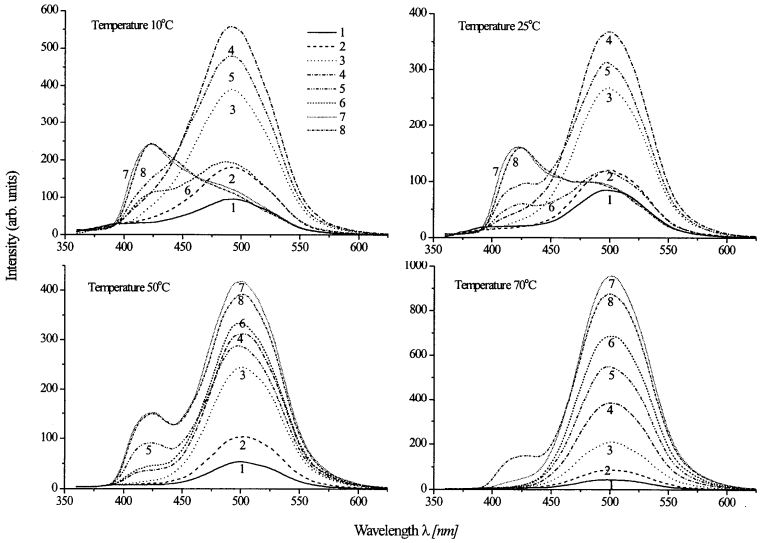

Fig. 1. Emission spectra of Laurdan at different concentrations and temperatures in glycerol. Excitation at 350 nm. Laurdan concentrations: **1 - 5x10^{-7}M, 2** - 1x10^{-6}M, **3** - 2.5x10^{-6}M, **4** - 5x10^{-6}M, **6** - 1x10^{-5}M, **7** - 2.5x10^{-5}M, **8**- -5x10^{-5}M. [18]

or incorporated into a liposomal membrane (Fig.2) [19].

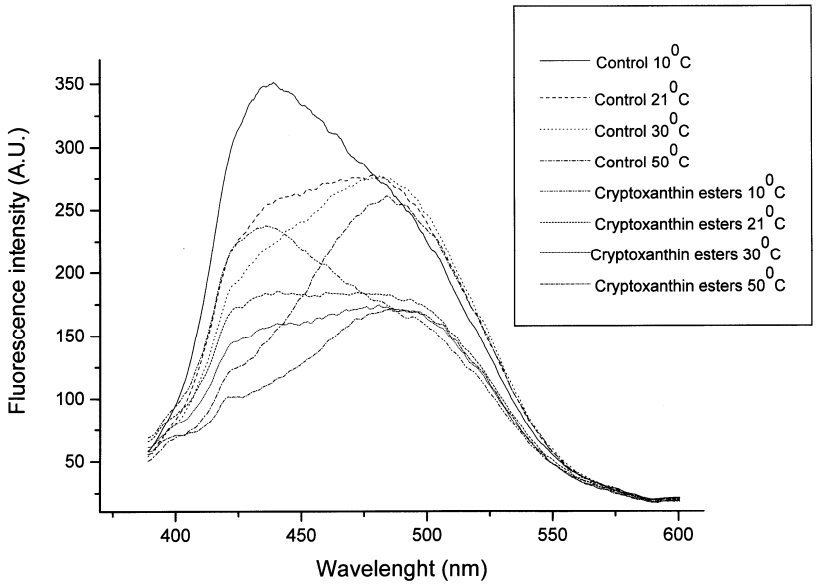

Fig. 2. Emission spectra of Laurdan in liposomes at different temperatures incubated with 2 mol% ß-cryptoxanthin as indicated. [19]

Both assays were measured at different temperatures. In both experiments we find an increase of the fluorescence emission with temperature at 500 nm (ascribed to the S_1(CT) state) and a decrease at about 420 nm (ascribed to the S_1(LE) state). The addition of cryptoxanthin esters into the liposomes results in a stronger emission band at 420 nm without changing the temperature course. The CT emission component at 500 nm originates from the S_1(CT) state which is created during the life time of the S_1(LE) excited state of Laurdan as a result of an intramolecular charge transfer between the twisted dimethylamino functional donor group and the naphtalene moiety acceptor group. Low temperature of the glycerol/Laurdan assay as well as the pigment incorporation into liposomes inhibit the charge transfer. Relaxation processes become slow and the S_1(LE) state life time, which is essentially below 1 ns [18], dominates the emission process. That's why Laurdan senses well changes of the membrane dynamics which are caused by the incorporation of carotenoids (Fig. 2, Fig. 3 [14]). The carotenoid incorporations cause a slight hypsochromic shift of the short-wavelength Laurdan emission peak. The carotenoids quench the emission strongly but most effectively in the long-wavelength range. The effect is strongest for lutein and zeaxanthin which we found to be incorporated most effectively. In the Laurdan excitation spectra we observe a slight bathochromic shift. The quenching effect is as strong in the excitation and in the emission spectra.

The incorporation of carotenoids into membranes has the same effect as a decrease of temperature in the mixture glycerol/Laurdan (Fig. 1). Laurdan is restricted in its movement and the intramolecular charge transfer in inhibted. Fig. 4, moreover,

shows that the incorporation of cholesterol instead of carotenoids into the membranes enhances strongly the direct S_1(LE) state emission, yielding the same effect as the carotenoids, but cholesterol does not quench Laurdan.

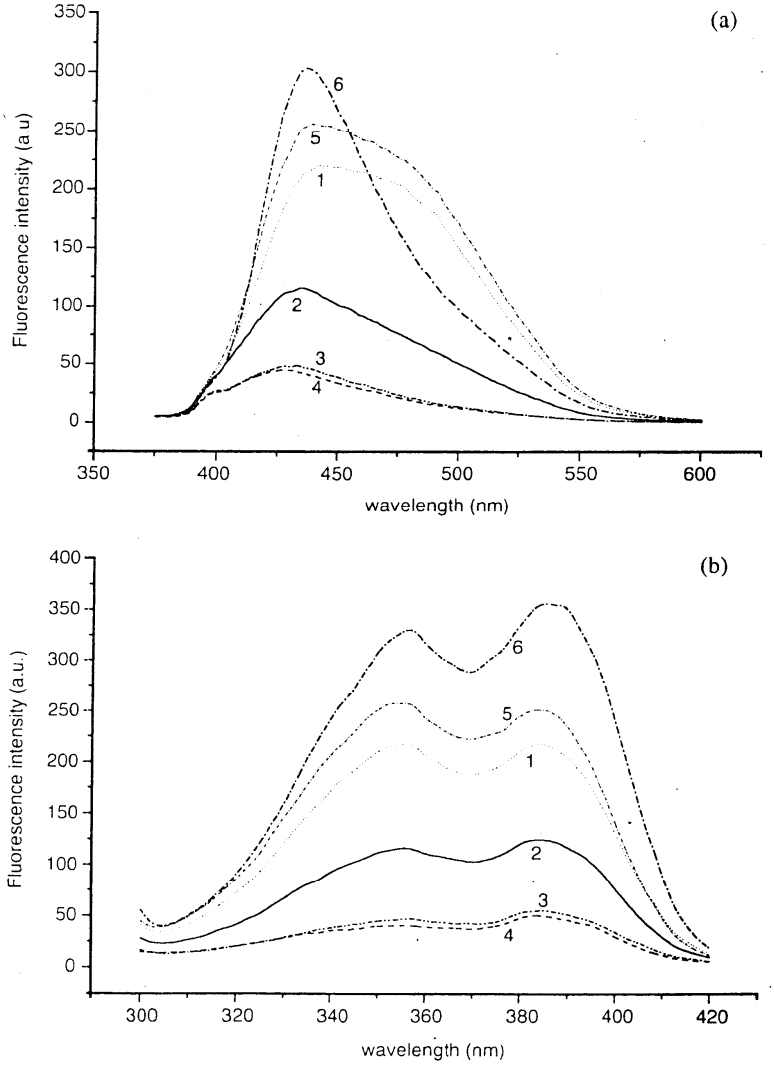

Fig. 3. Emission spectra excited at 350 nm (**a**) and excitation spectra observed at 440 nm (**b**) of Laurdan incorporated into liposomes which have been prepared from a mixture of phospholipids and carotenoids or cholesterol. **1**- control liposomes, liposomes containing: **2** - ß-carotene, **3** - lutein, **4** - zeaxanthin, **5** and **6** - a low and a high concentration of cholesterol, respectively. [14]

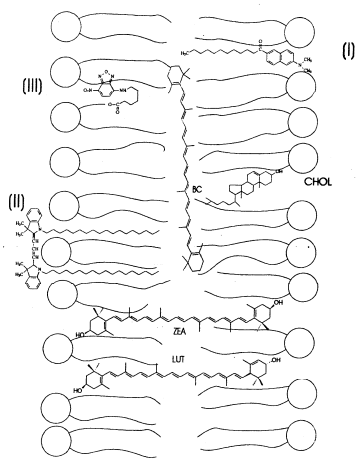

Fig. 4. Schematic drawing of the membrane bilayer containg fluorophors and cholesterol. Laurdan (I), DiC-C18 (II), C6NBD-PC (III) and the carotenoids ß-carotene (BC), lutein (LUT), zeaxanthin (ZEA). Molecular dimensions and locations are drawn in relation to the bilayer dimensions. [14]

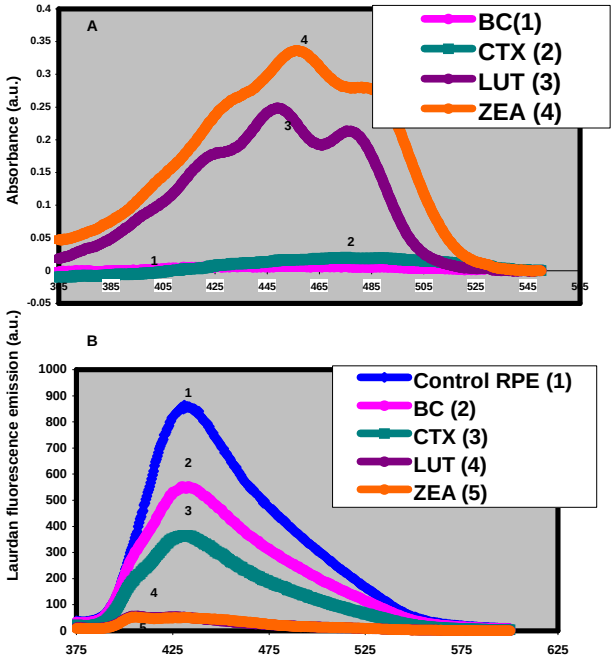

Fig. 5. RPE cell line D 407 incubated with 26 µg carotenoid/10^6cells for 48 hours. (1) ß-carotene, (2) cantaxanthin, (3) lutein, (4) zeaxanthin. A: absorption spectra taken after cell solubilisation and exraction of the carotenoids into ethanol. B: Laurdan fluorescence emission directly from the cells. [20]

Fig. 4 [14] sketches schematically the composition of the liposomal membrane with an indication how fluorophores, carotenoids and cholesterol are located. By playing the puzzle of defined incorporations into various membrane types and of discerning specific fluorescence and other optical properties one can get an imagination how concentrated, at which locations and how stable carotenoids can be found in membranes. Further investigations aim to carotenoid esters, which are highly abundant in nature, and to the mechanisms why and how just only two carotenoids, the pigments lutein and zeaxanthin, are incorporated into the retinal pigment epithelial cells, where they protect the eye from visual diseases. We used the human retinal pigment epithelial (RPE) cell line D 407 to study the incorporation of several pigments (lutein, zeaxanthin, cantaxanthin and ß-carotene) [20]. Fig. 5a demonstrates the first time that just the eye protecting pigments lutein and zeaxanthin and not the other pigments are incorporated into the RPE cells. And fig. 5b, like a mirror image, shows that the quenching of co-incubated Laurdan is just proportional to the pigment concentration in the membrane of the RPE cells.

Conclusion

Exogenous biomolecules or other macro-molecules and fluorescing reporter molecules simultaneously incorporated into membranes form nanostructured systems which can be used to detect sensitively physical membrane changes that directly can be related to membrane functions. In the case of technical membranes fluorescence detection may help to vary membrane properties like permeability on-line only by varying a streaming incubation assay. In the case of biological membranes in-vitro simulations of drug effects can be studied.

REFERENCES

1 Parasassi T., De Stasio G., D'Ubaldo A. and Gratton E. (1990) Phase fluctuation in phospholipid membranes revealed by laurdan fluorescence. Biophysical Journal 57, 1179-1186

2 Parasassi T., Di Stefano M., Loiero M., Ravadnan G. and Gratton E. (1994) Influence of cholesterol on phospholipid bilayers phase domains as detected by laurdan fluorescence. Biophysical Journal 66, 120-132

3 Kölling A., Maldonado C., Ojeda F. and Diehl H.A. (1994) Membrane fluidity of microsomal and thymocyte membranes after X-ray and UV irradiation. Radiat. Environ. Biophys. 33, 303-313

4 Engelke M., Behmann T., Ojeda F., Diehl H.A. (1994) Heterogeneity of microsomal membrane fluidity: evaluation using intrinsic tryptophan energy transfer to pyrene probes. Chemistry and Physics of Lipids 72, 35-40

5 Engelke M., Klockmann H.-C. and Diehl H.A. (1995) Gramicidin effects on the transverse and lateral distribution of pyrene and pyrene derived probes in lipid bilayers. Spectrchimica Acta Part A 51, 1939-1947

6 Engelke M., Bojarski P., Diehl H.A. and Kubicki A. (1996) Protein-dependent reduction of the pyrene excimer formation in membranes. J. Membrane Biol. 153, 117-123

7 Härtel S., Diehl H.A. and Ojeda F. (1998) Methyl-ß-cyclodextrins and liposomes as water-soluble carriers for cholesterol incorporation into membranes and its evaluation by a microenzymatic fluorescence assay and membrane fluidity-sensitive dyes. Analytical Biochemistry 258, 277-284
8 Socaciu C., Lausch C. and Diehl H. A. (1999) Carotenoids in DPPC vesicles: membrane dynamics. Spectrochimica Acta Part A 55, 2289-2297
9 Socaciu C., Jessel R., Härtel S. and Diehl H.A. (2000) Carotenoids in 1,2-dipalmitoyl-sn-glycero-3-phosphorylcholine liposomes: incorperation and effects phase transition and vesicle size. J. Med. Biochem. 4, 71-82
10 Socaciu C., Jessel R. and Diehl H.A. (2000) Competitive carotenoid and cholesterol incorporation into liposomes: effects on membrane phase transition, fluidity, polarity and anisotropy. Chemistry and Physics of Lipids 106, 79-88
11 Socaciu C., Jessel R. and Diehl H.A. (2000c) Carotenoid incorporation into microsomes: yields, stability and membrane dynamics. Spectrochimica Acta Part A 56, 2799-2809
12 Jessel R., Härtel S., Socaciu C., Tykhonova S. and Diehl H.A. (2002) Kinetics of apoptotic markers in exogeneously induced apoptosis of EL4 cells. J. Cell. Mol. Med. 6, 82-92
13 Härtel S., Tykhonova S., Haas M. and Diehl H.A. (2002) The suscseptibility of non-UV fluorescent membrane dyes to dynamical properties of lipid membranes. J. of Fluorescence 12, 465-479
14 Socaciu C., Bojarski P., Aberle L. and Diehl H.A. (2002) Different ways to insert carotenoids into liposomes affect structure and dynamics of the bilayer differently. Biophysical Chemistry 99, 1-15
15 Tomin V.I., Brozis M. and Heldt J. (2003) The red-edge effects in Laurdan solutions. Z. Naturforsch. 58a, 109
16 Brozis M., Kozyra K.A., Tomin V.I., and Heldt J. (2002) Inhomogeneous broadening of the electronic spectra of Laurdan. J. Appl. Spectr. 69, 480-483
17 Kawski A., Kuklinski B., Bojarski P. and Diehl H.A. (2000) Ground and excited state dipole moments of Laurdan determined from solvatochromic and thermochromic shifts of absorption and fluorescence spectra. Z. Naturforsch. 55a, 817-822
18 Kozyra K.A., Heldt J.R., Heldt J., Engelke M and Diehl H.A. (2003) Concentration and temperature dependence of Laurdan fluorescence in glycerol. Z. Naturforsch. 58a, 581-588
19 Pintea A., Diehl H.A., Momeu C. and Socaciu C. (2004) Incorporation of carotenoid esters into liposomes. Submitted to Biopys. Chem.
20 Shafaa M. W. (2004) PhD thesis in preparation

STUDIA UNIVERSITATIS BABEŞ-BOLYAI, PHYSICA, XLIX, 2, 2004

STRUCTURAL ANALYSIS OF NANOMOLAR QUANTITIES OF NEUROPEPTIDES USING 2D-NMR

ELENA MATEI[1,3], HERMINSUL CANO[1], FRED PFLUEGER[1] and FRANK MARI[1,2]

[1]Department of Chemistry & Biochemistry and
[2]Center for Molecular Biology & Biotechnology,
Florida Atlantic University, 777 Glades Rd.,
Boca Raton, Florida, 33431, USA
[3]"Babes-Bolyai" University, Cluj-Napoca, 3400, Romania

ABSTRACT. Cone snails (genus *Conus*) are venomous and predatory marine mollusks whose venoms contain complex mixtures of neuroactive (conopeptides). Conopeptides have been recognized as versatile and powerful neuropharmacolo-gical agents. There are potentially ~ 100,000 different conopeptides that can target neuronal receptors, present in the venom of over 1000 species of cone snails. Every conopeptide has a highly specific target; binding of the conopeptide to its target leads to a biologically relevant change in neurophysiological function. After a laborious separation procedure, nanomole quantities of native conopeptides are usually obtained. For this study, we have selected two samples: i) 30 nmoles of α-Conotoxin GI (ECCNPACGRHYSC; 2–7, 3–13), isolated from the venom of *C. geographus*, ii) 23 nanomoles of vexB, a 28-residue peptide with three disufide bonds isolated from *Conus vexilum*. Conformational analysis of nanomoles amount in aqueous solution of α-conotoxin GI, a potent peptide antagonist of acetylcholine receptor (nAChR) and vexB, a potent blocker of Ca^{2+} - ion channel, have been performed by two-dimensional NMR methods. Structural information of these conotoxins, was obtained from proton-proton internuclear distance constraints in combination with dynamical simulated annealing protocols. The limits of detection and other analytical parameters associated with the use of the nano-MAS and 1.7mm NMR probes in conopeptide research are evaluated.

Results and Discussions

Structure calculation of α-conotoxin GI

Our interest on α-conotoxin GI, a well-characterized conopeptide, has focused on its use as a model compound to explore and optimize all NMR parameters. Using a small quantity (~30nmoles) of this conopeptide, we obtained sufficient structural information to ascertain the secondary structure and enough constraints to determine its tridimensional structure.

The α-conotoxin GI a 13-amino acid peptide isolated from *Conus geographus* venom was the first Conus peptide for which a complete amino acid sequence was established, and confirmed by chemical syntesis [1]. It is also the smallest known peptide nAChR.

NMR samples were obtained by dissolving the lyophilized peptide in 90% H_2O/10% D_2O. NMR spectra were recorded at 25°C and 0°C, using TSP (0.1mM) as an internal standard. Only 30 nanomoles amount of α-conotoxin GI, yielded ^{1}H-NMR spectra of excellent quality, providing a strong indication of a well defined 3D structure.

H^1 2D-NMR homonuclear experiments (TOCSY, and NOESY) in H_2O were used, for resonance assignment and collection of distance restraints. The spin system was identified using ES-TOCSY spectra (Figure 1).

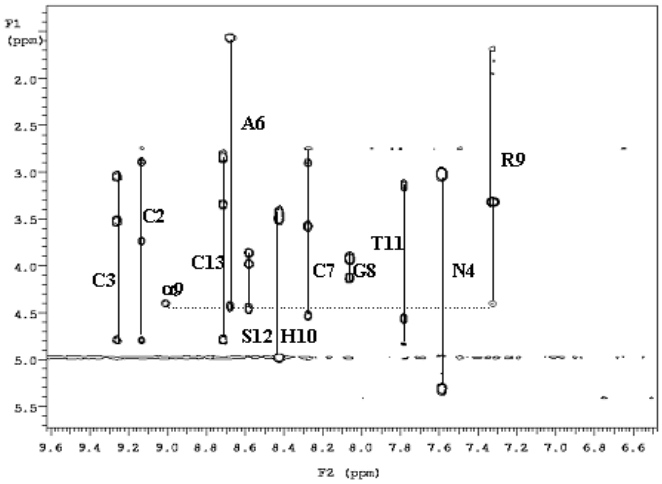

Figure1 ES-TOCSY spectra of 30 nanomoles of α-conotoxin GI @ 25°C

The 2D-wgNOESY NMR spectra of GI shows strong nOe interactions at t= 0°C (Figure 2). As we increase the temperature, the peptide exhibits a high conformational disorder, characterized by the absence of persistent tertiary interactions, as reflected in poor spectral dispersion and lack of NOEs interactions in NMR spectra. Because of a small size of the peptide the NOESY experiment performs to a temperature higher than 10 C° gives low quality spectra that can be hardly used for a structural analysis.

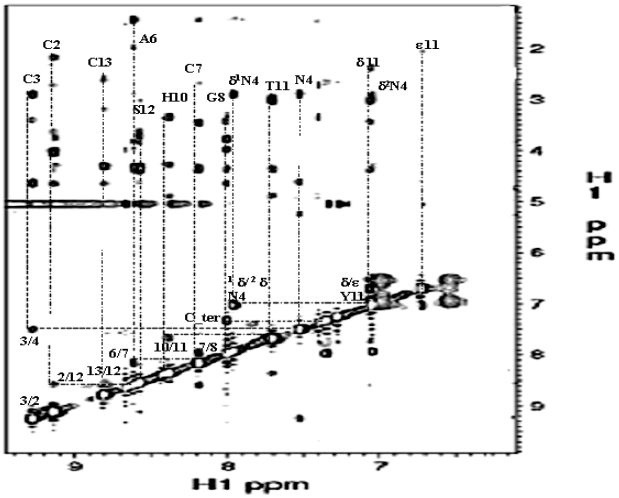

Figure2 NH-NH and αH-NH region of NOESY spectra of α-conotoxin GI @0°C

The resonance assignments were carried out using standard biomolecular NMR procedures [2]. Most of the NOE correlations expected for 3_{10} helix secondary structure elements, including $d_{NN}(i,i+1)$, $d_{NN}(i,i+2)$, $d_{\alpha N}$, $d_{\beta N}$ or $d_{\alpha\beta}(i,i+3)$, were observed throughout the peptide structure, from Pro^5 to Arg^9 (Figure 3).

NMRpipe software was used for quantification of NOE volumes and peak intensities were calibrated relative to NOEs corresponding to known interproton distance. As a distance reference, the average value of the NOE volumes corresponding to three nonoverlapping geminal β - protons cross-peaks $H^{\beta 1}$- $H^{\beta 2}$ of Cys^3, Cy^7, Cys^{13} respectively, were related with the appropriate geminal distance of 1.8 Å, and H^{γ}- H^{ε} distance of 2.5 Å known for proline aminoacid. The NOE restraints were classified into three categories: strong (1.8-2.7 Å), medium (2.7 -3.5 Å), and weak (3.5-5.0 Å).

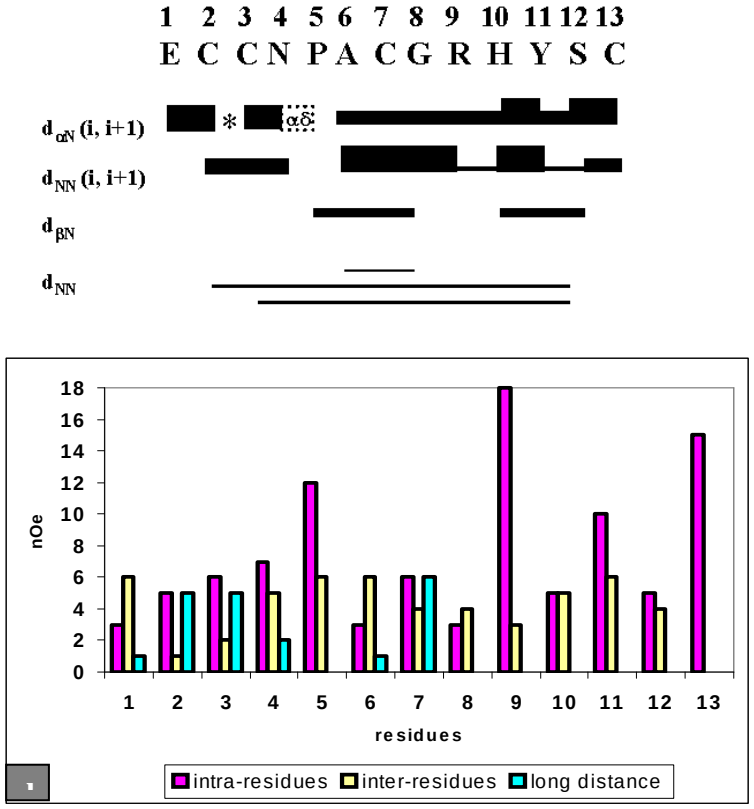

Figure3a) The secondary structure elements of α-conotoxin GI b) NMR distance restraints derived from wgNOESY spectra of α-conotoxin GI @ 0°C

A number of 167 (96 intra-residues, 52 inter-residues and 19 long distance) nOe protons connectivities were identified. The final representation of all nOe interactions are shown in Figure 4.a. A simulated annealing protocol (SA) included in XPLOR software was used to obtain three dimensional structure of α-conotoxin GI.

The total number of derived inter-proton experimental restraints were used to generate 100 structures of α-conotoxin GI. After two cycles of molecular dynamics, a final set of structures was obtained. The structures were further refined using a simulated annealing protocol and extra energy minimization step under the cvff force field. The final 32 "nano"- structures were retained on the basis of the agreement with the experimental data and the low potential energy. The first structure that is closest to the average coordinates of the ensemble, was chosen as a representative conformer and used for structural illustration (Figure 4 b). The superposition of the best 32 selected structures is shown in Figure 5.

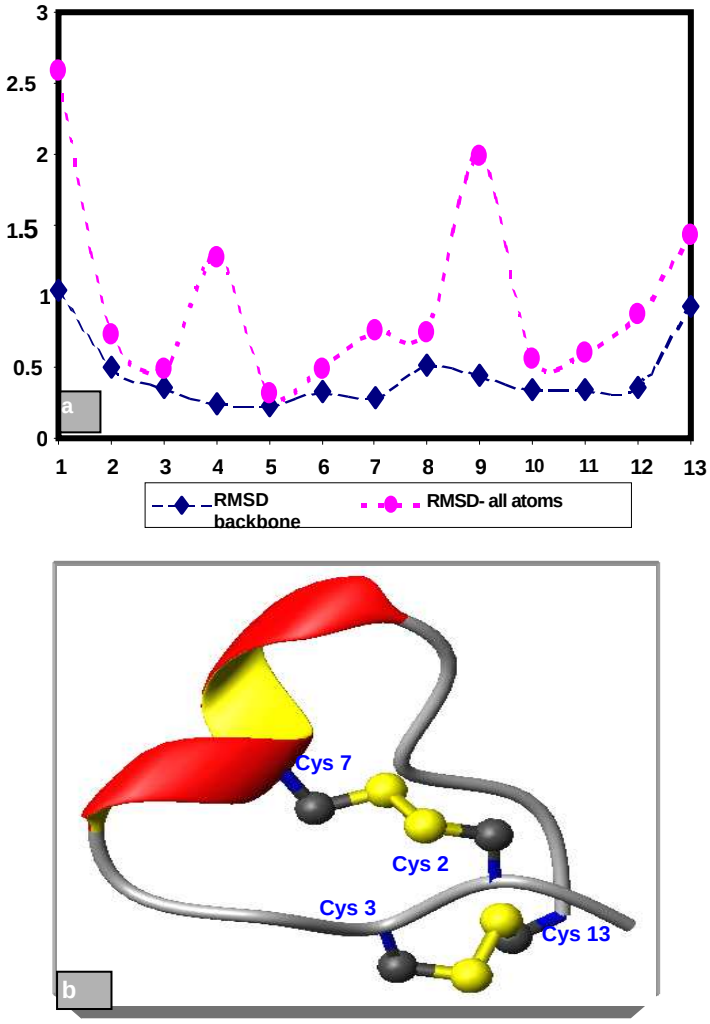

Figure 4 a) RMSD value of all GI aminoacids b) Ribbon (MOLMOL) representation of 3D-structure of ~30 nanomoles α-conotoxin GI, solved by MAS- NMR spectroscopy

The secondary structure is characterized by the presence of a 3_{10} helix between residues Pro^5 to Arg^9 that is stabilized by the Cys^2- Cys^7 and Cys^3 – Cys^{13} disulfide bonds. Conformational constraints provided by both disulphide bonds are important for optimal α-conotoxin GI-binding activity [3]. The RMS deviation (0.47Å for backbone, 1.06Å all non-hydrogen atoms) of all these structure from the average structure reveals a very good quality of the GI solved structure.

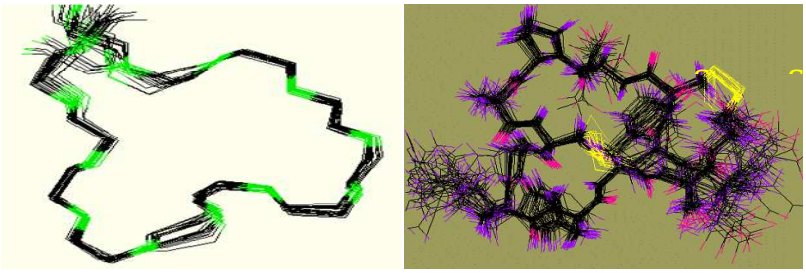

Figure 5 The superposition of the best 32 NMR structures of ~ 30 nanomoles of α-conotoxin GI a) rmsd =0.47 backbone b) rmsd = 1.07 all atoms.

Beside of the crystal structure [4], another three solution structure, one in DMSO [5], and two in water [6,7] of the native isomer GI (2-7; 3-13), as well as the solution structure for two non-native isomers GI (2-13;3-7) and GI(2-3;7-13), have been reported. Gehrmann et. al. solved the tridimensional structure using milimolar quantities of α-Conotoxin GI with a rmsd value of 0.16Å for backbone and 1.27Å for all non-hydrogen atoms [7]. The nano NMR solution structure determined using nanomolar quantities of this conopeptide is in close agreement with the X-Ray structure and previous reported NMR structures (Figure 6).

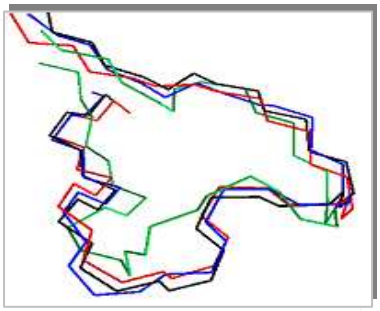

Figure 6. The α-conotoxin GI structures solved by: Green (Pardi '89) Blue (Guddat et. al., X-ray '96); Red (Gehrmann et.al. '98); Black (Matei et. al. 2003)

A very low intensity signal of NH for Arg^9 could be associated as evidence for more than one conformation, and a possibility of stabilizing interactions with other target-residues into physiological environment. The final set of calculated structure shows that side-chain of Arg9 has several possible orientations and is freely to move into the solvent (Figure 5 b). However, the residue Arg9 of α-conotoxin GI has been shown to be responsible for its high selectivity for α,γ agonist site on the electric organ Acetylcholine Receptor [4,8].

The high-resolution structure of nanomolar quantities, determined at t = 0 C°, represents one of possible conformations explored by α- conotoxin GI in the physiological medium, and may be close to that assumed in the presence of target molecules. The nano-NMR methodologies here described can be used for analysis of other conopeptides and in cases where only limited quantities of modified peptides are available.

Structural analysis of ω-conotoxin Vex –B

The Size Exclusion HPLC chromatography technique consisting with a Superdex 30 Column, in NH_4HCO_3 mobile phase mode, was used to separate 57 mg crude venom of *C. vexilum* (Figure 7.a). The HPLC chromatogram suggests a mixture of peptides components in venom. The fraction 6 collected from size exclusion was further separated by semipreparative Reversed Phase HPLC using a Semiprep Vydac 18 Column (Figure 7b). About 23 nanomoles of Vex –B conotoxin was finally collected.

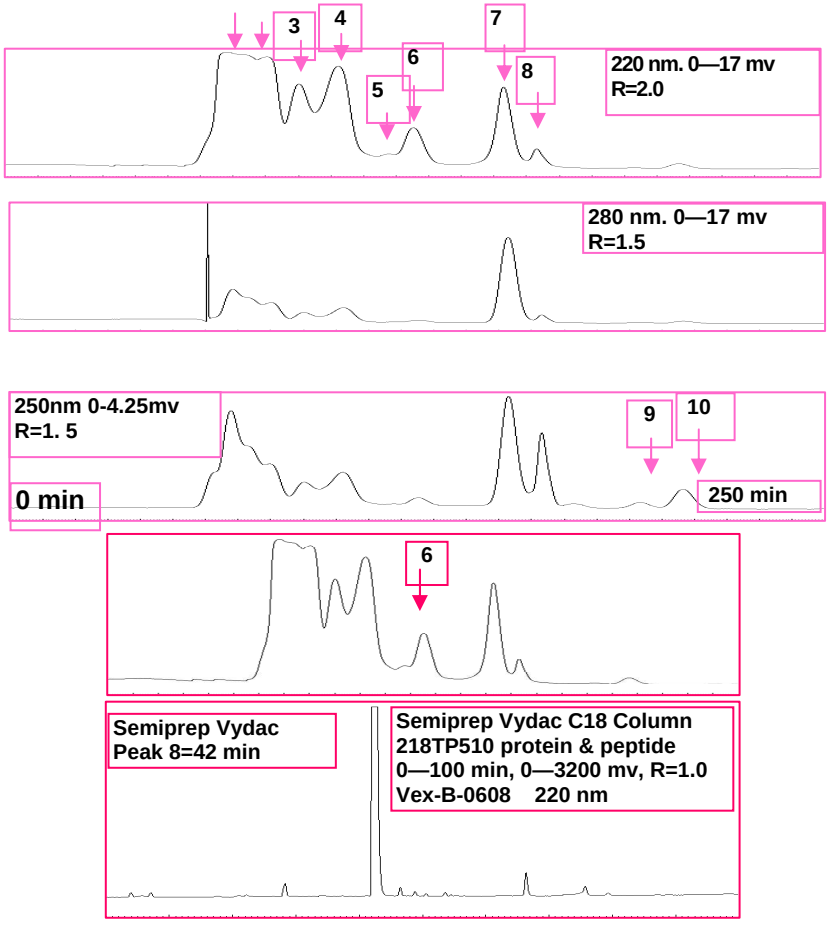

Figure 7a) SE - HPLC cromatogram of the crude venom of *C. vexilum*
b) RP- HPLC of fraction 6 separated by a **Semiprep Vydac C18 Column.**

The molecular weight of Vex-B determined by MALDI-Tof MS Spectrometry is **2926.8623 Da** (Figure 8 a).

The reduction-alkylation reaction was used to break the disulfide bonds. The difference in molecular weight before and after reduction & alkylation from **2926.8623** to **3277.5,** suggests the presence of six Cys within sequence (Figure 8b).

A complete sequence of 28 residues

(ACTOOGGACGNHGHCCHYCNTLTSTCYQ)

of Vex-B peptide was obtained at the end of Edman degradation process on Procise® protein sequencer. The sequence shows clearly the presence of six Cys. The two hydroxyprolines in position 4 and 5 may have significant neuronal protection relevance. A comparative sequence analysis shows that Vex-B belongs to the ω- conotoxins family that blocks Ca^{2+} channel (Table 1)

Table 1

	Sequence	Source
	1 2 3 4	
Vex-b	**ACTOOGGACGNHGH-CC-HYCNTLTSTCYQ**	*C.Vexilum*
GVIA[1]	**CKSOGSSCSOTSYNCC-RSCNHWTKRCY***	*C.geographus*
GVIB[2]	**CKSOGSSCSOTSYNCC-RSCNOYTKRCYG***	*C.geographus*
GVIC[2]	**CKSOGSSCSOTSYNCC-RSCNHWTKRC***	*C.geographus*
TVIA	**CLSOGSSCSOTSYNCC-RSCNOYSRKCY**	*C.tulipa*
SVIA[3]	**CRSSGSOCGVTSI-CCGR-C--YRGKCT***	*C.striatus*
SVIB[3]	**CKLKGQSCRKTSYDCCSGSCGRS-GKC***	*C.striatus*
MVIIA[4]	**CKGKGAKCSRLMYDCCTGSCRS--GKC***	*C.magus*
MVIIB[4]	**CKGKGASCHRTSYDCCTGSCNR--GKC***	*C.magus*
MVIIC[5]	**CKGKGAPCRKTMYDCCSGSCGRR-GKC***	*C.magus*
MVIID[6]	**CQGRGASCRKTMYNCCSGSCNR--GRC***	*C.magus*
CVIA[8]	**CKSTGASCRRTSYDCCTGSCRS--GRC***	*C.catus*
CVIB[8]	**CKGKGASCRKTMYDCCRGSCRS--GRC***	*C.catus*
CVIC[8]	**CKGKGQSCSKLMYDCCTGSCSRR-GRC***	*C.catus*
CVID[8]	**CKSKGAKCSKLMYDCCSGSCSGTVGRC***	*C.catus*
CnVIIA[9]	**CKGKGAOCTRLMYDCCHGSCSSSKGRC***	*C.consors*
TxVII[7]	**CKQADEPCDVFSLDCCTGICLGV---CMW***	*C.textile*

NMR experiments

Samples for NMR studies were prepared using ~ 23 nanomoles of natural peptide in 90% H_2O/ 10%D_2O solution at pH = 3.6. TSP (0.1mM) was used as an internal standard. The NMR experiments were performed using a Varian INOVA 500 spectrometer equipped with 3mm *g*HCN (with 1.7mm inserts) probe. In order to obtain unambiguous resonance assignment the NMR spectra were recorded at four different temperatures (0°C, 10°C, 25°C and 35°C).

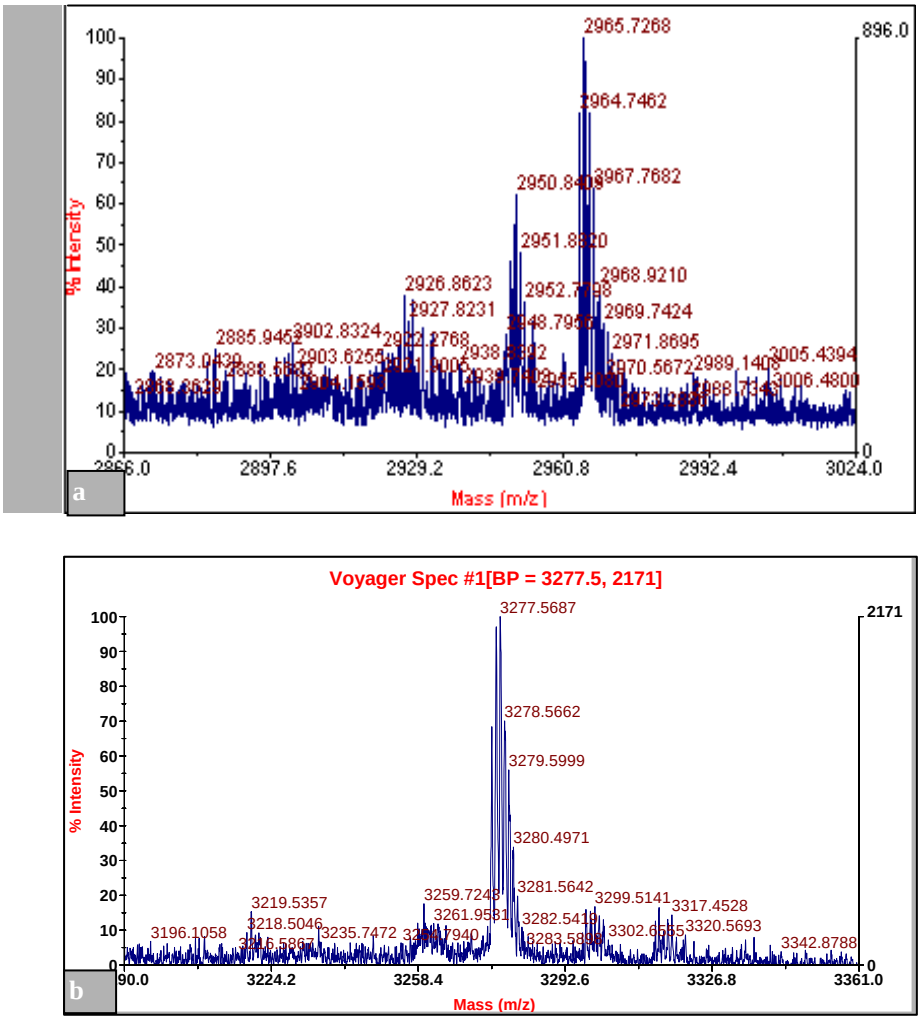

Figure 8 a) MW =2926.8 Da of Vex-b **b)** MW = 3277.5 after reduction & alkylation proved the presence of six Cys within Bru-1 sequence

Proton resonance specific assignment of Vex-B was achieved with the combined use of the ES-TOCSY and watergate-NOESY following the standard biomolecular NMR procedure [2]. The spin system was elucidated using the NH- αH, NH-NH and sidechain regions of ES-TOCSY at 25°C (Figure 9) and corresponding regions of wg-NOESY spectra (Figure 10). Interproton distance restraints used for computation of the structures were derived primarily from the wg-NOESY spectra recorded with a mixing time of 80 ms at 10 °C.

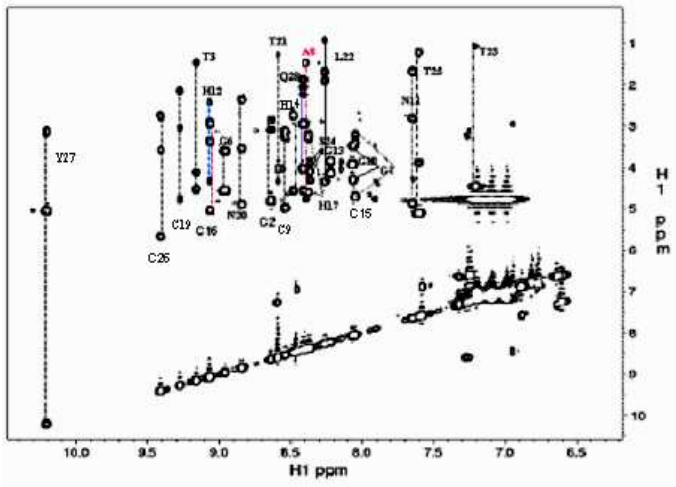

Figure 9. ES-TOCSY spectra of ~23 nanomoles of Vex-B at 25°C

It can be observed that in most spectra, the proton signals show a very little overlap. The change in temperature had a significant effect on the signal intensity, chemical shifts, linewidths, mostly for NOESY experiments. Some of the changes in signal intensity and linewidts may be attributed to the relaxation process. The correlation time associated to overall tumbling motions is much shorter for small size peptides. The global mobility and exchange process are more significant as the temperature is raised. TheC^{13}-HSQC experiment does not provide a good quality of spectra suitable for proton spin system elucidation. The NOEY spectra recorded at 10°C (pH=3.6) were chosen to carry out the most part of sequence specific assignment and to obtain the nOe constraints file required for structural determination of Vex–B. Only in few cases it was necessary to use 2D spectra at 0°C or 25°C, even 35°C to complete the assignment. The lack of NH for two hydroxy-prolines lead to missing sequential i to i+1 cross-peaks, that made the sequence specific assignment more complicated. However, we could not assign some ambiguous cross-correlations that are overlapping in the same region of the spectra. The cross-correlation and chemical shift values of the sidechain of the two hydroxyprolines were better observed in wg-NOESY spectra at 0 °C (Figure 10 b).

The NMRpipe program was used for quantification of NOE volumes and for converting them into interproton distances. The NOE restraints were classified into three categories: strong (1.8-2.7 Å), medium (2.7 -3.5 Å), and weak (3.5-5.0 Å). We were able to assign a total of 232 nOe-constraints from wg-NOESY spectra (92 intraresidue, 54 sequential, 14 short and medium distance and 33 long distance). Structures determinations were carried out using a dynamical simulated annealing (SA) protocol incorporated in XPLOR software. The initial pdb coordinates file of Vex-b that can be read by XPLOR was generated using HYPERCHEM program. The pdb file was used in refine.inp code file to generate a structure file (VEX.psf) specific to the force field of the peptide, using some XPLOR parameter files (covalent bonds, dihedral angles, impropers, etc.). The VEX.psf file was further used to generate

an arbitrary template coordinate file with ideal geometry of the peptide, as a starting file for SA protocol. The final table needed to calculate the structure is NOE constraints file. Once all this files are provided the structures can be generated by the means of sa.inp (XPLOR) code file.

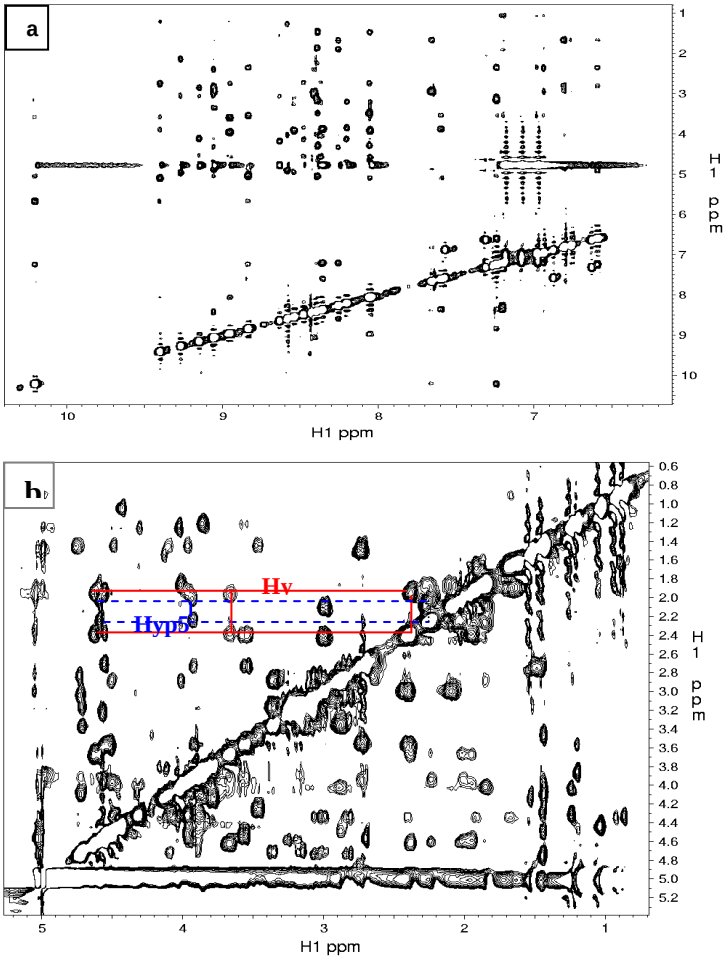

Figure10 a) wg-NOESY spectra of ~23 nanomoles of Vex-b at 10 °C
b) wg-NOESY sidechain of Vex-b at 0 °C

The actual computation of the structures was done in two major steps. The first step involved generation of 125 structures using sa.inp (XPLOR) code file. The second step was refinement of the resulting structures using the refine.inp code file. A total of 34 structures were accepted by accept.inp code file using a 0.3 NOE threshold. The refined structures were analyzed for best fit the NMR constraints and a number of 14 structures were retained based on their lower energy value.

The average structure was calculated by average.inp using file with a RMSD of 1.3 for the backbone and 1.79 for all atoms (Table2).

Table 2

NOE restraints	232
Intraresidue	92
Sequential	54
Medium distance	14
Long distance	33
Energies (kcal mol /1)	
$E_{bond} + E_{angles} + E_{impropers} = 95.6 \pm 5$	
Rmsd (Å) from the av. structure	
all non-h atoms	1.8
backbone	1.3

The structure has a very well defined region near the N-terminal (Cys2 to Gly7) where RMS deviation is much lower to 0.8 Å (Figure 11). RMS deviation for the backbone and all heavy atoms that range from 1.9 to 2.5

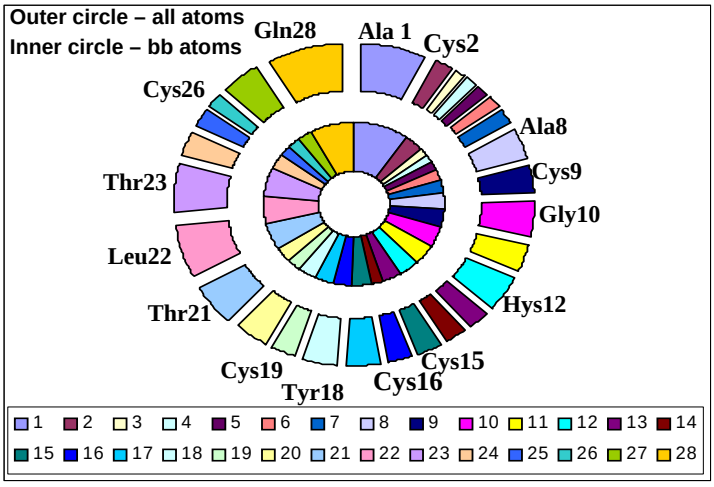

Figure 11. Rmsd value for backbone atoms (inner circle) & all atoms (outer circle). Å within loop region, may be associated with certain degree of conformational flexibility of the peptide.

The superposition over average structure of the best 14 structure is given in Figure 12.a. Figure 12.b. shows the ribbon representation of the minimized average structure of ω -conotoxin Vex-b. The structure of Vex-b is characterized by the presence of two loops stabilized by the presence of three disulfide bonds. Similar two-loop conformational arrangement was observed in most omega conotoxin structures. The structure determined here is close with that of ω -conotoxin MVIIA from *C.magus,* which was found to have significant therapeutics properties. A comparison a backbone atom structure of Vex-b and ω -conotoxin MVIIA is given in Figure 12.c.

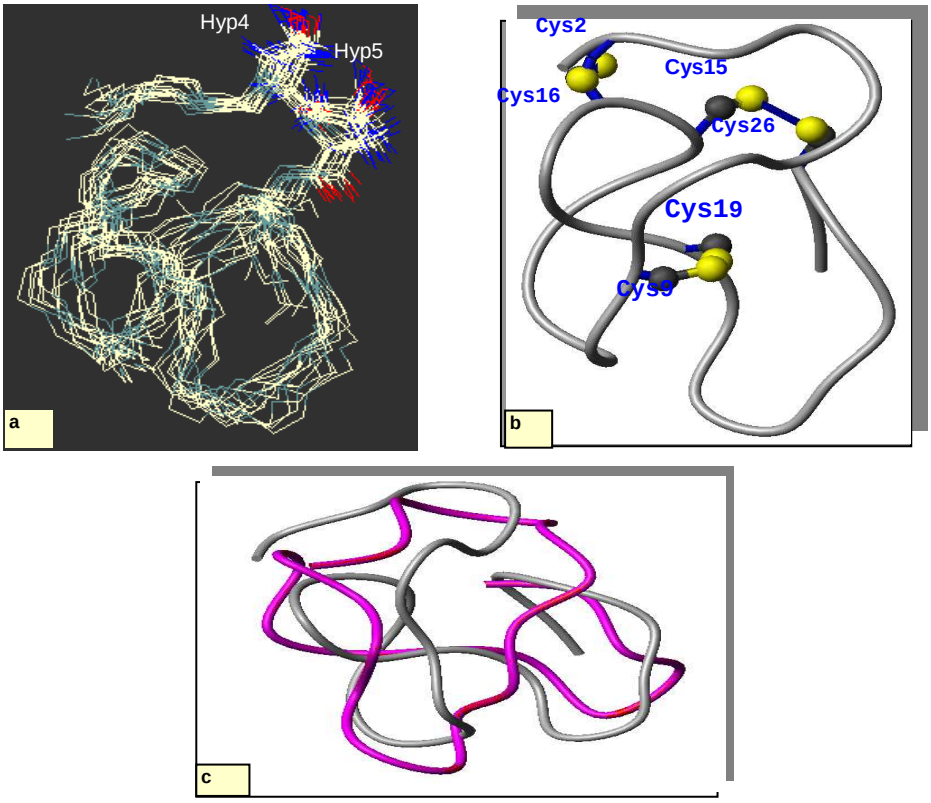

Figure 12 a) Backbone atoms of the best 14 structures of Vex-b superimposed over of the average structure. (rmsd =1.3 backbone; rmsd =1.79 for all atoms) **b)** Ribbon representation of 3D-structure of ω-conotoxin Vex-b **c)** Comparison of the backbone atom between the average structure of Vex-b(grey) and the NMR structure of ω -conotoxin MVIIA (magenta).

Bilogical implication

Cone snails, the marine predators, have some extraordinary features. Their venom contains a hundred or more peptides that target numerous ion channels and receptors in mammals, including several that are involved in diseases.

The α-conotoxins have potent biological activities that correlate well with their binding affinities for *T*orpedo *californica* nAchR [9, 10, 11]. α-Conotoxins GI and MI, isolated from the venoms of *Conus geographus* and *Conus magus*, cause a rapidly lethal muscle paralysis in mice at submicrogram quantities. Selective binding of α-neurotoxins to the nAchR from different animal species is also evident for α- bungarotoxin, a snake postsynaptic neurotoxin purified from *Bungarus multicinctus* venom [12].

At the neuromuscular junction, acetylcholine acts by binding nicotinic AchR. The channel is converted from a closed to open state by the binding of two molecules of Ach to sites located at α- γ and α- δ interfaces. Conotoxin GI and another antagonists compete with Ach for these sites.

The best defined omega-conotoxin are GVIA from *Conus geographus*, omega conotoxins MVIIA, MVIIIV and MVIID from *Conus magus*, omega CNVIIA from *Conus consors* and omega conotoxin CVID from the venom of *Conus catus*.

Ca^{2+} ion channels have been classified pharmacologically and biophysically. The channels are designated L-, T-, N-, P-, Q- and R-type. Each channel has different voltage ranges and rates for activation and inactivation.In mammalian systems, omega GVIA and omega MVIIA are remarkably specific for voltage-gated calcium channels [13]. Since calcium channels present at presynaptic termini, generally omega conotoxins have become widely used tools for blocking synaptic transmission.

Omega conotoxins, MVIIA and CVID are currently in clinical development for chronic pain management (Ziconotide and AM336, respectively). Recent experiments in U.S.A have shown a *synthetic* molecule based on one of the paralyzing ω-conotoxin MVIIA, almost magically blocks acute pain in patients who no longer obtain relief from opiate drugs. These include terminally ill cancer and AIDS patients with chronic pain. The compound called Ziconotide, developed by the biopharmaceutical company Neurex, is 100 to 1000 times more potent than morphine. This conotoxin (also known as **SNX-111**) is undergoing stage III clinical trials in the USA as a treatment for intractible pain.

REFERENCES

1. Gray, W.R., Luque A., Olivera B.M., Barret J., and Cruz L.J., *J. Biol. Chem*.,256, 4734-4740, (1981).
2. Wüthrich, K. NMR of proteins and nucleic acids. (Wiley, New York), (1986).
3. J. D. Ashcom and Bradley G. Stiles, *Biochem. J*., *328,* 245-250, (1997).
4. L.W. Guddat, J. A. Martin, L. Shan, A.B. Edmundson, and W.R. Gray, *Biochemistry*, 35, 11329-11335, (1996).
5. Kobayashi Y., Ohkubo T., Kyogoku Y., Nishiuchi Y., Sakakibara S., Braun W. & Go. N., *Biochemistry*, 28 (11), 4853-4860, (1989).
6. Pradi. A., Galdes A., Florance J., Maniconte D., 5494-501, 28 (1989).
7. John Gerhrmann, Paul F. Alewood and David J. Craik, , *J. Mol. Biol*., 278, 401-415, (1998).
8. R. M. Hann, O. R. Pagan, L. M. Gregory, T. Jacome, V. A.Eterovic, *Biochemistry*, 36, 9051-9056, (1997).
9. Zafaralla, G. C., Romila, C., Gray, W. R., Karlstrom, R., Olivera, B. M. and Cruz, L. J., Biochemistry *27*, 7102-7105, (1988).
10. Hann, R. M., Pagan, O. R. and Enterovic, V. A., Biochemistry *33*, 14058-14063, (1994).
11. Groebe, D. R., Dumm, J. M., Levitan, E. S. and Abramson, S. N., Mol. Pharmacol. *48*, 105-111, (1995)
12. Barchan, D., Ovadia, M., Kochva, E. and Fuchs, S., Biochemistry *34*,9172-9176, (1995).
13. Olivera, B. M.; Cruz, L. J.; Desantos, V.; Lecheminant, G. W.; Griffin, D.; Zeikus, R.; McIntosh, J. M.; Galyean, R.; Varga, J.; Gray, W. R.; Rivier, J. *Biochemistry*, *26*, 2086-2090, (1987).

STUDIA UNIVERSITATIS BABEŞ-BOLYAI, PHYSICA, XLIX, 2, 2004

FT-IR SPECTROSCOPY AND X-RAY DIFFRACTION STUDIES OF INCLUSION COMPLEXES OF β- AND γ- CYCLODEXTRINS WITH TENOXICAM

I. BRATU[1], A. HERNANZ[2], MINO R. CAIRA[3], J.M. GAVIRA[2] and GH. BORA[4]

[1]National Institute for Research and Development of Isotopic and Molecular Technologies, Cluj-Napoca, R-400293, ROMANIA, ibratu@s3.itim-cj.ro
[2]Universidad Nacional de Educación a Distancia, Depto. de CC y TT Físicoquímicas, Madrid, E-28040, SPAIN
[3]University of Cape Town, Dept. of Chemistry, Private Bag, Rondebosch, 7701, South Africa
[4]"Terapia", 126 Fabricii st., R-3400 Cluj-Napoca, ROMANIA

ABSTRACT. Tenoxicam and its inclusion complexes with β- and γ-cyclodextrin were prepared by co precipitation and freeze-drying methods and investigated in solid state by X-ray diffraction and FT IR spectroscopy. The polymorphic III form used in the present was certified by the mentioned methods. The inclusion complex structure, the functional groups involved and the possible mechanisms of inclusion were proposed.

Introduction

Tenoxicam (*TEN*) is a NSAID of the second-generation oxicam family with anti inflammatory and analgesic actions, being used in the treatment of chronic rheumatic disorder (arthritis, osteoarthritis), gout and ankylosing spondylitis. The replacement of the benzo ring of the Piroxicam with the thieno residue in the case of *TEN* does not produce a strong influence on the lipophilicity of that molecule. However, the attractive electronic effects of the sulphur atom can change the electronic properties of the neighbourhood with possible pharmacological consequences. As for other oxicams, *TEN* causes gastrointestinal ulceration and bleeding. Due to this unpleasant effect, a possible percutaneous delivery is desirable. Cyclodextrins (CDs), see Fig. 1, structurally related cyclic non-reducing oligosaccharides (consisting of six, seven or eight glucose units, respectively α-CD, β-CD and γ-CD) and their derivatives are typical host molecules forming inclusion complexes (*ICs*) in both solid and solution states. Inclusion complexes of *TEN* with γ-CD were studied in order to improve its aqueous solubility and to decrease its adverse side effects [1]. In the present work only two CDs were used, namely β- and γ-CD. It is of interest to establish the way in which *TEN* as guest molecule, see Fig.2, enters the CD torus.

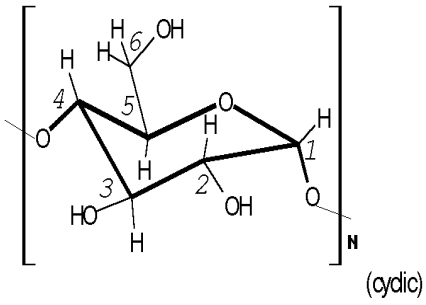

Fig. 1. β- and γ-CD molecules with the atom numbering (N=7 and 8, respectively).

The purpose of this work was to determine if *ICs* were obtained and which part (*i.e.* functional groups) of the drug molecule are involved in the inclusion process.

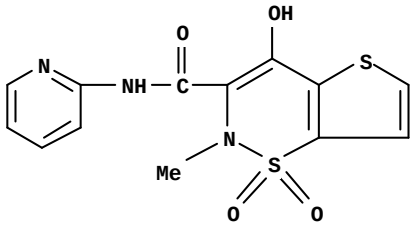

Fig. 2. Tenoxicam molecule

Materials and methods

IC preparation

Various methods for obtaining *ICs* can be used: physical mixing (*pm*), co-grinding, co-precipitation (*co*), freeze drying (*fd*) and kneading (*kn*) [2]. In the present work only two methods were used, *co* and *fd,* as they were considered the most efficient ones. An *IC* in the 1:1 molar ratio was prepared by co-precipitation from an aqueous solution of β-CD (heated to 50°C) or γ-CD (at room temperature), respectively, to which the drug was added. In order to increase the drug solubility NH_4OH was added to this aqueous solution until a *pH* = 9 was obtained. The homogeneous solution was stirred at room temperature until a co-precipitate product was obtained, isolated and then dried at 38°C. In order to obtain *fd* products, from the same mother solution stirred for one hour, an aliquot was taken and stored in a freezer and thereafter, freeze-dried overnight. Physical mixtures of *TEN* and β-CD or γ-CD were obtained by gently mixing the corresponding solids in an agate mortar.

XRD examination of Cyclodextrin / TEN preparations

The samples were used as provided and were packed in standard Al holders for X-ray powder diffraction analysis. For controls, two physical mixtures (β-CD / *TEN*, γ-CD / *TEN*) were prepared in 1:1 molar ratio by gentle mixing until the samples were homogenous. Powder patterns were recorded on a Philips PW1050/80 vertical goniometer using CuKα-radiation (λ = 1.5418 Å). Step scans (0.1º 2θ) were performed with 2 s counts per step over the range 2θ = 6-40º. Only the portions of the traces for the range 6-30º were compared.

FT IR spectroscopy

FT IR spectra were obtained using the KBr pellet technique; they were collected in the 4000 to 400 cm^{-1} spectral region with a Bomem DA3 FT IR spectrometer, under vacuum with a resolution of 2 cm^{-1}. Good S/N ratios were obtained by co-adding 250 interferograms.

Results and Discussion

XRD

In general, patterns for the co-precipitated and freeze-dried samples were compared with those of the corresponding physical mixtures, as well as with standard reference patterns generated for series of known, isostructural β-CD and γ-CD complexes. In the case of matching between sample pattern and a reference pattern,

one can make a definitive statement as regards complex formation. If, however, the sample pattern does not match a reference pattern [3-5], this does not exclude the possibility of complex formation as the phase examined may represent a new series, as yet undocumented. Table 1 below lists the sample trace label, sample description and the conclusion drawn from the various comparisons of X-ray patterns described above.

Table 1.

X-ray diffraction analysis results

Sample	System investigated	Comments
S5	TEN + β-CD (1:1), *co*	Very convincing match with SM2, indicating no complexation or in a very small extent.
S6	TEN + β-CD (1:1), *fd*	Relative to S5, some crystallinity is still retained, but trace is essentially an 'amorphous version' of trace S5, with coincidence of main peaks.
S9	TEN + γ-CD (1:1), *co*	Partially amorphous. Poor match with SM4, which could indicate some complex formation. Pattern does not match reference pattern † but sample could contain complex with new structure.
S10	TEN + γ-CD (1:1), *fd*	Good match with S9, but the sample is considerably more amorphous.
SM2	TEN + β-CD (1:1), *pm*	-
SM4	TEN + γ-CD (1:1), *pm*	-

This refers to the standard reference pattern for the tetragonal phase ($P42_12$) that is the common one for γ-CD inclusion complexes.

FT IR spectra

Infrared spectra of *IC*s and *pm* are quite different: several changes were observed both in the 4000 to 2000 cm^{-1}, see Fig. 3 and in the 2000 to 600 cm^{-1} spectral regions, respectively, see Figs 4 and 5.

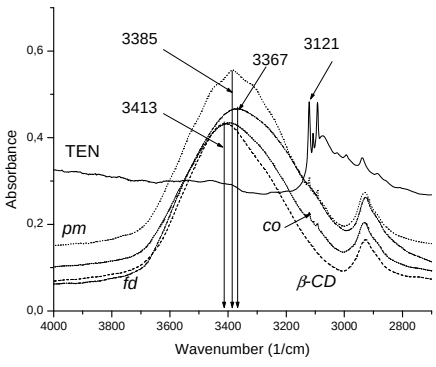

Fig. 3a. FT IR spectra (4000-2600 cm^{-1}) of TEN (_____), *pm* (------), *co* (.....), *fd* (-.-.) and β-CD (-..-..)

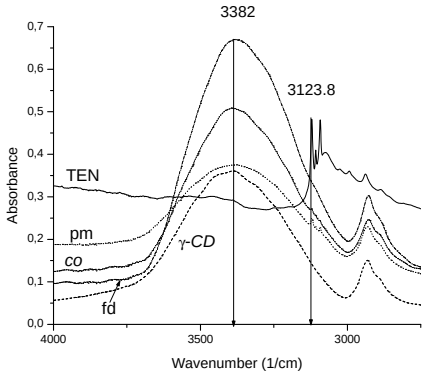

Fig. 3b. FT IR spectra (4000-2600 cm^{-1}) of TEN (_____), *pm* (------), *co* (.....), *fd* (-.-.) and γ-CD (-..-..)

There is a broad band between 3100 and 2700 cm^{-1}, due to the –OH and NH stretching bands, respectively. These bands are characteristic for each polymorphic form of TEN. It is known that, depending on the solvent used for the recrystallization, one can obtain different polymorphic forms. By the inspection of the FT IR spectra of pure TEN and comparing the literature data [5], one can establish the polymorphic form used in the present work, namely form III, with a melting range of 217-220ºC, obtained from acetone [6].

Comparative analysis of the FT IR spectra for different ICs of β-CD and γ-CD with TEN

4000-2000 cm^{-1}

The O-H stretching band (~3400 cm^{-1}) and N-H stretching band (~3073 cm^{-1}) of the secondary amine of the *TEN* exhibit a broadening and an increase in intensity in the *IC* spectrum as compared to the *pm* spectrum. The O-H stretching maximum appears at 3413 cm^{-1} (*β*-CD), 3385 cm^{-1} (*pm*), 3400 cm^{-1} (*co*) and 3367cm^{-1} (*fd*) for *TEN*/*β*-CD. The low N-H stretching wavenumber is probably due to the inter- and intramolecular hydrogen bonds involving nitrogen and oxygen atoms of the secondary amine group [7]. The narrow bands appearing between 3092 and 3121 cm^{-1} are probably due to the aromatic character. They are clearly identified in the *pm* and *co* spectra but it is quite difficult to identify them in the *fd* spectrum, a very broad envelope being observed in this case.

A quite different situation was observed in the case of *γ*-CD inclusion complexes: there are small differences in the spectra in this spectral region. The O-H stretching band is located at 3382 cm^{-1}, independent of the *IC*s preparation method, so it is difficult to explain the *IC* appearance mainly on the basis of expulsion of water molecules from the cavity [8], a process quite evident in the case of *β*-CD *IC*s where the position of this maximum is modified. The N-H stretching band is easily identified for the *pm* and *co IC*s but not in the case of *fd IC* where the fine structure is smeared out due to the amorphisation.

2000-600 cm^{-1}

Several differences appear comparing the spectra of pure TEN or the *pm* and those corresponding to different *IC*s of *β*-CD and *γ*-CD: a broadening of the carbonyl-stretching band (1639 cm^{-1}) is observed in the *IC* spectra, see Figs 4 and 5.

In the FT IR spectrum of TEN the sharp bands at 1639 cm^{-1} and at 1599.7 cm^{-1} are assigned [9] to the carbonyl C=O and C=N stretching vibrations of the -CO-NH- secondary amide group, respectively. Once again, by comparing the bands present in this spectral region with the literature data [3], one can deduce that the polymorphic form used in the present work is form III. The bands at ~ 1600 and 1495 cm^{-1} are also due to the aromatic ring. The ν(C=O) and ν(C=N) bands are shifted to higher frequencies in the *TEN* /*β*-CD spectrum of the *co IC* at 1644.3 and 1605 cm^{-1}, respectively, whereas for the *fd* preparation, these bands are broadened but unshifted in wavenumber.

The CNH deformation for the *trans* configuration, located at 1558 cm^{-1} is perfectly detectable, although other authors [9] have not detected this band. They used slightly different conditions (60ºC and *pH* = 12) for preparing inclusion complexes.

The band at 1540 cm^{-1} can be due to the δ(NH) mode of the amide. A new broad band appears at 1520 cm^{-1} in the *IC* spectrum of *fd* type. In the *TEN*, *pm* and *co* spectra there is a shoulder at 1529.3 cm^{-1}. The observed broadening and increase of intensity in the *fd* spectrum may be due to a hydrogen bonding effect. The band of *TEN* located at 1450 cm^{-1} is assigned to the $\nu_{asymm}CH_3$ and $\nu_{arom}C{=}C$.

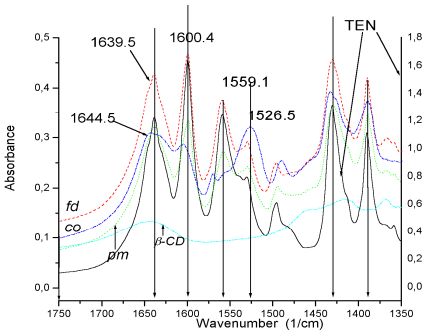

Fig. 4a. FT IR spectra (1750-600 cm^{-1}) of TEN (_____), *pm* (------), *co* (.....), *fd* (-.-.) and β-CD (-..-..). The absorbance scale is different (right vertical axis) for TEN spectrum.

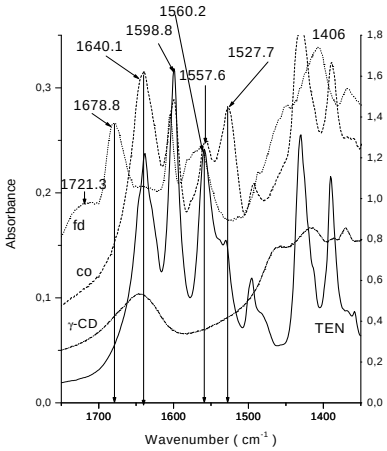

Fig. 4b. FT IR spectra (1750-1350 cm^{-1}) of TEN (_____), *pm* (------), *co* (.....), *fd* (-.-.) and γ-CD (-..-..). The absorbance scale is different (right vertical axis) for TEN spectrum.

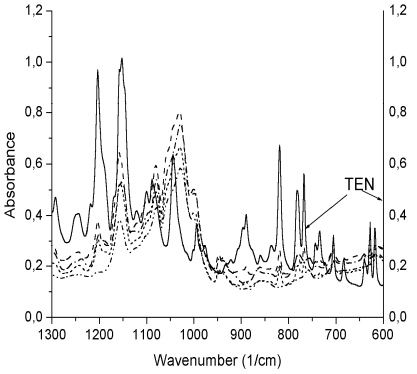

Fig. 5a. FT IR spectra (1300-600 cm^{-1}) of TEN (_____), *pm* (------), and *IC, co* (.....), *fd* (-.-.) and of β-CD (-..-..).

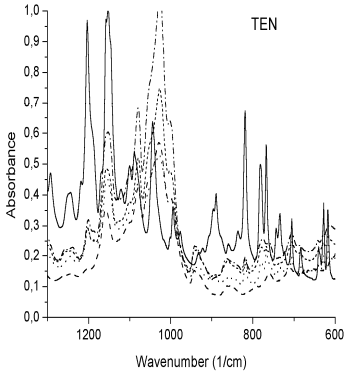

Fig. 5b. FT IR spectra (1300-600 cm^{-1}) of TEN (_____), *pm* (------), and *IC, co* (.....), *fd* (-.-.) and of γ-CD (-..-..).

At 1360 cm^{-1} one can identify the $\nu_{symm}CH_3$, whereas the band at 1150-1180 cm^{-1} is assigned to the $\nu_{symm}SO_2$-N- vibration (sulfonamide which absorbs at 1239 and 1152 cm^{-1}, see also [3]). The O-H deformation band at 1044 cm^{-1} in the *TEN* spectrum [3, 5], is broadened also in the *IC* spectra, the effect being more evident in the *co* spectrum. Lastly, the band at 730-770 cm^{-1} corresponds to the *o*-di-substituted phenyl. The broadening of this band and of the one observed in the N-H stretching region can be due to the formation of stable hydrogen bonds between *TEN* and the CDs.

One notes that the most important differences between the FT IR spectra of the *IC*s obtained for *TEN* / β-CD and *TEN* / γ-CD were observed in the 1800 to 1500 cm^{-1} spectral region.

TEN / β-CD *system*

In the spectrum of pure *TEN* the characteristic bands centred at 1639 cm^{-1}, 1599 and 1559 cm^{-1} appear. They are shifted to 1644 and 1606 cm^{-1} respectively for the *IC* obtained by the *co* procedure. One observes an intensity inversion in this *IC* spectrum also, see Fig. 4a, explained by rupture of the hydrogen bonds and an intensity increase of the 1644 cm^{-1} band. The bands become broad and asymmetric, a possible explanation being the amorphisation of the system. For the rest of the *IC*s, the spectra are quite similar, so it is difficult to identify the complex formation by using only FT IR spectra. Probably only a small fraction of the starting components produced the *IC*.

TEN / γ-CD *system*

The bands centred at 1598.8 and 1638 cm^{-1} are shifted to 1603 cm^{-1} (*fd*) and 1640 cm^{-1} (*co*); for the *fd* system the band at approx. 1600 cm^{-1} disappears, being shifted to 1678 cm^{-1}. One observes also a small intensity band (shoulder), centred at 1721.3 cm^{-1}. This effect could be attributed to the breakdown of the intermolecular hydrogen bonds of the crystal associated with the inclusion of the drug monomer into the hydrophobic cavity of the carrier [9]. These differences that appear in the corresponding FT IR spectra demonstrate the new structure, viz. the inclusion complex.

The general aspect of the *fd* spectra is characterized by the presence of broadened bands as compared to the corresponding ones for *TEN* or *pm* spectra. This fact reflects the amorphous state of the *IC* systems. Both *co* and *fd* spectra present differences as compared to the *pm* spectrum showing that these methods are suitable for the *IC* preparation.

Conclusions

The use of a single polymorphic form of *TEN* in the present work was clearly established by X-ray diffraction and FT IR spectroscopy.

Based on XRD and FT IR data one can estimate that an *IC* is evidently formed if *fd* and *co* methods are used, especially with γ-CD as host; the results are not clearly evident in the case of β-CD although FT IR spectra showed some frequency shifts indicating that a new structure is formed, though with low efficiency. Probably, the most important mechanism in the formation of the *ICs* is estimated to be the rupture of the hydrogen bonds resulting upon insertion of the *TEN* molecules inside the CD cavity, the carbonyl group playing an important role in the inclusion process.

The expulsion processes of the intracavity water molecules [8] must be taken into account. Other procedures are necessary to establish the nature of the forces [11] involved in the inclusion process.

Acknowledgements One of us (I.B.) is grateful to the NATO Science Committee for a *Dc* type grant supporting his scientific stay at UNED, Madrid.

Thanks are due to Dr. R.G. Cantera from the Galenic Center, University of Navarra, Pamplona, Spain for his kindness in offering access to its FT IR data for the polymorphic forms of tenoxicam.

REFERENCES

[1] Z. Aigner, A. Kezsmarki, M. Kata, Cs. Novak, I. Erös, *J. Incl. Phenom. Macrocyclic Chem*., 42 (2002) 227-233.

[2] S. Şenel, Ö. Cacoğlu, M. Şumnu, D. Duchêne, A.A. Hincal, *J. of Inclusion Phenom. and Molec. Recogn.*, 14 (1992) 171-179.

[3] R. G. Cantera, M. G. Leza, C.M. Bachiller, *J. Pharm. Sci*., 91(10)(2002) 2240-2251.

[4] M. R. Caira, L. R. Nassimbeni, M. Timme, *J. Pharm. Sci.*, 84 (1995) 884-888.

[5] R. G. Cantera, *PhD Thesis*, University of Navarra, 1995.

[6] M. Eman Samy, *Alexandria J. Pharm. Sci*., 15(1) (2001) 1-7.

[7] M. Demertzis, S.K. Hadjikakou, D.K. Demertzi, A. Koutsodimou, M. Kubicki, *Helv. Chim. Acta*, 83 (2000) 2787-2801.

[8] J.M. Gavira, A. Hernanz, I. Bratu, *Vibr. Spectroscopy,* 32, Issue 2 (2003), pp. 137-146.

[9] E. Larrucea, A. Arellano, S. Santoyo, P. Ygartua, *Drug. Dev. Ind. Pharm*., 27 (2001) 251-260.

[10] N. Goyenechea, M. Sanchez, I. Velaz, C. Martín, C. Martinez-Ohariz, A. Zornoza, *J. Incl. Phenom. Macrocyclic. Chem.*, 44 (2002) 283-287.

[11] Lei Liu, Qing-Xiang Guo, *Journal of Inclusion Phenom. and Macrocyclic Chem*. 42, (2002) 1-14.

STUDIA UNIVERSITATIS BABEŞ-BOLYAI, PHYSICA, XLIX, 2, 2004

THE ATOMIC MOBILITY IN PROTEIN MAIN CHAINS AND THE RELATIONSHIP TO THERMODYNAMICS OF THE PROTEIN-LIGAND COMPLEX

V.V. MORARIU[1]

[1]*National Institute for Research and Development of Isotopic and Molecular Technologies, Cluj-Napoca, R-400293, ROMANIA, vvm@L40.itim-cj.ro*

ABSTRACT. The series of the atomic mobility in the protein main chains of HIV-1 protease was characterized by the long-range correlation exponent resulting from the slope of the double-log plot of the FFT of the series. We have characterized the protease-substrate complex and protease-drug inhibitors complexes respectively and compared to the various thermodynamics free energy contributions to the overall binding free energy. We found that the weaker the electrostatic contributions to the interaction energy the stronger the correlation of the atomic mobility in the protein main chain and vice versa, the stronger the nonelectrostatic forces the stronger the correlation. This suggests that the correlation property of the crystallographic temperature factor of the protein main chains can be used to predict some of the energies of interaction contributing to the binding free energy.

Introduction

The basic information regarding the structure and dynamics of proteins are the atomic coordinates and the temperature factor (Tf) respectively, which are stored in the Protein Data Bank (PDB). The crystallographic temperature factor, Tf, also known as factor B or Debye-Waller factor, represents a measure of the atomic vibration amplitude. This is also commonly referred to as atomic mobility. A standing problem in protein science is the relationship between structure, dynamics and function. This goal "…has not yet been reached in any protein although the present knowledge in simple proteins such as myoglobin gives some hope that the end is near in this case" [1].

The present work is part of a project on the relationship between structure, dynamics and function. The central point of investigation is the atomic mobility. There is no simple relationship between atomic mobility and function [2-3]. The particular question in this work is whether the correlation properties of the atomic mobility can be related to physical characteristics such as the free energy of the system.

The object of investigation was the human immunodeficiency virus type 1 (HIV-1) protease in the presence of inhibitors currently used as drugs for the treatment against HIV. The components of the free energy of binding of the drugs to the HIV-1 proteinase were reported in the literature [4] so it was possible to investigate in details whether they are related to the correlation properties of the atomic mobility of the corresponding cases. The intuition tells us that there should be some relationships although the details are not at all clear and the literature is silent on this matter.

Our feeling is that the temperature factor was not much exploited despite of the fact that it represents basic dynamic information about proteins, included in PDB. Contrary to the structural characteristics (the atomic coordinates) the temperature

factor is quite sensitive, mainly to ligands and to some extent to mutations. Therefore it might offer the advantage of being used asa predictive characteristics for the protein properties and function.

Previous investigations on the correlation of the atomic mobility in the main chains revealed long–range correlation characteristics [2]. Also it should be reminded that protein structure could be described as fractal [5].

Materials and methods

I selected the human immunodeficiency virus type 1 (HIV-1) protease in combination with the natural substrate and five drugs currently used in USA for the treatment of the HIV disease. The crystal structure and temperature factor of these protease-ligand complexes are available in PDB. The selected cases were included in Table 1.

Table 1

HIV-1 protease complex with various ligands*

No	Ligand	Protein Data Bank code
1	Substrate	7hvp
2	Ritonavir	1hxw
3	Saquinavir	1hxb
4	Amprenavir	1hpv
5	Indinavir	1hsg
6	Nelfinavir	1ohr

- The ligands represent inhibitors approved by Food and Drug Administration (USA) for used as drugs against the HIV disease.

The temperature factor T_f data for each case was downloaded and the relevant data were extracted for the main chain atoms. The series of data was represented by the function T_f=f (atom) where the atoms were numbered as 1,2,3…. The resulting series was subjected to Fast Fourier Transform and the spectrum was represented as a double log plot. The slope of the linear fitting was the scaling exponent β. The spectrum was, therefore, described by a power law $P=1/f^{\beta}$ where f is the frequency. The object of our analysis was the scaling exponent β in conjunction to the free energy characteristics of the protein-ligand complex.

The binding free energy of the protein-drug complex is described according to the Molecular Mechanics/Poisson-Boltzmann Solvation Area method [4] as:

$$\Delta G_{MM} + \Delta G_{sol}^{C} - \Delta G_{sol}^{L} - \Delta G_{sol}^{P} - T\Delta S$$

where ΔG_b is the binding free energies in water, ΔG_{MM} is the interaction energy between the ligand and the protein, $\Delta G_{sol}^{L}, \Delta G_{sol}^{P}$ and ΔG_{sol}^{C} are solvation free energies for the ligand, protein, and complex respectively, and -TΔS is the conformational entropy contribution to the binding. It is assumed that the entropies are similar in magnitude for the inhibitors and the substrate [4]. ΔG_{MM} is calculated from MM interaction energies:

$$\Delta G_{MM} = \Delta G_{\text{int}}^{ele} + \Delta G_{\text{int}}^{vdw}$$

where $\Delta G_{\text{int}}^{ele}$ and $\Delta G_{\text{int}}^{vdw}$ are electrostatic and van der Waals interaction energies between ligand and receptor.

The solvation energy, ΔG_{sol} is divided into two parts, the electrostatic contributions, ΔG_{sol}^{ele}, and all other contributions, $\Delta G_{sol}^{nonpolar}$:

$$\Delta G_{sol} = \Delta G_{sol}^{ele} + \Delta G_{sol}^{nonpolar}$$

We looked for relationships between ΔG_b and all other free energy individual contributions *versus* the scaling exponents β.

Results

All inhibitors bind more tightly than the substrate according to the ΔG_b data (see ref.4). However we found no simple relationship between the binding energy and the scaling exponent β. On the other hand we can see in the figures below that various relationships exist when some components of the free energy are considered. The total electrostatic contribution, $\Delta G_{\text{int}}^{ele} + \Delta G_{sol}^{ele}$ which is $\Delta G_{\text{int}+sol}^{ele}$, is related in an exponential fashion to β. This can read as follows: The weaker the electrostatic interaction energies the stronger the correlation. (More positive values of ΔG mean weaker interaction energies). On the other hand an exponential relationship binds the nonpolar and van der Waals interaction energies and β. One can read: The stronger the nonelectrostatic contributions the stronger the correlation. The exponential relationships illustrated in fig.1-3 are:

$\Delta G_{\text{int}+sol}^{ele} = 44.32 + 2.33E - 7e^{\beta/0.105}$;

$-\Delta G^{nonpol} = 5.013 + 0.0057e^{\beta/0.33}$

and $-\Delta G^{vdw} = 61.96 + 8E - 5e^{\beta/0.156}$.

No clear relationships were found when considered separately the components $\Delta G_{\text{int}}^{ele}$ and ΔG_{sol}^{ele} in respect to β. The only term, which does not obey to a simple exponentatial relationship, is for the HIV-1 protease –Amprenavir complex. This might possibly represent errors or the imprecision of the calculation of these terms. It should be needed more data for analysis in order to conclude that the binding free energy of the protein+drug complex is directly related to the correlation exponent β. This is a worthy effort as the consequence would be very important: the correlation of the atomic mobility is related to the binding energy between the protein and ligand.

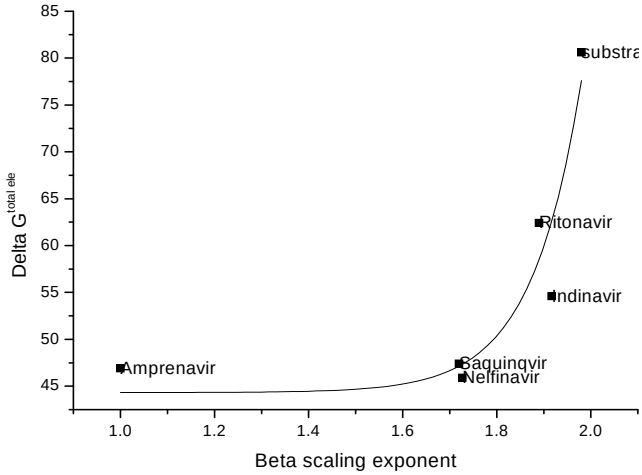

Fig.1. The total electrostatic free energy contributing to the binding free energy in the HIV-1 proteinase-inhibitor complex and its influence on β scaling exponent of the main chain atomic mobility ($\Delta G^{totalele} = \Delta G^{ele}_{\text{int}+sol}$).

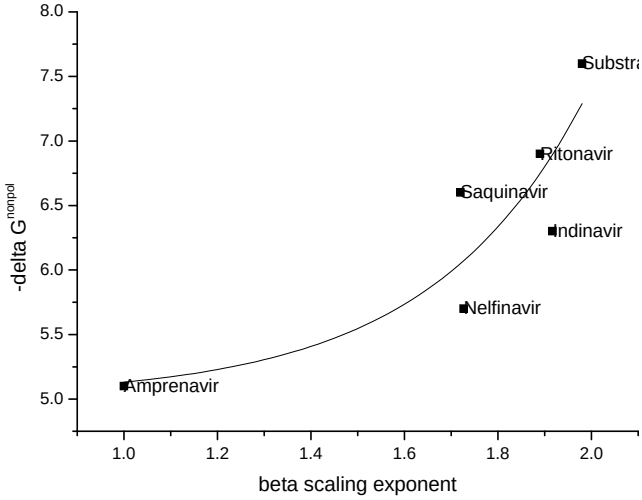

Fig. 2. The influence of the nonopolar solvation free energy for the binding of the drug to protein on β scaling exponent of the temperature factor.

Discussion

Two categories of forces are opposite in respect to the correlation of the atomic mobility. Electrostatic forces “destabilize” the atomic mobility and consequently they fluctuate more widely (weaker correlation). On the contrary, nonelectrostatic forces “stabilize” the atomic mobility and they fluctuate less (stronger correlation). The quantitative summation of these forces has as a result the apparent lack of coherence between ΔG_b and β although this seems to supported by a single case (HIV-1 protease

–Amprenavir complex). The present analysis is limited to the FDA aproved drugs where Molecular Mechanics/Poisson-Boltzmann Solvation Area (MM/PBSA) method was apllied and therefore the binding free energy is available [3].

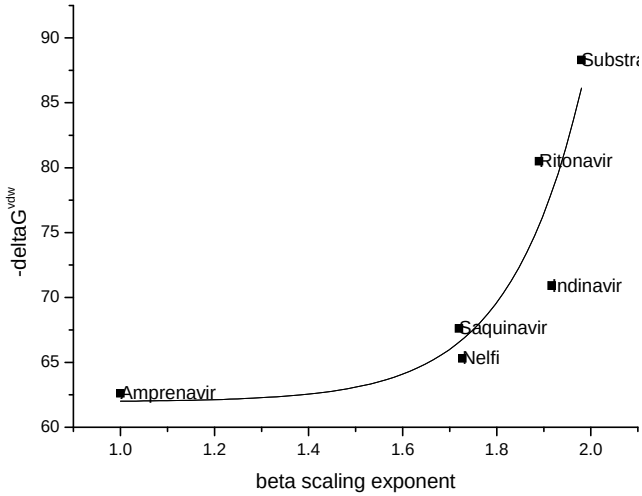

Fig. 3. The van der Waals interaction energies between the ligand and the receptor (HIV-1 proteinase) and its influence on the scaling exponent of the atomic mobility.

Finally it should be pointed out that a protein is a three-dimensional structure and not a simple one-dimensional system as apparently considered during calculations. The series of data consisting of the main chain atomic mobility reflect all the side chain and side atoms of the primary structure as well as all other interactions which generate the protein conformation *i.e.* the 3D structure.

Conclusions

The correlation property of the atomic mobility in protein main chains is a sensitive parameter to some components of the free energy of interaction between the protein and inhibitor. Stronger correlation of the atomic mobility is associated to stronger nonelectrostatic forces and weaker electrostatic forces. Consequently the atomic mobility of the protein main chains can have a relative predictive value about the interaction energies involved in the protein-ligand interaction.

Acknowledgements I wish to acknowledge useful discussions with professor M. Crisan.

REFERENCES

[1] H. Frauenfelder, B.H. McMahon, *BioSystems* 62 (2001) 3-8
[2] V.V.Morariu, A. Coza, *Physica A.*, 320 (2003) 461-474.
[3] T.Graycar, M. Knapp, G,Gashaw, J. Dauberman, R. Bott, *J.Mol.Biol.* 292 (1999) 97-109
[4] Wei Wang, P.A.Kollman, *Proc.Natl.Acad.Sci.USA* 98 (2001) 14937-14942
[5] Dewey TG *Fractals in molecular biophysics*, (1997) Oxford University Press, Oxford, New York

STUDIA UNIVERSITATIS BABEŞ-BOLYAI, PHYSICA, XLIX, 2, 2004

EPR AND HF-EPR OF METALLIC CLUSTERS INCORPORATED IN SOME SUPRAMOLECULAR SYSTEMS

O. COZAR[1], L. DAVID[1], M. RUSU[2], C. CRĂCIUN[1], V. CHIŞ[1]

[1]Babes-Bolyai University, Faculty of Physics, Cluj-Napoca, Romania, cozar@phys.ubbcluj.ro
[2]Babes-Bolyai University, Faculty of Chemistry,Cluj-Napoca, Romania

ABSTRACT. The obtained results about the electronic structure, metal-ligand interaction, local symmetry changes as solvent effects, molecular association processes and the appearance of some dimeric or polymeric species in some supramolecular systems are reported. EPR spectra of Cu(II)-complexes with antiimflammatory and cardiovascular drugs (indomethacin, ibuprofen, piroxicam, dihidrazinophtalazine) exhibit typical absorbtions of randomly oriented triplet state (S=1) species (dimers) with small rhombical distorted axial symmetry. Trinuclear metallic clusters encapsulated in some polyoxometalates (supramolecular blocks of metal oxide) with applications in medicine and catalysis were evidenced too. The local symmetry, type of the coupling between the spins of transition metal ions and active EPR states depend strongly on the nature of these ions. The spectrum of one Cu(II)-tetranuclear polyoxometalate cluster is explained considering a superposition of the spectra for the (S,S_{13},S_{24}) type states: (1,1,0), (1,1,1) and (1,0,1).

1. Introduction

Many structural aspects of some supramolecular systems were evidenced in the last years by different spectroscopic methods [1-6]. One of their most interesting property is that of molecular recognition quality. Molecular recognition mechanism is very important in biological systems such as chelating of some metal ions and transport them in the living cell or in the replication and transcription of the genetic code in the reproduction and genetics of living organisms [2,3].

Metal complexes of some drugs have been found to be more potent and desirable products than their parent drugs. The hypothesis that copper compounds might be active as antiinflammatory agents is supported by the finding that copper complexes are effective against arthritic and other degenerative diseases of man. In addition, these metal complexes exhibit a variety of new pharmacological effects such as antiulcer, antidiabetic, anticancer, anticonvulsant and radiation recovery activities [7,8].

Sandwich-type heteropolyoxometalates (HPOM) encapsulating clusters of early transition metals have received much attention both from applied medicine, catalysis [9,10]. The great advantage of these complexes is the possibility of varying the type of the metallic cluster (its structural topology and the nature of the transition metals). The proximity of the transition metals possessing unpaired electrons facilitates their coupling through exchange, superexchange or dipolar interactions.

The studied compounds were prepared at the Faculty of Chemistry of the Babeş-Bolyai University. EPR and HF-EPR measurements were performed at ~9.5 GHz (JEOL-JES-3B and Bruker ESP 380 spectrometers) and 190 GHz (HF-EPR Grenoble spectrometer) in the 5-293 K temperature range.

2. Results and discussion

a) Dimeric species in antiinflamatory and cardiovascular drugs

The following Cu(II)–complexes with antiinflammatory drugs were prepared and investigated by EPR method: $[Cu_2(aspirinate)_4](H_2O)_2$, $[Cu_2(indomethacin)_4](H_2O)_2$ and $[Cu(ibuprofen)_2](H_2O)_2$. Generaly these compounds adopt a dimeric structure as shown in Fig. 1 [5].

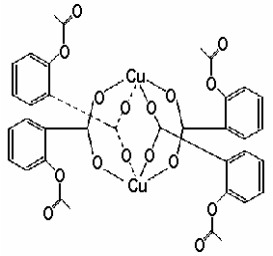

Fig.1. The binuclear structure of $Cu_2(Asp)_2$ complex

Powder EPR spectrum of $[Cu_2(aspirinate)_4](H_2O)_2$ complex, measured at room temperature, exhibits absorptions typical of randomly oriented triplet state (S = 1) species characterized by a strong antiferromagnetic exchange coupling (J = –288 cm^{-1}) and an axial symmetry with a small rhombic distortion. The $[Cu_2(indomethacin)_4](H_2O)_2$ spectrum (Fig.2a) suggests the presence of two kinds of dimeric species: one of them characterized by a short Cu–Cu distance (≅2.7 Å) analogous to the dominant form of Cu(II)–aspirinate complex and the other type in which the metal–metal distance is bigger (≅4-5 Å) than in the first case. The spin–spin coupling is realized in the second dimmers through the dipole–dipole interaction [5].

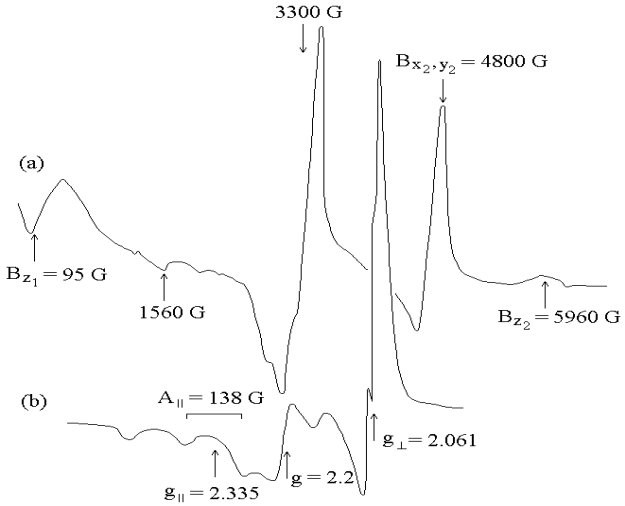

Fig.2. Powder EPR spectra of Cu(II)–indomethacin (a) and (Cu:Zn)–indomethacin (b) complexes

The mononuclear Cu(II) species appear in indomethacin by a magnetically dilution with Zn(II) (Fig.2b). The characteristic EPR parameters of these species: $g_{\|} = 2.335$, $g_{\perp} = 2.061$, $A_{\|} = 138$ G and $A_{\perp} = 20$ G suggest a tetrahedral (T_d) coordination of Cu^{2+} ions. Using the LCAO–MO scheme described in the paper [11], a mixture of $3d_{xy}$ and 2% $4p_z$ copper orbitals results for the paramagnetic electron ground state. The more intense g = 2.2 signal from the parallel band may be attributed to a little amount of monomeric species with d_z2 ground state [12].

Cu(II) compounds of dihydrazinophthalazine which is an hypotensive and cardiovascular drug adopt also a dimeric structure (Fig. 3). A similar coordination mode has been also recently reported in the case of copper(II)-bilirubinate (BR) complex where the Cu^{2+} ion is bonded to four nitrogen atoms coming from two molecules of BR [13]. The magnetic field resonance absorption values of the triplet state (S=1) EPR spectrum allowed us to calculate the $g_{\|,}$ $g_{\perp}$, D, E an J parameters following the procedure described by Chasteen [14]. The results are given in Table 1.

Table 1

Magnetic parameters for Cu(II)-1-4 dihydrazinophthalazine complexes at room temperature.

Compound	2 |J| (cm^{-1})	$g_{\|}$	$g_{\perp}$	D (cm^{-1})	D_{dd} (cm^{-1})	$D_{exch.}$ (cm^{-1})	E (cm^{-1})
$[CuCl_2 \cdot DHF \cdot H_2O]_2 \cdot 2H_2O$	105	2.322	2.092	0.072	-0.116	0.186	-0.024
$[CuBr_2 \cdot DHF \cdot H_2O]_2 \cdot H_2O$	95	2.281	2.078	0.062	-0.156	0.218	-0.023

It was observed also that non steroidal ligands are partially or totally substituted by DMF or pyridine solvent molecules in solutions. Thus the following $Cu(Asp)_2(DMF)_2$, $Cu(Asp)_2(Py)_2$, $Cu(DMF)_4$, $Cu(Py)_4$ types of monomeric species with different chromophores and local symmetries were evidenced.

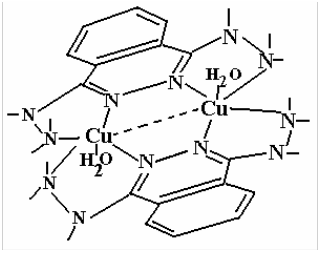

Fig.3. The structure of binuclear Cu(II)-DHP complexes.

The most interesting mononuclear species for their anti-tumor activity is $Cu(Asp)_2(Py)_2$, with CuO_2N_2 chromophore. The copper (II) ion is bonded in a trans square-planar arrangement to the nitrogen atoms of two pyridine molecules and two aspirinate anions [2]. The existence of CuO_2N_2 chromophore is confirmed by the presence of nitrogen super-hyperfine lines in the $g_{\perp}$ region of the spectra.

b) Trinuclear mettalic clusters in some heteropolyoxometalates

Heteropolyoxometalates (HPOM) are supramolecular blocks of metal oxide formed by WO_6 and/or MoO_6 octahedra sharing vertices or edges (Fig.4). The metallic clusters are usually encapsulated between two Keggin or Dawson-Wells trilacunary fragments. In this context, our research focuses on the EPR and HF-EPR investigation of Bi^{III} based sandwich-type HPOM with three 3d transition metals $[M^{n+}{}_3(H_2O)_x(BiW_9O_{33})_2]^{(18-3n)-}$ ($M^{n+} = (VO)^{II}$, x = 0 and $M^{n+} = Cr^{III}$, Co^{II}, Ni^{II}, Cu^{II}, x = 3).

Powder EPR spectrum of the complex with vanadyl ions obtained at room temperature was simulated as a superposition of two Gaussian components, an axial and a broad isotropic one. The axial component is characteristic for isolated V^{IV} ions in a C_{4V} local symmetry (g_{II} = 1.899, $g_{\perp}$ = 1.974, A_{II} = 184 G, $A_{\perp}$ = 69 G) with a well resolved hyperfine structure. The broad component of the spectrum could be interpreted in therms of the presence of very weak extended exchange interaction within the vanadyl triangular cluster (S= 3/2). These lead to the appearance of two doublets (S = 1/2) and an excited quartet (S = 3/2). This last state could be responsible for the appearance of the broad component of the spectrum, because of the unsolved hyperfine structure and possible g and A tensors anisotropies [15].

The degree of covalency of the in-plane V–O π bonds (β_2^2) was evaluated using the LCAO-MO approach for V^{IV} with antibonding $B_2(d_{xy})$ ground state, in a C_{4v} local symmetry [16]:

$$\beta_2^{\,2} = \frac{7}{6}\left[-\frac{A_{II} - A_{\perp}}{P} + (g_{II} - g_e) - \frac{5}{14}(g_{\perp} - g_e)\right] \qquad (1)$$

where $P = g_e\mu_B g_N\mu_N\langle r^{-3}\rangle$ = 0.0128 cm^{-1} is the dipolar interaction term for the vanadyl ion, g_e = 2.0023 is the g factor of the free electron and $\Delta E_x2_{-y}2$ = 14705 cm^{-1} is the energy of the $^2B_2(d_{xy}) \rightarrow {}^2B_1(d_x2_{-y}2)$ transition obtained from the VIS spectrum. The Fermi contact term was determined as $K = -(A_0 / P) - (g_e - g_0)$, where $A_0 = (A_{II} + 2A_{\perp})/3$ and $g_0 = (g_{II} + 2g_{\perp})/3$. The β_2^2 = 0.876 value indicates a dominant ionic character of the in-plane π bonds, but there is also a covalent degree of them. The delocalization of the vanadium unpaired electron towards the neighboring oxygen atoms is confirmed by the low K = 0.705 Fermi contact term and the negative signs of A_{II} and $A_{\perp}$ parameters, the only situation which gives rise to acceptable values for the molecular orbital coefficients.

The EPR parameters and the shape of the spectrum remain nearly unchanged at the temperature of 80 K. While the linewidths of the hyperfine signals do not vary when the temperature rises from 80 K to 293 K, the intensity of the whole spectrum strongly decreases. Particularly, the intensity of the ΔM_I = –5/2 hyperfine line decreases about 23 times. The fact that the proportionality I ~ 1/T, where I is the amplitude of the signal, is not observed, points to a non-Curie behavior of the complex due to the V^{IV}–V^{IV} coupling [17].

HF-EPR spectra of the polycrystalline complex with three Cr^{III} ions, obtained at 190 GHz and 5–200 K temperature range contain a broad line at g ≈ 2.0. By raising the temperature, the linewidth of the signal decreases because of small Cr^{III}–Cr^{III}

superexchange interactions. The temperature dependence of the inverse of the linewidth was fitted taking into account the proportionality $(\Delta B(p\text{-}p))^{-1} \sim \chi_M T$, with χ_M being the molar susceptibility, and in the frame of a HDVV model for three exchange-coupled high-spin Cr^{III} ions ($S_1 = S_2 = S_3 = 3/2$) [18]:

$$\chi_M T = (N\mu_B{}^2 g^2/3k)(3x^{3/8} + 60x^{15/8} + 157.5x^{35/8} + 252x^{63/8} + 247.5x^{99/8})/ \\ (4x^{3/8} + 16x^{15/8} + 18x^{35/8} + 16x^{63/8} + 10x^{99/8}) \quad (2)$$

where x = exp(J/kT) and all other parameters have their usual meanings. The best fit was obtained with J = –4.116 cm^{-1} and considering the g = 1.995 mean value in the temperature range of 5–85 K.

The three Cr^{III} ions are antiferromagnetically coupled as arises from the negative value of the exchange coupling constant. The spin states obtained by coupling antiferromagnetically three S = 3/2 spins which form an equilateral triangle are all degenerate except the highest S = 9/2 state. The fast relaxation between degenerate states owing to a spin frustration effect makes EPR signals too large and masks the fine structure.

HF-EPR spectra (190 GHz) of the pollycrystaline complex with Co^{II} ions pressed in a pellet exhibit at 5 K at least four signals (Fig.5). The ratio of the intensities for the two signals at lower magnetic fields is almost constant in the temperature range 5–50 K, which indicates that they originate in the same spin state. This spectrum was simulated by superposing in 2:1 ratio the spectra of two distinct species (g_{x1} = 5.021, g_{y1} = 3.561, g_{z1} = 2.401 and g_{x2} = 5.776, g_{y2} = 3.813, g_{z2} = 2.850), characterised by the same effective spin S_{eff} = 1/2 for three antiferromagnetic coupled Co^{II} ions.

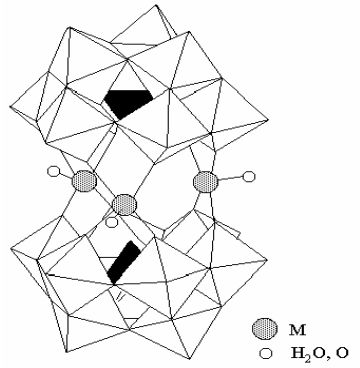

Fig. 4 The $[M_3^{M+}(H_2O)_x(BiW_9O_{33})_2]^{(18-3n)-}$ *heteropolyanion structure*

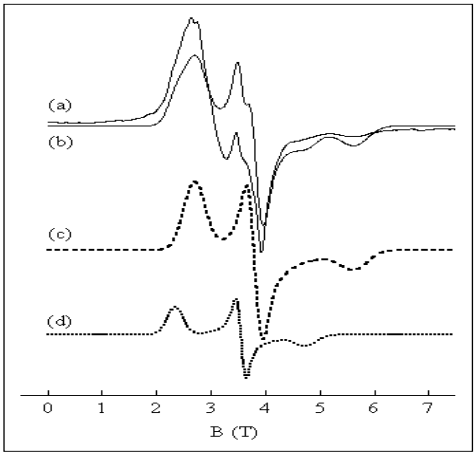

Fig.5 (a) HF-EPR spectrum (190 GHz) at T = 5 K of a polycrystalline sample of the complex with Co^{II} pressed in a pellet and (b) the simulated spectrum as sum of the spectra (c) and (d) assuming S = 1/2 spin state

Spectra of the pollycristaline

sample with Ni^{II} were interpreted in terms of one S = 1 spin state for three antiferromagnetic coupled Ni^{II} ions (Fig.6). The magnetic fields for allowed $\Delta M_S = \pm 1$ transitions estimated from the spectrum at 5 K were used for supplying the EPR parameters by means of Chasteen procedure [14]. The cluster presents a small rhombic distortion both in **g** (g_x = 2.201, g_y = 2.211 and g_z = 2.292) and **D** tensors (D = 1.66 cm^{-1} and E = 0.18 cm^{-1}).

In the case of the Cu^{II} complexes the antiferromagnetic coupling between the Cu^{II} ion, favorised by the geometry of the cluster and the spin frustration [19], leads to a double degenerate S = 1/2 ground state, which is EPR inactive, and one excited state (S=3/2) EPR active (Fig.7). The best fit of the spectrum was obtained with an axial spin Hamiltonian with S = 3/2, principal g values $g_{\parallel}$ = 2.080, $g_{\perp}$ = 2.237 and the axial zero field splitting parameter D = 0.0214 cm^{-1}. The parallel direction is along the C_3 axis of the trinuclear copper cluster and also along the perpendicular direction of the individual **g** tensors.

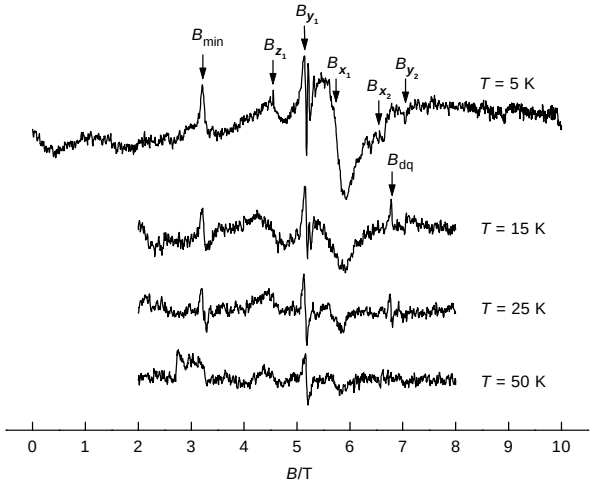

Fig. 6. Temperature dependence of the HF-EPR spectra at 190 GHz of the polycrystalline complex $Na_{12}[Ni_3(H_2O)_3(BiW_9O_{33})_2]\cdot 39\ H_2O$ pressed in a pellet.

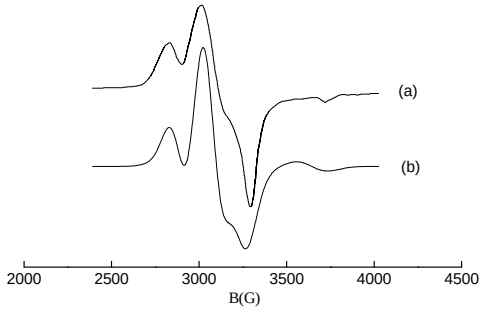

Fig.7. Powder EPR spectrum of the $Na_{12}[Cu_3(BiW_9O_{33})_2(H_2O)_3]\cdot 29H_2O$ complex (X-band, T=293 K) (a) experimental spectrum, (b) simulated spectrum

c) Tetranuclear metallic clusters

Sandwich-type heteropolyoxometalates (HPOM) in which four d-electron transition metal ions link two trivacant Keggin or Dawson-Wells fragments are intensely studied for their capacity of formation of high spin magnetic clusters, for their catalytic and antiviral activity [9,10].

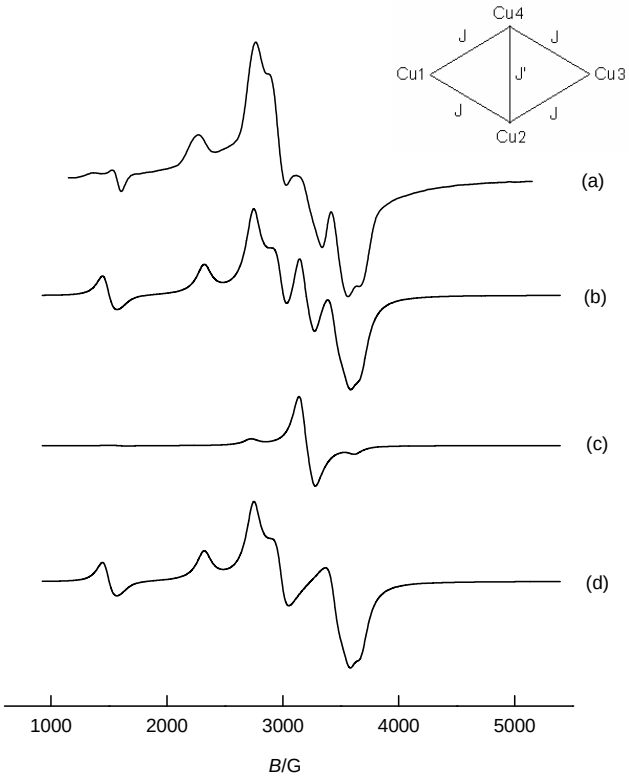

Fig. 8. (a) Experimental EPR spectrum of the Cu^{II}–HPOM complex obtained at T = 293 K and (b) the simulated spectrum obtained as sum of the components (c) and (d) in the 7:13 ratio.

The heteropolyoxometalate $Na_{10}[Cu_4(H_2O)_2(AsW_9O_{34})_2]\cdot 23H_2O$ was investigated by EPR for obtaining information about the interaction between the four Cu(II) ions. The main signals of the spectrum are typical for one S = 1 spin state, obtained through isotropic antiferromagnetic interactions between the electronic spin angular momentum operators of the Cu^{II} ions. Using the Kambe model for the tetranuclear cluster of Cu^{II} ions, characterised by two exchange parameters J and J' [20,21] ($J_{24}' \cong$ -12.5 cm^{-1}, $J_{12,14,23,34} \cong$ -3.5 cm^{-1} for similar complexes) and presenting the energetical states (S, S_{13}, S_{24}), the EPR parameters have been etimated: g_x = 2.055, g_y = 2.205, g_z = 2.330, D = 0.068 cm^{-1} and E = 0.0008 cm^{-1} for the ground state (1,1,0) (spectrum c) and g_x = 2.114, g_y = 2.030, g_z = 2.292, D = 0.029 cm^{-1}, E = 0.0049 cm^{-1} for the excited (1,1,1) and (1,0,1) states (spectrum d).

4. Conclusions

Powder EPR spectra of Cu(II) – complexes with antiinflammatory and cardiovascular drugs suggest the presence of dimeric species in which the spin of copper ions are coupled by strong exchange interaction.

The most interesting mononuclear species for their anti-tumor activity is $Cu(Asp)_2(Py)_2$ with CuO_2N_2 chromofore.

The presence of trinuclear metallic clusters was evidenced for all polyoxometalates with transitional ions. Thus in case of vanadium compounds a weak superexchange interaction prevails which lead to the S = 1/2 ground state and the excited S = 3/2 state. Trinuclear Cr^{III} cluster has an isotropic g = 1.995 factor and the chromium ions are antiferromagneticaly coupled (J = -4.116 cm^{-1}). Co^{II} cluster is characterized by the effective spin S = 1/2 and the sample is a mixture of two nonequivalent species (g_x^1 = 5.021, g_y^1 = 3.561, g_z^1 = 2.401 and g_x^2 = 5.776, g_y^2 = 3.813, g_z^2 = 2.850).Ni^{II} cluster has one S = 1 ground state and g (g_x = 2.201, g_y = 2.211, g_z = 2.292) and D (D = 1.66 cm^{-1}, E = 0.18 cm^{-1}) rhombic tensors. Trinuclear Cu^{II} cluster has an EPR inactive S = 1/2 doublet as ground state and an excited state S = 3/2 ($g_{||}$ = 2.080, $g_{\perp}$ = 2.237, D = 0.0214 cm^{-1}).

EPR spectrum of the $Na_{10}[Cu_4(H_2O)_2(AsW_9O_{34})_2]\cdot 23H_2O$ heteropolyoxometalate was explained in therm of antiferromagnetic interaction between the four Cu(II) ions and a superposition of the spectra for the (S, S_{13}, S_{24}) (1,1,0), (1,1,1) and (1,0,1) states.

REFERENCES

1. A. Ikeda, T. Hatano, T. Konishi, J. Kikuchi, S. Shinkai, Tetrahedron, 59, 3537 (2003)
2. Z. Yehuda, Y. Hadar, Y. Chen, J. Agric. Food Chem., 51, 5996 (2003)
3. R. Ludwig, N.T.K. Dzung, Sensors, 2, 397 (2002)
4. O. Cozar, I. Bratu, L. David, C. Craciun, A. Hernanz, R. Navarro, M. Fuente, C. Balan, Appl.Magn.Reson. 21, 71 (2001)
5. L. David, O. Cozar, V. Chis, A. Negoiescu, I. Vlasin, Appl.Magn.Reson. 6, 521 (1994)
6. D. Rusu, C. Craciun, A. L. Barra, L. David, M. Rusu, C. Rosu, O. Cozar, Gh. Marcu, J. Chem. Soc., Dalton Trans,, 19, 2879 (2001).
7. J. R. J. Sorenson, Metal Ions in Biological Systems (H. Siegel, Ed.), Marcel Dekker, New York, 14, 77 (1982)
8. R.P. Ferrari, L. Paradisi, M. Torrielli, Anticancer Res., 9, 771 (1989)
9. Y. Inouye, Y. Fujimoto, M. Sugiyama, T. Yoshida, T. Yamase, Biol. Pharm. Bull, 18,996 (1995)
10. X. Zhang, T.M. Anderson, Q. Chen, C.L. Hill, Inorg. Chem., 40, 418 (2001)
11. O. Cozar, I. Ardelean, J. Non Cryst. Solids, 92, 278 (1987)
12. E. Forizs, L. David, O. Cozar, V. Chis, R. Tetean, M. Todică, Appl.Magn.Reson., 16, 499 (1999)
13. J.R. Ferraro, J.G. Wu, R.D. Soloway, W.H. Li, Y.Z. Xu, D.F. Xu, G.R. Shen, Appl. Spectrosc., 50, 923 (1996)
14. N. D. Chasteen, Inorg. Chem., 10, 2339 (1971)
15. T. Yamase, B. Botar, E. Ishikawa, K. Fukaya, Chem. Lett., 1, 56 (2001)
16. A. Bencini, D. Gatteschi, in “Transition Metal Chemistry”, Marcel Dekker, New York, 1982, vol.8, p.59
17. D. Collison, D.R. Eardley, F.E. Mabbs, A.K. Powell, S.S. Turner, Inorg. Chem., 35, 4974 (1996)
18. O. Kahn, in “Molecular Magnetism”, VCH Publishers, Inc., New York, 1993, p.212.
19. P. Chaudhuri et al., Inorg. Chem., 30, 2148 (1991)
20. U. Kortz, S. Nellutla, A.C. Stowe, N.S. Dalal, U. Rauwald, W. Danquah, D. Ravot, Inorganic Chemistry, Vol. 43, No. 7, 2308 (2004)
21. C. J. Gómez-García, E. Coronado, P. Gómez-Romero, N. Casañ-Pastor, N. Inorg. Chem. 32, 3378 (1993)

STUDIA UNIVERSITATIS BABEŞ-BOLYAI, PHYSICA, XLIX, 2, 2004

TWO-PHOTON ABSORPTION OF ORGANICS: FROM SPECTROSCOPY TO PHOTODRIVEN MICROSENSORS

P.L. BALDECK, C.-L. LIN[1], C. ANDRAUD[2]

[1]Laboratoire de Spectrométrie Physique, Université J. Fourier, CNRS (UMR 5588) 38402 Saint Martin d'Hères, France
[2]Ecole Normale Supérieure de Lyon, Laboratoire de Stéréochimie et Interactions Moléculaires, UMR 5532, 46, allée d'Italie, 69364 Lyon Cédex 07, France.

ABSTRACT. We report on an oligomer strategy that leads to fluorescent molecules with large two-photon cross-sections. Then, we present our recent work on photodriven polymer microsensors for microfluidic applications.

1. INTRODUCTION

Applications related to two-photon absorption (TPA) with organics are very attractive for different fields : 3D-fluorescence imaging,[1] 3D optical data storage,[2] 3D lithographic microfabrication,[3] photodynamic cancer therapy,[4] and optical power limiting.[5] Different strategies have been developed to synthesize organic molecules with large two-photon absorption. They are based on the concept of charge transfer in π-conjugated structures substituted with electron donor or acceptor groups, and are very efficient for applications in the near infrared.[6]

In the first part of this paper, we report on a fluorene oligomer strategy that leads to large two-photon cross-sections in the visible range. This oligomer strategy is based on the enhancement of transition dipole moments due to the coupling between monomers.

In the second part of this paper, we focus on a microfabrication application of TPA-induced polymerization. Polymer microsensors have been fabricated. They can be manipulated and powered using a strongly focussed CW Nd:YAG laser.

2. FLUORENE OLIGOMERS FOR TWO-PHOTON ABSORPTION APPLICATIONS

The chemical structure of fluorene oligomers (*N*-PDHF) is shown on Figure 1.

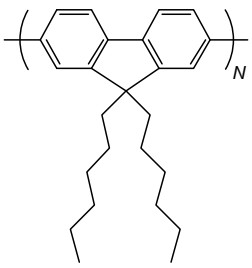

Fig. 1. Chemical structure of *N*-PDHF oligomers

TPA spectra were obtained by up-conversion fluorescence measurements, using a Nd:YAG pumped optical parametric oscillator which produces 2.6 ns pulses (FWHM) in the 450-650 nm range. The TPA cross-section was determined at 600 nm, using *p*-bis(*o*-methylstyryl) benzene as reference.

TPA absorption spectra of *N*-PDHF oligomers are presented on Figure 2. These systems exhibit broadband spectra between 500 to 700 nm. A bathochromic effect is observed when increasing the oligomer length.

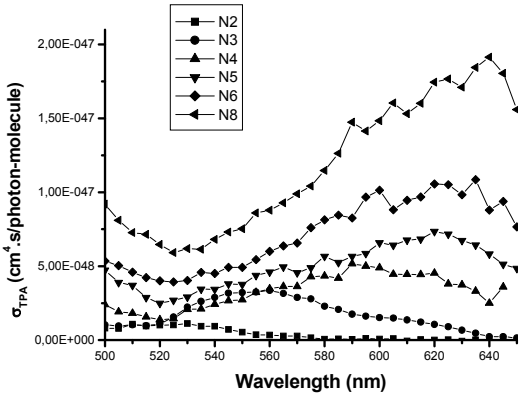

Fig. 2. TPA spectra of *N*-PDHF oligomers

The most relevant parameter allowing to rationalize the TPA efficiency of oligomers is the cross-section density σ_{TPA}/N, which permits to cancel concentration effects due to the increase of the number of monomer units and to really determine the influence of the length of the oligomer (Figure 3).

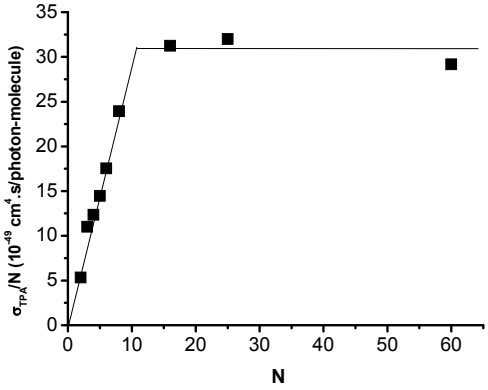

Fig. 3. TPA cross-section density of *N*-PDHF with the oligomer length.

There is linear increase of σ_{TPA}/N for the shortest molecules (N<10), and a saturation for the longest ones (N= 16, 25 and 60).

Variations of σ_{TPA}/N with N can be readily analyzed from the excitonic model. The coupling between monomers induces variations following Eq. (1) of oligomer dipole moments $\mu_{ij}(N)$ for the transition $i \rightarrow j$ with $\mu_{ij}(1)$ of the corresponding monomer.

$$\mu_{ij}(N) = \sqrt{N}\,\mu_{ij}(1) \tag{1}$$

Using the three-level model, the TPA cross-section σ_{TPA} is given by:

$$\sigma_{TPA} \propto \frac{\mu_{01}^2 \mu_{12}^2}{(E_{01} - \frac{E_{02}}{2})^2 \Gamma} \tag{2}$$

where E_{ij} is the transition energy and Γ the damping constant.

Thus, the variations of σ_{TPA} with N, if assuming that the influence of the denominator can be neglected, is given by:

$$\sigma_{TPA}(N) = N^2 \sigma_{TPA}(N=1) \tag{3}$$

This expression remains valid for $N < N_e$ (N_e is the number of monomer corresponding to the effective conjugation length). For $N > N_e$, $\sigma_{TPA}(N)$ becomes proportional to $\sigma_{TPA}(1)$. Thus, as observed experimentally, the excitonic model leads to a linear variation of σ_{TPA}/N with N for $N < N_e$, and a saturation for $N > N_e$.

3. TPA-INDUCED POLYMERISATION OF PHOTODRIVEN MICROSENSORS

TPA induced photopolymerization is a very attractive method for the fabrication of three-dimensional (3D) microstructures. The chemical polymerization reaction occurs at the laser focus where the photoiniator chromophore is excited by the simultaneous absorption of two photons. 3D micrometer-size objects with resolution as good as 200nm can be produced.

Linearly polarized optical tweezers are efficient tools to control the position and orientation of dielectric anisotropic micro-objects. When such objects are trapped by a tightly focused beam, they tend to align parallel to the direction of the electric field polarization. The orientation or angular motion of the object can be obtained by rotating the linear light polarization with a half-wave plate.

We report on the fabrication and demonstration of polymer microsensors. They are made using a low-cost TPA-induced microfabrication technique based on a efficient TPA photoinitiator and a Nd:YAG microlaser. These microsensors are photodriven with an optical tweezers.

The microfabrication technique has been described earlier.[7] The resin consists in a commercial resin (Photomer 3015 from Henkel) to which 1% photoinitiator is added to enhance two-photon absorption properties. The photoinitiator molecule is (N^4,$N^{4'}$-bis-(4-methoxyphenyl)-N^4,$N^{4'}$-diphenyl-4,4'-diaminobiphenyl). A small quantity of resin is deposited on glass coverslip to form a film with an approximate thickness of 30 µm. The experimental setup is based on an inverted microscope (Zeiss Axiovert). Two-photon excitation is achieved by a frequency doubled Nd:YAG microlaser from JDS Uniphase (λ=532 nm, pulse duration 0.5 ns, maximum pulse energy 4 µJ,

repetition rate 6.5 kHz) focussed through a microscope objective lens (magnification $\times$100, numerical aperture 1.25). Polymerization occurs at the focal point. A 3-axis piezoelectric stage is used to translate the sample with respect to the laser focus in order to produce the desired structure. A few drops of acetone are added to dissolve the unexposed resin and to free the polymer micro-objects, which can be trapped when floating in acetone.

We have used this TPA-induced polymerization technique to fabricate microsensors for viscosimetry, velocimetry and micropump applications (Fig. 4). Hundreds of sensors are free-floating in the liquid to be characterized. When the optical tweezers is turned on, one sensor is trap at the focal point. To maximize the laser-dielectric interaction, its longest dimension aligns in the laser direction. In the case of a slab shape and a linearly polarized laser, the microsensor rotates to align itself in the polarization direction. Hence, the optical-tweezers can be used to control the sensor position and angle, but also to generate an optical torque that can be used for local hydrodynamic measurements, i.e. viscosity and fluid velocity.

The viscosity microsensor is based on a micro-slab ($4\times2\times0.7\mu m^3$) that is trapped and rotated using a linearly polarized optical tweezers (Fig. 5). The slab rotation is controlled by a half-wave plate. The optical torque is compensated by the drag torque. Hence, the fluid viscosity can be deduced from the rotation characteristics.

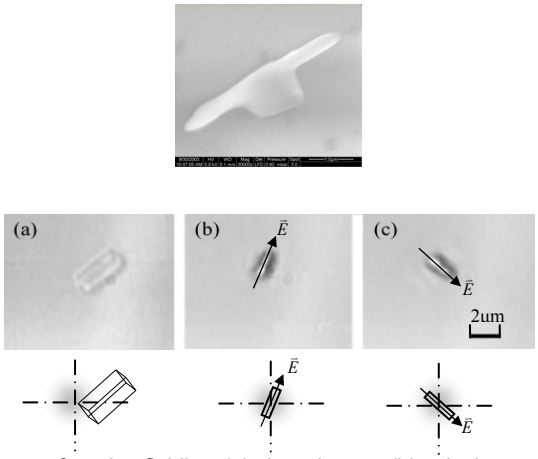

Fig. 4. Microsensors for microfluidics: (a) viscosimetry, (b) velocimetry, (c) micropump

Fig. 5. Micro-slab in different positions: (a) laser “off”: free-floating, (b) laser “on”: the micro-slab is trapped, (c) the micro-slab follows the half-wave plate rotation.

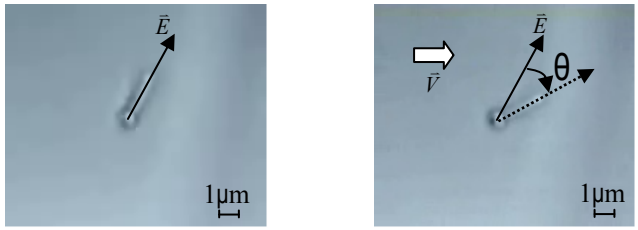

(a) (b)

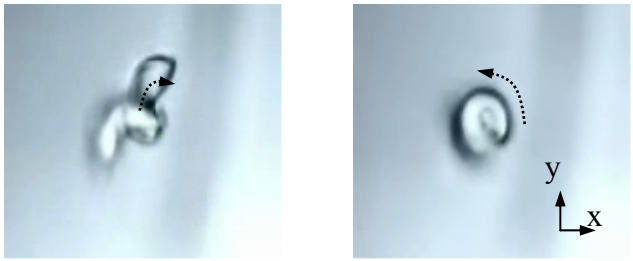

(a) (b)

Fig. 6. Velocimetry sensor: (a) at rest the flat slab is aligned in the polarization direction; (b) v ~ 40μm/s, the sensor rotates to an equilibrium angle

Fig. 7. Photodriven micropump behavior

The velocimetry sensor behavior is shown in Fig. 6. At rest the linearly polarized optical tweezers traps the microsensor at the focal point, and the flat-plate gets aligned in the polarization direction (Fig. 6a). Under a fluid flow, the plate rotates to an equilibrium angle that is used to measure the fluid velocity (Fig. 6b).

The micropump behavior is shown in Fig. 7. When a free-floating pump is approaching the laser focus (Fig. 7a), it gets trap, aligns its axis in the laser direction, and starts to rotate around its axis (Fig. 7b). This rotation generates a propulsive force on the fluid. The rotation frequency ranges from few Hz to tens of Hz, depending on the laser power, screw geometry, and fluid viscosity. The rotation is due to the optical torque transferred to the object by the laser scattering.

REFERENCES

1. W. Denk, J.H. Strickler, W.W. Webb. *Scienc*e, **248**, 73 (1990)
2. J.H. Strickler, W.W. Webb. *Optics Letters*, **16**, 1780 (1991)
3. S. Maruo, O. nakamura, S. Kawata. *Optics Letters*, **22**, 132 (1997)
4. A.M.R. Fisher, A.L. Murphree, C.J. Gomer, *Laser Surg. Med.*, **17**, 2 (1995)
5. G.S. He, J.D. Bhawalkar, C.F. Zhao, P.N. Prasad, *App. Phys. Lett.*, **67**, 2433 (1995)
6. M. Albota, D. Beljonne, J.L. Brédas, J.E. Ehrlich, J.Y. Fu, A.A. Heikal, S.E. Hess, T. Kogej, M.D. Levin, S.R. Marder, D. McCord-Maughon, J.W. Perry, H. Röckel, M. Rumi, G. Subramaniam, W.W. Webb, X.L. Wu, C. Xu, *Science* **281**, 1653 (1998).
7. I. Wang, M. Bouriau, P.L. Baldeck. *Optics Letters*, **27**, 1348 (2002)

STUDIA UNIVERSITATIS BABEŞ-BOLYAI, PHYSICA, XLIX, 2, 2004

STUDY OF MATERIALS NANOSTRUCTURE BY SMALL ANGLE NEUTRON SCATTERING

ADÉL LEN[1], LÁSZLÓ ROSTA[1], ESZTER RÉTFALVI[1], PÉTER HARMAT[2], MASSIMO ROGANTE[3]

[1]Research Institute for Solid State Physics and Optics, H-1525, P.O.B.49, Budapest, Hungary, e-mail: lenadel@sunserv.kfki.hu
[2]Research Institute for Technical Physics and Materials Sciences, Budapest
[3] Rogante Engineering Office, Civitanova Marche, Italy

ABSTRACT. The small angle neutron scattering (SANS) method is a technique for studying structural features from *1* to *100 nm* in size in various materials such as porous media, polymers, solutions of micelles, membranes, ceramics, metals, etc. The very low energies of thermal neutrons allow them to penetrate in most materials without destructing them. The possibility to substitute hydrogen for deuterium makes SANS a unique technique for investigating macromolecular structures in synthetic and biological polymers. The SANS technique includes the determination of void sizes and their distributions in porous media as well as the investigation of particle agglomeration and evolution of pores during sintering. SANS is also useful for the understanding of the thermodynamics of two-phase systems. In this paper some examples are presented; the different structure investigations were performed recently at the Budapest Neutron Center at „Yellow Submarine" SANS spectrometer.

The Method of SANS

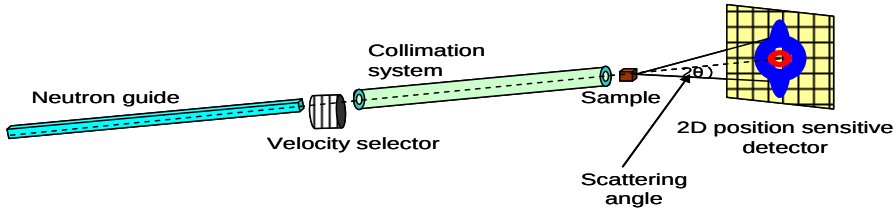

Fig.1 The scheme of the SANS facility

The most important "actors" of a SANS expriments are the neutrons. They are produced in our case in the tank type reactor with 10 MW power; then they are light water moderated and cooled [1]. Monochromatic wavelength neutrons are selected by a multidisc type velocity selector. The wavelength can be varied between *3* and *24Å*. The neutrons are guided through a supermirror guide system to the sample. The beam is formed by a *5m* long collimation system with variable slit sizes (Fig.1). The vacuumed collimator tube can be changed automatically by a neutron guide section or by a multibeam type collimator [2].

The scattered neutrons are detected by BF_3 filled, two dimensional position sensitive detector with 64x64 pixels. The SANS instrument Yellow Submarine covers a Q-range from 0.004 $Å^{-1}$ to 0.5 $Å^{-1}$ allowing density, composition and magnetization

fluctuations in materials to be measured on a length scale from 5 Å to 1000 Å. The primary data treatment can be made by regrouping the two-dimensional scattering patterns, background subtraction, correction for transmission and normalization to standard samples. When a monochromatic plane wave illuminates a sample, scattered waves of variable intensities are emitted in all directions of space. The incident and scattered wave at an angle of 2θ can be described by their wave vectors $\bar{k}_0$ and $\bar{k}_1$, which defines the $\bar{q}$, scattering vector: $\bar{q} = \bar{k}_1 - \bar{k}_0$. In case of elastic scattering: $|\bar{q}| = \frac{4\pi \sin\theta}{\lambda}$. The measured intensity at the detector can be expressed as follows: $I(\lambda,\theta) = I_0(\lambda)\Delta\Omega\eta(\lambda)TV\frac{\partial\sigma}{\partial\Omega}(q)$, where I_0 is the incident flux, η is the detector efficiency, T is the sample transmission, V is the sample volume and $(d\sigma/d\Omega)(q)$ is a function known as the microscopic differential cross-section. $(d\sigma/d\Omega)(q)$ has dimensions of (length)$^{-1}$ and is normally expressed in units of cm^{-1}. The objective of a SANS experiment is to determine the differential cross-section, which contains information on the shapes, sizes and interactions of the scattering objects in the sample. [3,4]

Tungsten wires

Doped tungsten wires are the most frequently used materials for lighting, electronic devices, thermocouples, cathodes. During commercial fabrication tungsten, doped with K, Al and Si, is pressed and sintered into bars. During the sintering most impurities escape, except a part of potassium, which remains in bubbles during the whole life of the lamp. The presence of potassium filled bubbles with characteristic diameter of *100 nm* is responsible for the quality of the wire. We have shown how the potassium bubble inclusions structure changes during the annealing of the wires. The form of pores and bubbles follows the macroscopic deformation of the wire. During heat treatment ellipsoids became spherical bubbles or break up into rows of bubbles. After many steps of rolling and wire drawing the *0.5 mm* diameter tungsten wire samples were annealed at different temperatures, *700℃, 1150℃, 1450℃, 1850℃, 2200℃* , and one sample was unannealed (Fig.2).

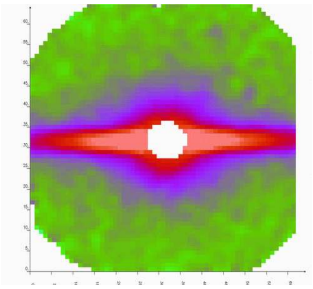

Fig.2. 2D SANS intensity distribution of an unannealed tungsten wire sample

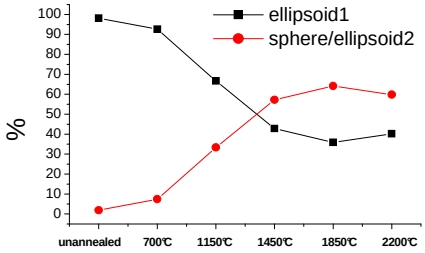

Fig.3. Change of the different shaped surfaces (ellipsoid1-very elongated, ellipsoid2-less elongated inclusion)

Previous experiments have shown that the anisotropy vanishes completely after full annealing of the sample, as each ellipsoid brakes up into rows of spherical bubbles. From our measurement it follows that even at the highest studied annealing temperatures a substantial amount of ellipsoidal inclusions remain in the wires (Fig.3). From this investigation one can deduce how the annealing temperature of the tungsten wires should be choosen, for provideing maximum spheroidisation of the potassium bubbles in order to prolongate the lifte-time of wires. [5]

Car engine piston

To solve the problem of long-term materials exploitation under extreme thermal and mechanical stresses in car's motors one needs the application of novel modern methods which enable to examine the material state and to predict some phenomena being the precursors of possible fracture. The analysis of SANS scattering patterns in deformed metals especially in the fracture zone, showed that the main sources of scattering are microcracks. The 5 different points (possible critical locations) of a new and an old (*400km* use) piston, made from commonly used Al 4032 alloy, have been investigated, as shown in Fig.4.

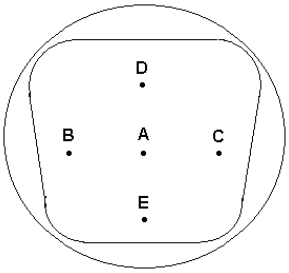

Fig.4. Investigated points either in the new, or in the old piston crown

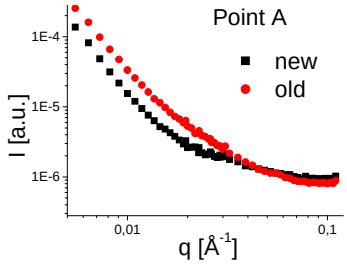

Fig.5. SANS intensities of a new and an old sample

The evaluation of shape and size of precipitates are useful to locate the areas of maximum thermal alteration and evaluate the velocity of the alteration. It was found that in the precipitate's ensemble the particles with characteristic radius $R \approx 100Å$ dominate. Comparing the parameters for new and old piston (Fig.5), we conclude: the aging leads to the increase of the interior surface by *~20%*, the size of the precipitates increase, and the small defects (vacancies) are annealed by use [6].

REFERENCES

1. L. Rosta, *Appl. Phys. A,* **2002**, *74* [Suppl.], S52-S54
2. A. Len, G. Pépy, L. Rosta: *Physica B,* **2004***, 350, 1-3,* [Suppl.1], E771-E773
3. O. Glatter, O. Kratky: *Small Angle X-ray Scattering* (Academic Press INC, London **1982**)

4. S. M. King: Small Angle Neutron Scattering, **1995**, U.K
5. A. Len, P. Harmat, G. Pépy, L. Rosta, P. Schade: *J. of Appl. Chryst.,* **2003**, 36, 621-623
6. E. Rétfalvi, M. Rogante, F. Nicolae, L. Rosta, V.T. Lebedev: *Physica B* - in print

STUDIA UNIVERSITATIS BABEŞ-BOLYAI, PHYSICA, XLIX, 2, 2004

STRUCTURAL INVESTIGATIONS OF (BI,PB):2223 HIGH TEMPERATURE SUPERCONDUCTOR

A.V.POP[1)], D.MARCONI[1)], G.ILONCA[1)], M.POP[3)], J.M. LEBRETON[2)], L.LECHEVALIER[2)]

1) University Babes-Bolyai, Faculty of Physics, University "Babes-Bolyai", 3400 Cluj-Napoca, Romania
2) Universite de Rouen,U.F.R.des Sciences et Techniques, UMR CNRS 6634, Rouen, France
3)Technical University Cluj-Napoca,Faculty of Materials Science and Enginering, Department of MaterialsProcessingEngineering, 400641,Cluj-Napoca,Romania.

ABSTRACT. The physical properties of HTS are strongly influenced by nanoscale processes. The effect of Cu partial substitution by (Fe+Zn) on structural properties of (Bi,Pb):2223 HTS were investigated by X-ray diffraction and Mössbauer spectroscopy measurements. By increasing Zn concentration, the volume fraction of the major phase Bi:2223 decreases and the volume fraction of Bi:2212 increases. All Mössbauer spectra consist in a paramagnetic doublet, slightly dissymmetric, typical for Fe in superconducting compounds. The two contributions can be attributed either to two types of sites in the same compound, or to two types of compounds.

1.Introduction

Since the discovery of Bi-based superconducting cuprates [1,2] $Bi_2Sr_2Ca_{n-1}Cu_nO_{2n+4+d}$, a lot of work has been done concerning structural, electric and magnetic properties of these compounds.

The CuO_2 layers are considered to play a dominant role for the high T_c superconductivity. Depending on the number of CuO layers in the unit cell, the phases show superconducting transitions at T_c=10K (n=1),T_c=80K (n=2)and T_c=110K (n=3).

The structure consist of a sequence of perovskite-type units and BiO double layers with rock salt coordination. The average structures of of these phases have the lattice parameters of $a \approx 0.54$nm,$b \approx a$ and $c \approx 2.45$ nm (n=1),$c \approx 3.09$nm (n=2) and $c \approx 2.45$nm (n=3).

For a more complete understanding of the role of Cu in superconductivity, it is interesting to study the influence of partial substitution of Cu by 3d elements. The doping with ^{57}Fe isotope has enabled the use of Mössbauer spectroscopy to study the environments occupied by iron in Bi:2201, Bi:2212 and Bi:2223 phases [3-7]. Each cooper atom in the Bi:2201 phase is surrounded by six oxygen atoms (octahedral coordination) while in the Bi:2212 phase it is surrounded by five oxygen atoms (square pyramidal coordination).Cu atoms in the Bi:2223 phase exist in the square pyramidal as well as square planar coordination [8].

The Bi:2223 phase has attracted considerable interest due to its higher T_c and the potential for applications. One of the reasons for the low critical current densities J_{cJ} is the granular nature of this sintered HTS compound. In the (Bi,Pb):2223 superconducting ceramic samples the competition of intra- and intergrain conductivity is strongly temperature dependent and is differently affected by the 3d ions which substitute in the Cu positions [9-11].

In this paper we report the effect of (Zn+Fe) doping in the Cu position of (Bi,Pb):2223 superconductor on the intergranular properties of ceramic system, by using X-ray diffraction, Mössbauer spectroscopy and AC susceptibility measurements function of temperature and AC field amplitude.

2.Experimental

The $(Bi_{1.6}Pb_{0.4})(Sr_{1.8}Ba_{0.2})Ca_2(Cu_{1-x-y}Zn_xFe_y)_3O_z$ (x=0.00;0.01;0.02 and y=0.01) were prepared by the conventional solid state reaction method [10].

X-ray diffraction (XRD) analysis was performed by reflection with a Siemens D5000 system working in Bragg-Brentano $\theta - 2\theta$ geometry. The X-ray generator was equipped with a Co anticathode and it was using Co (K_α) radiation ($\lambda = 0.17909\text{nm}$).

Powder XRD measurements were made in an effort to check the phase purity as well as to determine the crystal structure and lattice parameters of the phases. The measurements were conducted in a θ–2θ-scan mode in the 2θ range of 20 – 80 degrees, the step angle and step time being 0.02^0 and 10s respectively.

All the samples were investigated by Mössbauer spectrometry as well. Mössbauer analysis was performed at room temperature, in transmission geometry using a ^{57}Co source in a rhodium matrix.

The real (χ') and immaginary (χ'') parts of the AC susceptibility were simultaneously collected with a Lake Shore Model 7000 AC susceptometer. The measurements were performed at a frecquency of 1000Hz as a function of temperature at fixed AC magnetic field amplitude (H_{ac}) in a range from 0.4 to 800 A/m.

The end of the diamagnetism in χ' (T) dependence, correspond to the intragrain critical temperature $T_{cG.}$ The T_{cG} values are 109,5K for (x=0.00;y=0.00), T_{cG} =106K for(x=0.02 Zn;y=0.00) and T_{cG} =100K for (x=0.02;y=0.01), respectively. In our samples T_{cG} are very close to the inflection point temperatures T_c in the resistivity measurements.

3.Results and discussion

XRD patterns of the $(Bi_{1.6}Pb_{0.4})(Sr_{1.8}Ba_{0.2})Ca_2(Cu_{1-x}{}^{57}Fe_{0.01}Zn_x)_3O_y$ powders are shown in Figure 1. To simplify, the samples with x=0.02 and x=0.05 are noted $AFeZn_2$ and $AFeZn_5$ respectively.

In both patterns, the most intense peaks correspond to a Bi-2223 phase (base-centered orthorhombic structure) with lattice parameters a= 0.5408 nm, b= 0.5420 nm and c=3.7075 nm (space group A2aa). The main peaks of an hexagonal Bi-Pb-Sr-Ca-Cu-O phase (labeled with arrows) are observed as well.

The corresponding lattice parameters are a= 0.9927 nm and 0.3473 nm. In the pattern of the AFeZn5 sample, the main peaks of a Bi-2212 phase (labeled with

star*) are observed, with a very weak intensity. This phase has an orthorhombic structure, and the corresponding lattice parameters are a= 0.5408 m, b= 0.5413 nm and c= 3.8710 nm.

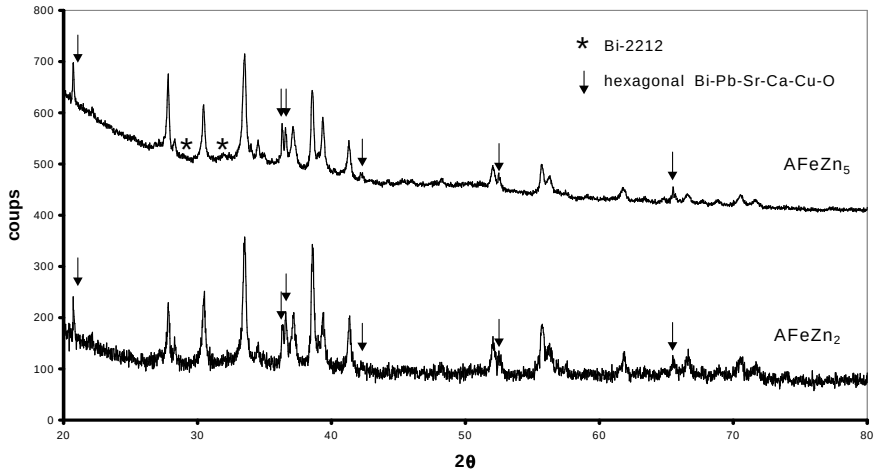

Fig. 1. XRD patterns of $(Bi_{1.6}Pb_{0.4})(Sr_{1.8}Ba_{0.2})Ca_2(Cu_{1-x}{}^{57}Fe_{0.01}Zn_x)_3O_y$ powders, with x=0.02 ($AFeZn_2$) and x=0.05 ($AFeZn_5$).

These results indicate that the Bi-2223 phase is the major phase in both samples. However the samples are not single phase, as an hexagonal phase is also detected. Moreover, a Bi-2212 phase is present in the sample with x=0.05, in very low proportions.

The room temperature Mössbauer spectra of the Zn-containing samples are shown in Figure 2. All the spectra consist in a paramagnetic doublet, slightly dissymmetric typical for Fe in Bi-2212 or Bi-2223 superconducting compounds [6,7,12,13]. According to the literature, preliminary fittings were performed with one, two, three and four paramagnetic contributions. The best results were obtained here with two contributions, and the corresponding hyperfine parameters are reported in Table 1.

Table 1

Fitted hyperfine parameters corresponding to the Mössbauer spectra of the $AFeZn_2$ and $AFeZn_5$ samples. δ is the isomer shift (relative to metallic α-Fe), Δ is the quadrupolar splitting and FW is the full linewidth at half height.

	δ (mm.s-1)	Δ (mm.s-1)	FW (mm.s-1)	%
$AFeZn_2$	0.24 ± 0.01	1.14 ± 0.16	0.36 ± 0.01	95 ± 4
	0.51 ± 0.10	0.80 ± 0.10	0.36 ± 0.01	5 ± 4
$AFeZn_5$	0.24 ± 0.09	1.13 ± 0.16	0.36 ± 0.01	96 ± 4
	0.52 ± 0.05	0.81 ± 0.09	0.36 ± 0.01	4 ± 4

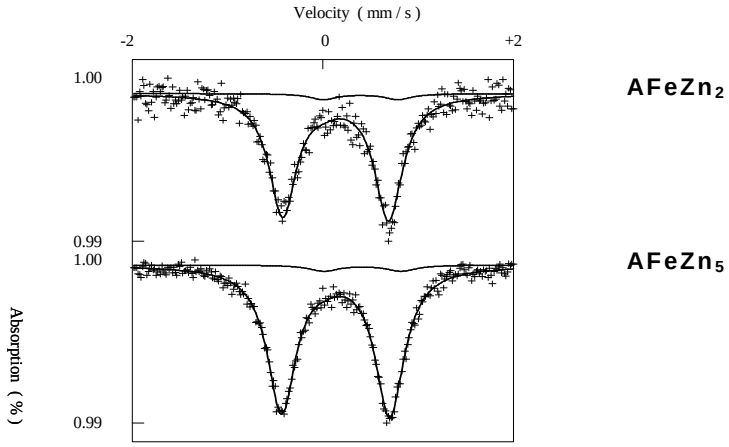

Fig. 2.- Room temperature Mössbauer spectra of the $AFeZn_2$ and $AFeZn_5$ powders. The second paramagnetic contribution is displayed.

The two contributions can be attributed either to two types of sites in the same compound, or to two types of compounds.

The major contribution (more than 90% of the relative intensity) is typical for Fe in Bi-2212 or Bi-2223 compounds [6,7,12,13,14]. Thus, this contribution is attributed to the Bi-2212 phase in the Co-containing samples, and to the Bi-2223 phase in the Zn-containing samples.

The high value of the quadrupolar splitting Δ (1.13 to 1.14 $mm.s^{-1}$) corresponds to Fe atoms located in Cu pyramidal sites of both Bi-2212 and Bi-2223 phases [6]. In these sites, Cu atoms are surrounded by pyramidally coordinated oxygen.

The high value of the corresponding isomer shift (0.5 to 0.7 $mm.s^{-1}$) could correspond to Fe^{3+}. As, according to XRD results, $AFeZn_2$ and $AFeZn_5$ samples contain Bi-2212 and Bi-2223 phases only, this contribution corresponds to Fe^{2+} ions in both phases.

4.Conclusions

The Cu substitution simultaneously by Zn (x=0.00.0.02;0.05) and Fe (y=0.00;0.01) in $Bi_{1.6}Pb_{0.4})(Sr_{1.8}Ba_{0.2})$ $Ca_2(Cu_{1-x}Fe_{0.01}Zn_x)_3O_y$ bulk superconductor was performed.

Critical transition temperature T_c decrease by increasing the concentration x and y for the Zn and Fe ions.

X-ray diffraction analysis of the (Bi,Pb)(Sr,Ba):2223 samples shows that they contain Bi-2223 phases as majority phase. In all samples the peaks of an hexagonal Bi-Pb-Sr-Ca-Cu-O phase are observed For sample with (x=0.05 Zn and y=0.01Fe) some weak peaks of 2212 sample were evidenced.

All Mössbauer spectra consist in a paramagnetic doublet, slightly dissymmetric typical for Fe in Bi-2212 or Bi-2223 superconducting compounds. Fitted parameters corresponding to the Mössbauer spectra by using two paramagnetic contributions shows that Fe^{2+} ions have a strong preference for the square pyramidal positions of Cu ions.

REFERENCES

1. Michel C., Hervieu M., Borel M.M., Gradin A., Deslandes F., Provost J. and Raveau B, *Z.Phys*. **B 68**,421(1987)
2. H.Maeda, T.Tanaka, M. Fukutomi and T. Asano, *Japan.J.Appl.Phys*.**27** L209(1988).
3. O.Bremet, C.Michaelsen, H.U.Krebs, *J.Appl.Phys*.**65**,1018(1989).
4. H.Tang,Z.Q.Qiu,Y.W.Du and J.C.Walker,*J.Appl.Phys*.**67**,4512 (1990).
5. M.Mehbod,E.Vanlathem, R.Deltour, P.H.Duvigneaud, P.Wyder, M.Verwerft, G. Van Tendeloo, J.Van Landuyt, *Physica* ***C*****168**,265(1990).
6. G.Marest, B.Hannoyer, F.Petit, D.D.Choughule, S.B.Ogale, S.I.Patil, *Physica* ***C*** **308**, 85(1998).
7. S.C.Bhargava, J.S.Chakrabarty, S., Singh, *Solid State Communications* **109**, 322 (1999).
8. T.Kanai, T.Kamo, S.Matsuda, *Jpn.J.Appl.Phys*.**28**, L551(1989).
9. A. M. Maeda, T. Yabe, S. Takebayashi, M. Hase and K. Uchinokura, *Phys. Rev.* **B41**, 4112 (1990).
10. A. V. Pop, R. Deltour, A. Harabor, D. Ciurchea, Gh. Ilonca, V. Pop, M. Todica *Supercond. Sci. Technol*.**10**, 843 (1997).
11. A.V.Pop, *Supercond.Sci.Technol* **12**, 672 (1999).
12. A.K. Jha and R.G. Mendiratta, *Solid State Communications* **93**, No.1, pp79-82 (1995)
13. Juichiro Arai, Toshiyuki Yamagishi, *Journal of Magnetism and Magnetic Materials* **177-181**, pp515-516 (1988)
14. C. Namgung, J. Irvine, E. Lachovski, A. West, Supercond. Sci. Technol. Vol.2, p.140 (1989)

STUDIA UNIVERSITATIS BABEŞ-BOLYAI, PHYSICA, XLIX, 2, 2004

MD SIMULATIONS OF BIOLOGICAL ION CHANNELS IN INTENSE MAGNETIC FIELDS

TITUS A. BEU

University "Babeş-Bolyai", Faculty of Physics
M. Kogălniceanu 1, RO-3400 Cluj-Napoca, Romania
E-mail: tbeu@phys.ubbcluj.ro

ABSTRACT. The transport of sodium ions through a model membrane channel in the presence of intense static magnetic fields is investigated by nonequilibrium molecular dynamics. The effect of the magnetic fields (1 - 100 T) appears to be exerted not mainly on the transiting ions (presumably reducing their transport rates by deflections), but rather on the water molecules, favoring statistically their polarization during the ion passages and leading indirectly to a slight increase of the ion current.

1. Introduction

The utmost importance of investigating biological membrane channels is reflected plenary by the award of the Nobel Prize in Chemistry for 2003 to Peter Agre and Roderick MacKinnon "for discoveries concerning channels in cell membranes".

Ion channels are proteins that control the passage of ions across cell membranes, and thus regulate important biological functions, such as the generation of action potentials in nerves and muscles, or the hormone release from endocrine cells. They are highly selective for particular ion types (Na^+, K^+, Ca^{2+} etc.) and show high transport rates (of the order of 10^8 ions/s), corresponding to currents of several tens of pA.

Ion channels are assumed to play an important role in pain control [1], and their functionality is believed to be influenced by magnetic fields. The present work is meant to be a contribution to the elucidation by means of non-equilibrium molecular dynamics (NEMD) simulations at atomic level of several aspects regarding the transport through ion channels in the presence of intense static magnetic fields.

The most realistic and detailed simulations concerning the ion dynamics in membrane channels in the absence of magnetic fields are those published by Crozier et al. [2,3], and many of the models and simulation details therein have been adopted in the present work, too. The main modeling differences regard the consideration of magnetic fields in the range 1 – 100 T and the usage of a more elaborate four-site water molecule model, meant to more accurately account for the polarization and structural properties of water. Technically, rigid-body dynamics for water in the quaternion representation was employed to make the computations more efficient and to allow for a better statistics by considering a two times longer data collection interval.

2. The Model

The channel model considered here is the one proposed by Crozier et al. [2,3], consisting of a cylindrical rigid atomic pore with polar walls, 25 Å long and 10.625 Å in diameter, embedded in a rigid uncharged membrane. 388 interaction sites are

distributed on a 10 atoms × 10 atoms square lattice on both membrane surfaces, with an atom-atom spacing of 2.5 Å, and on the channel, forming eleven 20-site rings, with a spacing of 2.5 Å along the channel axis. All sites feature Lennard-Jones interactions with $\sigma = 2.5$ Å and $\varepsilon/k = 60$ K. Additionally, the channel sites carry charges equal to -0.5e, -0.35e, +0.35e, +0.5e, disposed cyclically on the rings, with a relative rotation of 9°between adjacent rings to produce a helical charge distribution.

A 1*M* NaCl solution was considered, which was modeled by 600 water molecules, 8 Na^+ and 8 Cl^- ions. The water molecules were accurately represented by the rigid four-site model TIP4P of Jorgensen et al. [4], intensively used in the last two decades in simulations of aqueous solutions and clusters and known to describe more accurately than other three-site model potentials the thermodynamic and structural properties of water (radial distribution function and partial structure function). The Lennard-Jones parameters for ion-ion and ion-water interactions are summarized in Table 1 of Ref. [3].

The simulation cell was considered a parallelepiped 25 Å × 25 Å × 55 Å in the *x*, *y*, and *z* directions respectively, with the membrane channel centered along the *z*-axis and two reservoirs (designated as “entry” and “exit”) formed symmetrically on either side of the membrane.

The dynamics of the water molecules was decomposed in center-of-mass translation and rotation, described in the quaternion formalism [5], thus substantially reducing the total number of degrees of freedom (roughly by 1/3) and avoiding the necessity of a supplementary “shake”-type algorithm to preserve the equilibrium structure of the water molecules. A Gaussian thermostat [5] for the translational degrees of freedom of the water molecules was used to prevent the system from heating due to particle transport across the membrane and to fix the system temperature at 300 K. The rotational degrees of freedom of the water molecules and the translational degrees of freedom of the ions were allowed to relax freely to the equilibrium temperature.

To allow for a continuous flow of ions and water molecules without repositioning or recycling, periodic boundary conditions were applied in all three directions. However, to account correctly for the long-range electrostatic interactions of the charges and their periodic images, additionally Ewald sum techniques were employed [6]. By using the P^3M particle-particle/particle-mesh FFT-accelerated Ewald method as described by Deserno and Holmes [7], simulations over a sufficiently long time interval (200 ns) were possible, in order to measure current flow. Reciprocal space contributions were treated according to the particle-mesh methodology with a seventh-order charge assignment function on a 16 × 16 × 64 mesh point grid. The potential due to the particles and channel sites was obtained by solving the Poisson equation for the ensemble-averaged mesh-based charge distribution in the reciprocal space by using FFT.

A homogeneous electric field (0.02 V/Å) was applied parallel to the channel axis (z-axis) to mimic the potential gradient that drives ions through biological channels. Additionally, homogeneous magnetic fields of 1, 10, and 100 T were considered along and, respectively, transverse to the channel.

For each magnetic field configuration, 20 simulations spanning 10 ns were performed, making up a total of 200 ns of data collection. In order to allow for a more conclusive analysis of the trends, the individual runs for all magnetic field

configurations were started from the same 20 initial configurations, which were prepared themselves from unique structured lattices of randomly placed water molecules and ions, which were equilibrated for 0.25 ns.

The MD integrator employed, both for the translational and rotational degrees of freedom, was a fifth order Gear-type algorithm [5]. We have used throughout a time step of 0.25 ps and a data storage interval of 2.5 ps.

3. Results and Discussion

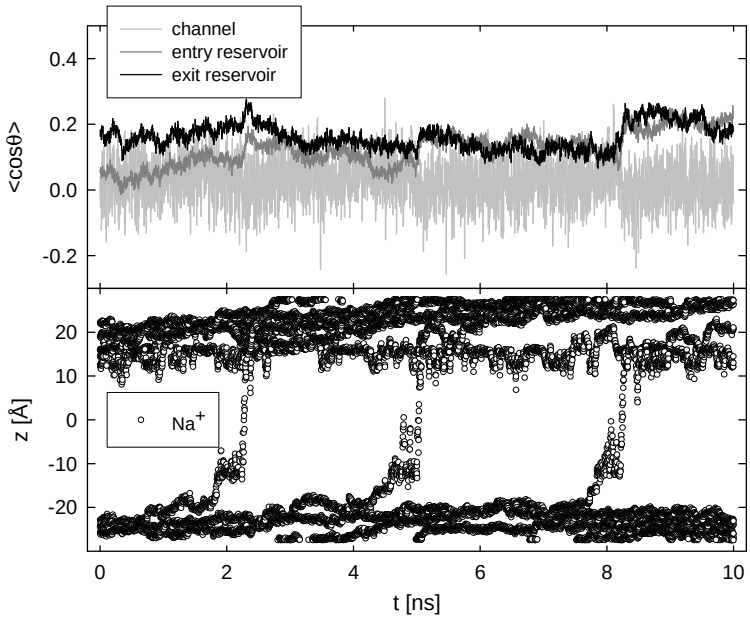

Figure 1. Positions of the Na^+ ions along the channel axis and average polarization angle of the water molecules over a typical time interval of 10 ns.

The lower panel of Figure 1 depicts the instantaneous z-positions of the Na^+ ions for a typical simulation interval of 10 ns. The average cosine of the polarization angle θ of the water molecules, defined between their electric dipole and the direction of the applied electric field (channel axis), is shown in the upper panel separately for the channel and the reservoirs. As can be seen, ion passages are accompanied by a pronounced polarization of the water, followed by relaxation.

The water polarization in the channel features large fluctuations as compared to the reservoirs and a more rapid relaxation, as well. After ion passages, the average polarization typically reverses the sign, the dipole of the water molecules showing a tendency to follow the ion as it moves along the channel. It can be easily seen that the average polarization in the channel is lower than in the reservoirs, where in addition it persists for a longer time due to the larger number of molecules.

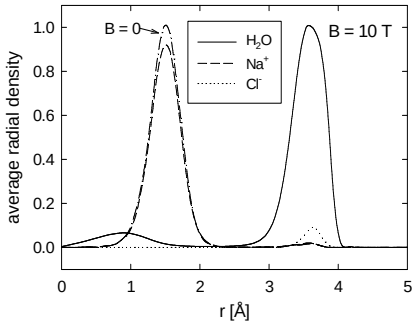

Figure 2 Ensemble averaged radial density profiles. The water profile is normalized to its maximum value. The ion profiles are normalized to the maximum radial ion density for B = 0

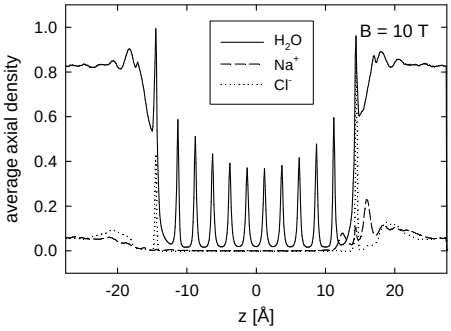

Figure 3 Ensemble averaged density profiles along the channel axis. The water profile is normalized to its maximum value. The ion profiles are normalized to the maximum axial ion density for B = 0.

The channel appears to be structured, the water molecules forming boundary layers both inside the channel (as can be seen from the radial density profiles in) and at the membrane surfaces (see the axial density profiles in). It is obvious, that while passing through the channel, the ions prefer certain paths along the axis. The most probable radial position of the water molecules in the channel is around 3.5 Å (in the immediate vicinity of the walls), while for the Na^+ ions (having a transition rate more than one order of magnitude higher than for the Cl^- ions), the radial density peaks around 1.5 Å. Both the radial and the axial density profiles turn out to depend little on the applied magnetic field, implying essentially that the water structure is little sensitive to the magnetic field.

Figure 4 shows the transversally averaged spatial voltage profile along the channel axis, calculated from the ensemble-averaged mesh-based charge distribution. The potential drop is found mainly across the channel, rather than across the reservoirs, reflecting the formation of a spatial charge (electrochemical double layer) at the membrane walls. The double layer partially neutralizes the applied electric field in the reservoirs and the overall behavior agrees qualitatively with the one reported by Crozier et al. [2,3].

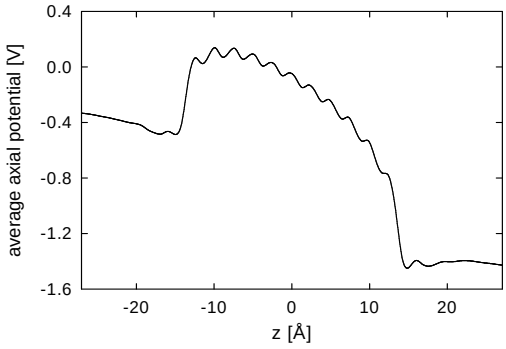

Figure 4. Ensemble and transversally averaged electrostatic potential along the channel.

Table 1 summarizes the relevant quantities which characterize the ion transport over the ensemble of 20 simulations making up the entire data collection interval of 200 ns. For each non-zero magnetic field value considered (1, 10, and 100 T), simulations were performed for the perpendicular (⊥) and parallel (∥orientations of the magnetic field relative to the channel axis and the corresponding results enter the derived quantities with the weights 2/3 and 1/3, respectively. The ion passages have been identified by the entry of the ion into the channel from one of the reservoirs and the subsequent exit to the opposite reservoir (without intermediate reexit to the initial reservoir). The ion passage times have been defined as ensemble averages of the individual passage times and together with the channel length have been used to express the average passage velocities. The net current was derived from the net charge transfer across the channel.

Table 1.

Statistics of ion passages over a time interval of 200 ns. Negative numbers of passages imply net motions in the negative z-direction (opposed to the applied electric field). The average passage times and velocities refer to the channel only.

B [T]		No. of ion passages		Average passage time [ps]		Average passage velocity [m/s]		Average water polarization <cosθ>			Net current [pA]
		Na^+	Cl^-	Na^+	Cl^-	Na^+	Cl^-	entry reservoir	channel	exit reservoir	
0		61	1	32.4	1610	77.1	1.55	0.078	0.030	0.104	48.1
1	⊥	62	-1	27.3	2978	91.6	0.84	0.084	0.028	0.110	50.5
	∥	62	1								
10	⊥	66	0	26.0	563	96.0	4.44	0.091	0.027	0.114	51.5
	∥	60	-1								
100	⊥	63	0	34.7	2276	72.1	1.10	0.087	0.028	0.123	51.8
	∥	67	-1								

Whereas the total number of passages takes values around 60 for the Na^+ ions (~0.3 passages/ns) and slightly increases with the intensity of the applied magnetic field, at most one Cl^- ion passage in the negative z-direction was observed irrespective of the applied magnetic field. As an exception, in the case B = 0, the Cl^- ion was rather dragged by a Na^+ ion in the positive electric field direction. The simulations of Crozier et al. [2] for B = 0 evidenced typically 12 complete Na^+ ion passages and no Cl^- ion passages over the considered interval of 100 ns of data collection. Possible causes of this smaller transport rate could be the different initial configurations of the simulations, the shorter data collection interval, and the different water model, as well. It should be noted that the selectivity of the channel with respect to the ion species does not appear to be influenced by the magnetic fields.

As can be seen from Table 1, the average passage times of the Na^+ ions across the channel take values around 30 ps, not showing any apparent correlation with the magnetic field. The corresponding passage time reported by Crozier et al. amounts to 0.8 ns, and the appreciable difference to the present result is obviously due to the different definitions: total time in which there is an ion in the channel divided by the net number of passages, in contrast with the average interval of the successful passages only, used in the present work.

The net currents through the channel amount to approximately 50 pA, in qualitative agreement with experiments and the result reported by Crozier et al. (24.7 pA) for conditions compatible to those in our simulations. They show a tendency of increasing (up to 10%) with the applied magnetic field, contrasting with the intuitive expectation for the ion transport rate to decrease due to the magnetic deflections.

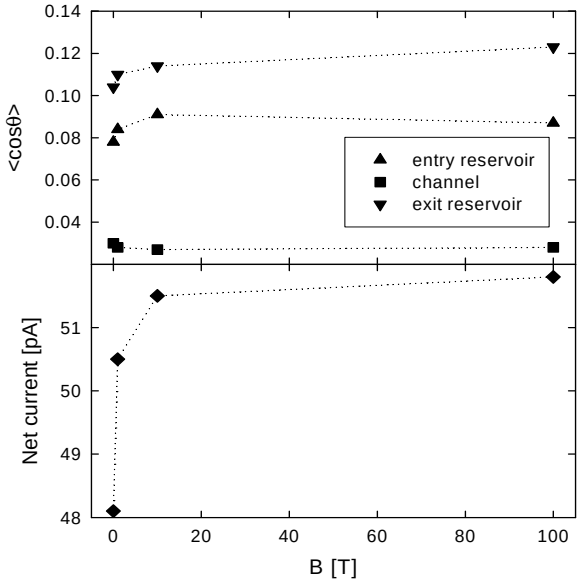

Figure 5. Magnetic field dependence of the polarization (cosθ) and net current.

As already pointed out by St. Pierre et al. [8], the Lorenz forces corresponding to technologically available magnetic fields are not capable of producing notable deflections on the cellular scale and thus to lead to a decrease of the ion flow. For the average velocities listed in Table 1, and even for the maximum instantaneous velocities, the associated Larmor radii turn out to be orders of magnitude over the channel size. Instead, by corroborating the magnetic field dependence of the net current with the behavior of the ensemble averaged water polarization (see also), showing itself an increasing trend in the reservoirs with increasing magnetic field, a different picture emerges.

Ion passages induce the water polarization, whereas the tilting of the water molecules is stochastically enhanced by the presence of the magnetic field, which acts like a small perturbation (especially in the case of the transverse orientation with respect to the channel axis). In turn, the more persistent polarization in the reservoirs causes the ions to experience a locally increased driving electric field. As can be seen from, already a modest magnetic field of 1 T produces the effect, higher field intensities enhancing the effect less, with a certain saturation tendency. The effect cannot be identified in the channel itself, where, due to the little number of water molecules, the relaxation subsequent to polarization is much faster than in the reservoirs.

Conclusions

The ion channel is structured – water forms boundary layers in the channel and at the membrane walls. It shows high transport rates (~3×10^8 ions/s) and high selectivity (Na^+ passages are roughly 60 times more probable than Cl^- passages).

Ion passages cause a pronounced water polarization and the quantitative description of the process relies on the appropriateness of the water model. Water polarization in magnetic fields as compared to the field-free case is enhanced in reservoirs, but remains practically unchanged in the channel. The magnetic fields technologically available cause a slight increase of the ion current (up to 10%), not a decrease as intuitively expected, acting as perturbations enhancing ion transport. The channel selectivity, however, is not affected by magnetic fields.

The cost of the presented numerical "experiment", estimated from the average simulation speed (1.25 ns/day) on up-to-date workstations and PCs and the total of 1400 ns simulated, was about 1100 CPU days.

Acknowledgements

The author is indebted to Prof. Jun Onoe for his hospitality at the Tokyo Institute of Technology, where some of the final runs were performed.

REFERENCES

1. Marcotte I, Ouellet M, Auger M, Chemistry and Physics of Lipids **127**, 175 (2004).
2. P.S. Crozier et al., Phys. Rev. Lett. **86**, 2467 (2001).
3. P.S. Crozier et al., Biophys. J. **81**, 3077 (2001).
4. W.L. Jorgensen, J. Chandrasekhar, and J.D. Madura, J. Chem. Phys. **79**, 926 (1983).
5. D.C. Rapaport, *The Art of Molecular Dynamics Simulation*, Cambridge University Press, Cambridge, 1995.
6. R.W. Hockney and J.W. Eastwood, *Computer Simulation Using Particles* (IOP, Bristol, 1988).
7. M. Deserno and C. Holm, J. Chem. Phys. **109**, 7678 (1998); J. Chem. Phys. **109**, 7694 (1998).
8. T.G.. St.Pierre, J. Dobson, Eur. Biophys. J. **29**, 455 (2000).

STUDIA UNIVERSITATIS BABEŞ-BOLYAI, PHYSICA, XLIX, 2, 2004

SPECTROSCOPIC CHARACTERISATION OF SOME OXIDE MATERIALS WITH BIOMEDICAL POTENTIAL

SIMION SIMON

Babeş - Bolyai University, Faculty of Physics, RO-400084 Cluj-Napoca, Romania
simons@phys.ubbcluj.ro

ABSTRACT. The phosphate based glasses and vitroceramics are oxide materials with high potential to be used in biomedical applications due to their biocompatibility and capabilities to form degradable temporary scaffolds for regeneration of hard and soft tissues.

In order to confer them microbial resilience small amount of silver oxide is introduced due to antimicrobial activity of leached Ag^+ cations. On such a way silver nanoparticles could be embedded in bioglass matrices.

The most efficient way of characterising the local structure of such bionano-materials, essential for understanding and controlling their physical and chemical properties, is to use complementary spectroscopic methods like nuclear magnetic resonance, electron paramagnetic resonance, infrared and Raman spectroscopy. All these techniques together with X-ray diffraction and scanning electron microscopy have been applied to characterise the calcium-soda-phosphate glasses containing Ag_2O up to 20 mol %. The structural features of these materials are related with their behaviour in simulated body fluids.

Introduction

The network structure of phosphate glasses is based upon a tetrahedral PO_4 structural unit. However, the structural behaviour of phosphate glasses is markedly different from that of most tetrahedral glassy networks, such as silicate glasses. The reason for this is that the fifth valence electron of the P atom forms an additional π bond with one of the oxygen neighbours, making this a terminal bond. The presence of terminal oxygen atoms makes phosphate glasses well suited for accommodation of various modifier cations which themselves may stabilise the network.

Vitreous P_2O_5 is an extremely hygroscopic substance. However, the addition of modifier cations to the network stabilizes the glasses and can confer them a large variety of potential applications, such as bioactive materials [1, 2], sensor applications, glass-to-metal sealing, optoelectronic devices, laser host glasses and solid state ionic conductors. The various properties of the glass are determined by the type of modifier cations and the degree of depolymerization of the phosphate network [3].

In all these materials the PO_4 tetrahedron appears as a stable structural element whose internal structure is mainly determined by the sp^3 hybridization of four of the five valence electrons. The fifth valence electron populates a d-orbital which in the threefold-linked tetrahedron of vitreous P_2O_5 (Fig. 1) forms a π-bond with the terminal oxygen atom that is not bridged to other tetrahedra (nonbridging oxygen, O_{NB}). Thus, a PO_4 tetrahedron is linked to the rest of the glassy network by a maximum three of its four vertices. The addition of modifier leads to a network degradation whereby the π-bond character is delocalised on all the terminal P-O_{NB} bonds of a given tetrahedron. These processes have been well studied by a variety

of spectroscopic methods which have shown that, up to the metaphosphate composition, $Me(PO_3)_v$, where v is the valence of the metal atom Me, only three- and twofold-connected PO_4 tetrahedra coexist.

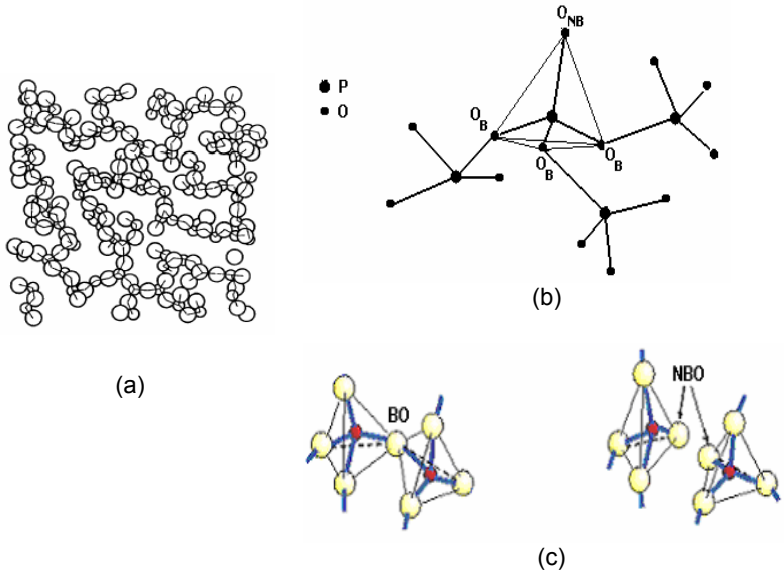

Fig. 1. A section for the model of the network of pure vitreous P_2O_5 (a), formed from threefold-linked PO_4 tetrahedra (b), which contain bridging and terminal (nonbridging) oxigens (c).

Beyond this composition, twofold-linked PO_4 tetrahedra and PO_4 end groups connect together to form chains and/or rings. Since the additional π-character shortens all the terminal P-O_{NB} bonds, the corresponding bond lengths may be differentiated from those occurring in P-O_B-P bridges. This effect makes it possible to gain detailed knowledge about the alterations of the bond lengths to the bridging (O_B) and the non-bridging oxygen (O_{NB}) atoms in the basic PO_4 structural unit by spectroscopic studies [4].

Most recently the phosphate-calcium-sodium glasses have paid attention due to their valuable capabilities shown to the formation of degradable temporary scaffolds for the regeneration of hard and soft tissues as they would eventually replace the natural tissue.

The introduction of silver has become one of the preferred methods that confers microbial resiliency on biomedical materials and device, since the incidence of biomaterial is one of the main causes of revision surgery [5-7].

Complementary spectroscopic methods like nuclear magnetic resonance, electron paramagnetic resonance, infrared and Raman spectroscopy together with X-ray diffraction and scanning electron microscopy have been applied in order to characterise the local structure of the calcium-soda-phosphate glasses containing Ag_2O up to 20 mol %.

Experimental

Glass samples belonging to (100-x)[50P_2O_5·30CaO·20Na_2O]xAg_2O system ($0 \leq x \leq 20$) were prepared using as starting materials: $NH_4H_2PO_4$, $CaCO_3$, Na_2CO_3·10H_2O and Ag_2O of reagent purity grade.

The mixtures corresponding to the desired compositions were melted in air, in sintered corundum crucibles, in a Carbolite RF 1600 electric furnace at 1200 °C, and maintained for 15 minutes at this temperature. The melts were quickly cooled at room temperature by pouring and pressing between two stainless steel plates.

MAS NMR measurements were performed on Bruker AVANCE 400 MHz, at room temperature, with a spinning speed of 15 kHz using 85 % H_3PO_4 water solution as reference.

The micro-Raman measurements were performed on a Dilor Labram system equipped with a 100 X 0.80 microscope objective, an 1800 lines/mm grating and an external laser with an emission wavelength of 514.5 nm. In the recording of the micro-Raman spectra a power of 100 mW incident on the sample has been employed. The spectral resolution was of about 2 cm^{-1}. For IR measurements the glasses were powdered and mixed with KBr in order to obtain thin pellets with a thickness of about 0.3 mm. The IR spectra were recorded with a Bruker Equinox 55 spectrometer; the spectral resolution in this case was 2 cm^{-1}.EPR spectra were recorded on powder samples, in X band, on ADANI spectrometer, at room temperature.

Results and discussion

Pure vitreous P_2O_5 consist in a continuos random network of quasi-tetrahedral PO_4 units wherein phosphorous is four coordinated (Fig. 1). The structure of phosphate glasses can be analysed by using the Q^n terminology, first introduced for silicate glasses and also adopted for phosphate ones [8], where n is the number of bridging oxygens in a tetrahedral unit. In this case Q^o represents isolated tetrahedral unit and Q^3 a maximum three connected tetrahedra (Fig. 2). The presence of the modifier like alkali and alkaline earth species decreases the number of bridging oxygens (P-O-P bridge) in PO_4 units. The tetrahedrons are linked together in chains or rings by bridging oxygens.

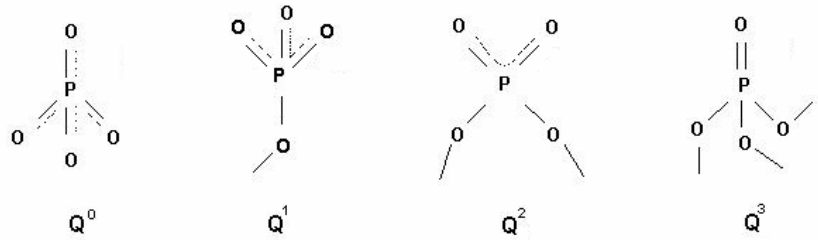

Fig. 2. The structural PO_4 units according to Q^n terminology.

CaO, Na_2O and Ag_2O act as glass network modifiers. CaO is a well known glass modifier and may enter the glass network by transforming two Q^3 tetrahedra into two Q^2 tetrahedra (Fig. 2) and thus a CaO polyhedron is formed when calcium ions are surrounded by such two Q^2 and several Q^3 tetrahedrons [9]. If new modifiers like Na_2O and Ag_2O are added, the depolimerisation of the phosphate glass structure is even more pronounced and Q^1 units are formed. This structure behaves as a defect in the network of tetrahedral units [10].

X-ray diffraction analyses and scanning electron microscopy show the vitreous state of the as prepared samples. Samples of the same composition and similar thermal history were tested in simulated body fluid (SBF). They find in the simulated body fluid conditions to develop at their surface an energetically more favorable arrangement of the component atoms in apatite like crystals.

Solid-state magic angle spinning (MAS) nuclear magnetic resonance (NMR) spectroscopy has become a powerful tool for the investigation of local structure and medium range order in glasses. Previous ^{31}P MAS NMR studies have detailed the local structure for a series of phosphate glasses [11-14]. Phosphate tetrahedra within the glass network are commonly described using the Q^n notation, where n= 0, 1, 2, 3 and represents the number of bridging oxygens attached to the phosphate unit. The ^{31}PMAS NMR spectra (Fig. 3) recorded from the glass samples without silver and with x = 0.25 mol % Ag_2O_3 consist of an intense isotropic peak at about –24 ppm and a weaker peak at about –9 ppm. These lines arise from ^{31}P nuclei belonging to Q^2 middle-chain tetrahedral units involved in long phosphate chains, respectively from Q^1 end chain tetrahedral units [11, 12].

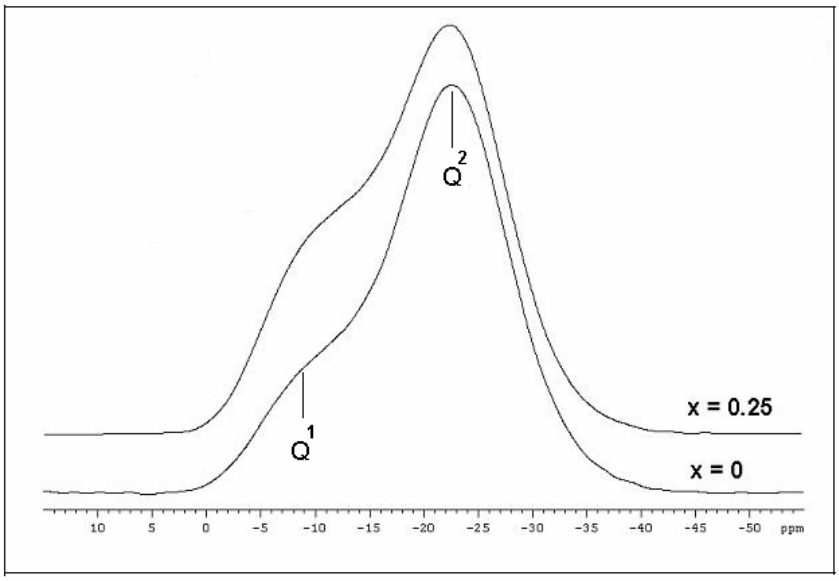

Fig. 3. MAS NMR spectra recorded from (100-x)[$50P_2O_5 \cdot 30CaO \cdot 20Na_2O$]x$Ag_2O$ glass samples.

Based on these MAS NMR data it can be suggested that the investigated $50P_2O_5 \cdot 30CaO \cdot 20Na_2O$ matrix glass network is built up mainly from linked ionic phosphate groups like $(PO_2)^-$ (Q^2 species), and in a less amount from $(PO_3)^{2-}$ (Q^1 species). By adding silver oxide up to x = 0.25 a depolimerisation of the phosphate network takes place and the number of terminal nonbridging oxygens and implicitely of Q^1 species increases. Microraman spectra (Fig. 4) show that no well-defined Ag-O-X (X = P, Ca, Na) bonds are formed in the samples with silver. Distortions of the phosphate units give rise to visible changes in the 400-650 cm^{-1} spectral range of the infrared spectra.

The same significant depolimerisation process with the addition of Ag_2O (Fig. 4), especially for 10 and 20 Ag_2O mol % is confirmed by Raman and IR results, being remarked a decrease of the P=O bond number and an increase of the non-bridging $(PO3)^{2-}$(Q^1 species) units number as well as the conversion of the long chain phosphate units in very short phosphate chains.

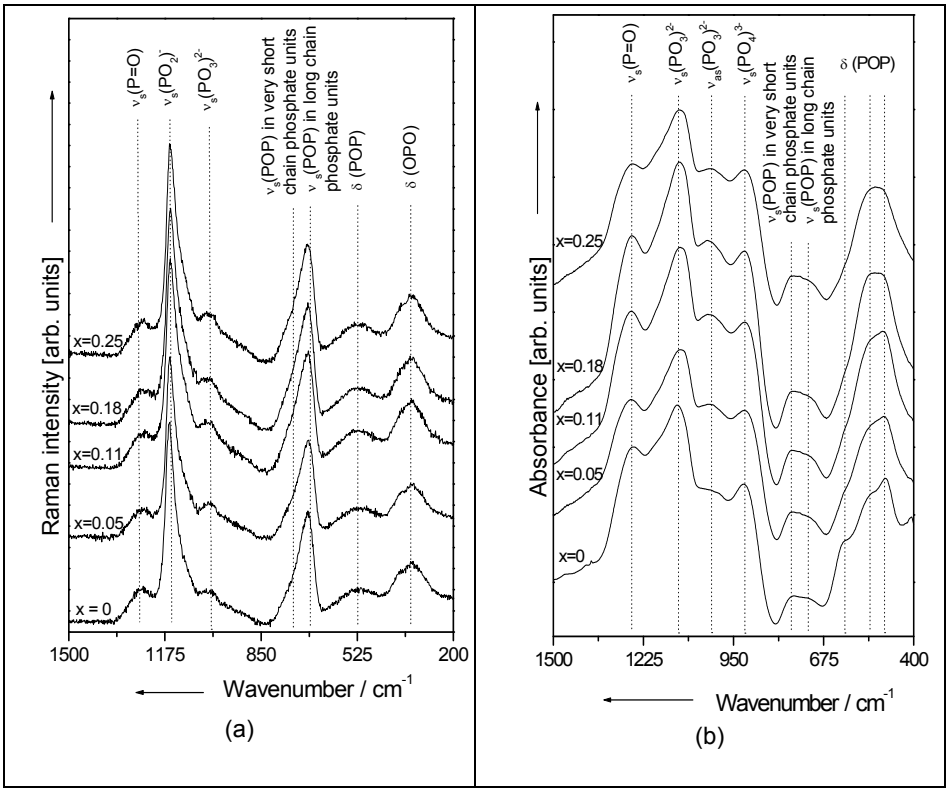

Fig. 4. Micro-Raman (a) and IR spectra (b) of $(100-x)[50P_2O_5 \cdot 30CaO \cdot 20Na_2O]xAg_2O$ glasses

The appearance in the UV VIS spectra (Fig. 5) of an electronic absorption band at 408 nm for the samples with 3 and 5 mol % Ag_2O is related to the existence of small spherical silver nanoparticles in the glass, while a shift of this band towards longer wavelengths show the presence of particles with a non spherical (or non equiaxial) shape. The relative constancy of this electronic absorption band position independent of silver concentration indicates the presence in the glass matrix of silver nanospheres with about the same radius.

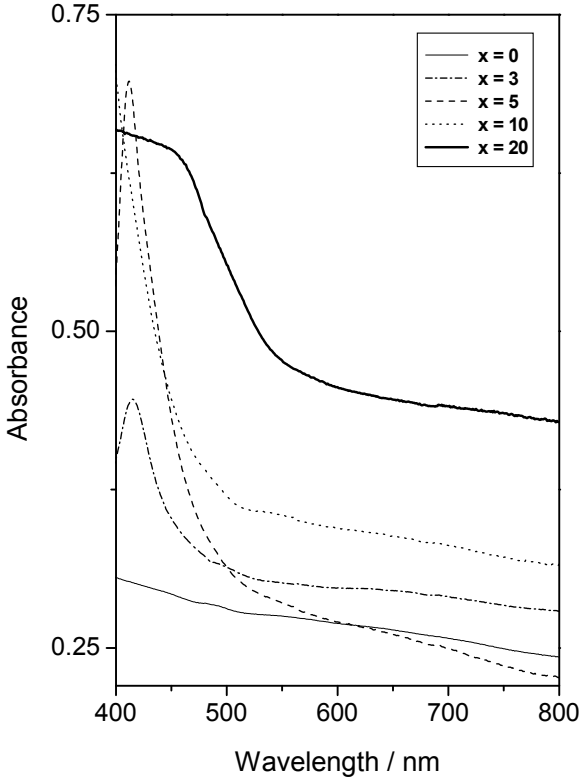

Fig. 5. UV-VIS spectra of (100-x)[$50P_2O_5 \cdot 30CaO \cdot 20Na_2O$]x$Ag_2O$ glasses

The depolimerisation process (x = 10 and 20) of the phosphate glass network is consequently followed by the occurrence of an intensified aggregation process of the silver cluster as Ag_2O content increases.

The EPR spectra (Fig. 6) recorded from(100-x)[$50P_2O_5 \cdot 30CaO \cdot 20Na_2O$]x$Ag_2O$ glasses show major differences in the surrounding of the resonant centers with increase of Ag_2O content. EPR signals are associated with silver species. The resonant centers could be created by Ag^+ trapping an electron. On trapping an electron silver ions may form four types of centers: the single Ag^0 or (Ag^+ + e) centers, and, at higher Ag contents, the $Ag^0(Ag^+)$ or (Ag^+ + e) (Ag^+) centers in which a second silver is involved [15, 16]. The formation and stability of these centers is critically dependent on silver content and, as can be seen in Figure 6,

the paramagnetic species are aggregated in clusters and give rise to relatively large lines around g ≈ 2.1. Some paramagnetic impurities like Mn^{2+} and Fe^{3+} ions bring their contribution to the hyperfine features well visible in samples with low silver content and to the line with g ≈ 4.3, respectively.

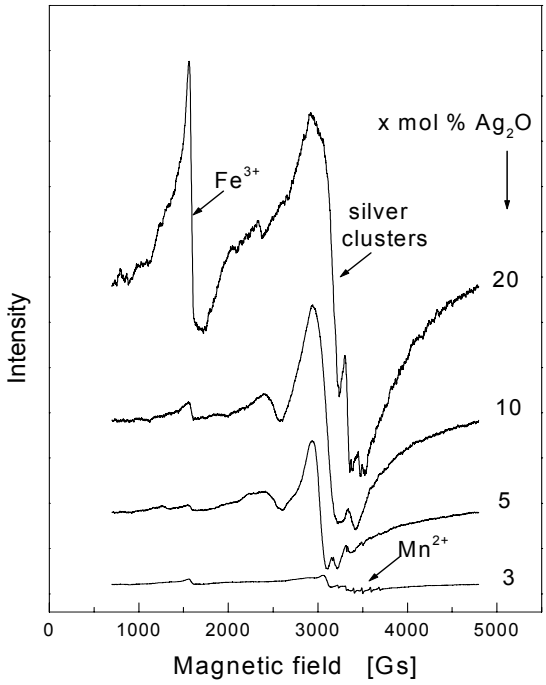

Fig. 6. EPR spectra of (100- x)[$50P_2O_5$·30CaO·$20Na_2O$]xAg_2O glasses.

Conclusions

NMR results show that in the investigated phosphate matrix mainly dominate Q^2 structural units and Q^1 species occurs in a less amount but its fraction increases with the silver content. The data obtained from UV-VIS spectroscopy evidence in the glass samples Ag_2O the silver aggregation in spherical nanoparticles with a diameter of about 5 nm. Raman and IR results indicate the progressive depolimerisation process by addition of Ag_2O even in very small concentrations and the distortions of the phosphate structural units for all samples. The aggregation of the silver diamagnetic and paramagnetic species in nanoparticles is also confirmed by the EPR results. The presence of the silver nanoparticles in the phosphate glass matrix and the behaviour of these glasses in the human body fluids is important for medical applications implying controlled release of silver in such environments.

Acknowledgements

We are grateful to Prof. Wolfgang Kiefer - University of Wuerzburg for allowing our student C. Popa to done IR measurements in his laboratories. We are also grateful for spectroscopic measurements to our Ph.D. students D. Muresan-Balasz, D. Petrisor, M. Vasilescu and last but not least to dr. L. Baia.

REFERENCES

1. M. Navarro, S. del Valle, S. Martinez, S. Zeppetelli, L. Ambrosio, J.A. Planell, M.P. Ginebra, Biomaterials, 256, 4233 (2004)
2. M. Bellantone, H.D. Williams, L.L. Hench, Antimicr. Agents and Chemotherapy, 46, 1940 (2002)
3. U. Hoppe, G. Walter, R. Kranold, A. Barz, D. Stachel, A.C. Hannon, J. Non-Cryst. Solids, 263-264, 29 (2000)
4. L. Baia, W. Kiefer, S. Simon, Recent Res. Devel. Non-Crystalline Solids, 4, 1-25 (2004)
5. M. Kawashita, S. Tsuneyama, F. Miyaji, T. Kokubo, H. Kozuka, K. Yamamoto, Biomaterials, 21, 4, 393 (2000)
6. M. Bellantone, H. D. Williams, L. L. Hench, Antimicrobial Agents and Chemotherapy, 46, 1940 (2002)
7. J. J. Blaker, S. N. Nazhat, A. R. Boccaccini, Biomaterials, 25, 7-8, 1319 (2004)
8. R.K.Brow, T.M.Alan, D.R.Tallant, RR.J.Kirkpatrick, MRS Bull., 23, 11, 63 (1998)
9. P. Subbalkshmi, N. Veeraiah, J. Non-Cryst. Solids, 298, 89 (2002)
10. K. Meyer, Phys. Chem. Glasses, 39, 108 (1998)
11. F. Fayon, C. Bessada, J.-P. Coutures, D. Massiot, Inorg. Chem., 38, 5212 (1999)
12. F. Fayon, I.J. King, R.K. Harris, J.S.O. Evans, D. Massiot, C. R. Chimie, 7, 351 (2004)
13. T.M. Alam, R.K.Brow, J. Non–Cryst.solids, 223, 1-2, 1 (1998)
14. BV.C. Tischendorf, T.M. Alam, R.T. Cygan, J.U. Otaigbe, J. Non–Cryst.solids, 316, 1-2, 261 (2003)
15. F. Assabghy, S. Arafa, E. Boulos, A. Bishay, N. J. Kreidl, J. Non-Cryst. Solids, 23, 1, 81 (1977)
16. J. Michalik, J. Sadlo, M. Danilczuk, Solid State Phenomena,94, 197 (2003).